MAGNETIC FIELDS NEAR MICROSTRUCTURED SURFACES: APPLICATION TO ATOM CHIPS

DISSERTATION
ZUR ERLANGUNG DES AKADEMISCHEN GRADES
DOKTOR DER NATURWISSENSCHAFTEN (DR. RER. NAT.)
IN DER WISSENSCHAFTSDISZIPLIN QUANTEN OPTIK

EINGEREICHT AN DER
MATHEMATISCH-NATURWISSENSCHAFTLICHEN FAKULTÄT
DER UNIVERSITÄT POTSDAM

VON
BO ZHANG

SUPERVISED BY
PROF. MARTIN WILKENS
DR. CARSTEN HENKEL

POTSDAM
5TH, NOVEMBER 2008

Abstract

Microfabricated solid-state surfaces, also called 'atom chip', have become a well-established technique to trap and manipulate atoms. This has simplified applications in atom interferometry, quantum information processing, and studies of many-body systems. Magnetic trapping potentials with arbitrary geommetries are generated with atom chip by miniaturized current-carrying conductors integrated on a solid substrate. Atoms can be trapped and cooled to μK and even nK temperatures in such microchip trap. However, cold atoms can be significantly perturbed by the chip surface, typically held at room temperature. The magnetic field fluctuations generated by thermal currents in the chip elements may induce spin flips of atoms and result in loss, heating and decoherence. In this thesis, we extend previous work on spin flip rates induced by magnetic noise and consider the more complex geometries that are typically encountered in atom chips: layered structures and metallic wires of finite cross-section. We also discuss a few aspects of atom chips traps built with superconducting structures that have been suggested as a means to suppress magnetic field fluctuations. The thesis describes calculations of spin flip rates based on magnetic Green functions that are computed analytically and numerically. For a chip with a top metallic layer, the magnetic noise depends essentially on the thickness of that layer, as long as the layers below have a much smaller conductivity. Based on this result, scaling laws for loss rates above a thin metallic layer are derived. A good agreement with experiments is obtained in the regime where the atom-surface distance is comparable to the skin depth of metal. Since in the experiments, metallic layers are always etched to separate wires carrying different currents, the impact of the finite lateral wire size on the magnetic noise has been taken into account. The local spectrum of the magnetic field near a metallic microstructure has been investigated numerically with the help of boundary integral equations. The magnetic noise significantly depends on polarizations above flat wires with finite lateral width, in stark contrast to an infinitely wide wire. Correlations between multiple wires are also taken into account. In the last part, superconducting atom chips are considered. Magnetic traps generated by superconducting wires in the Meissner state and the mixed state are studied analytically by a conformal mapping method and also numerically. The properties of the traps created by superconducting wires are investigated and compared to normal conducting wires: they behave qualitatively quite similar and open a route to further trap miniaturization, due to the advantage of low magnetic noise. We discuss critical currents and fields for several geometries.

Zusammenfassung

Mikrotechnologische Oberflächen, sogenannte Atomchips, sind eine etablierte Methode zum Speichern und Manipulieren von Atomen geworden. Das hat Anwendungen in der Atom-Interferometrie, Quanteninformationsverarbeitung und Vielteilchensystemen vereinfacht. Magnetische Fallenpotentiale mit beliebigen Geometrien werden durch Atomchips mit miniaturisierten stromfhrenden Leiterbahnen auf einer Festkörperunterlage realisiert. Atome können bei Temperaturen im μ K oder sogar nK-Bereich in einer solchen Falle gespeichert und gekhlt werden. Allerdings können kalte Atome signifikant durch die Chip-Oberfläche gestört werden, die sich typischerweise auf Raumtemperatur befindet. Die durch thermische Strme im Chip erzeugten magnetischen Feldfluktuationen knnen Spin-Flips der Atome induzieren und Verlust, Erwärmung und Dekohärenz zur Folge haben. In dieser Dissertation erweitern wir frühere Arbeiten ber durch magnetisches Rauschen induzierte Spin-Flip-Ratenund betrachten kompliziertere Geometrien, wie sie typischerweise auf einem Atom-Chip anzutreffen sind: Geschichtete Strukturen und metallische Leitungen mit endlichem Querschnitt. Wir diskutieren auch einige Aspekte von Aomchips aus Supraleitenden Strukturen die als Mittel zur Unterdrückung magnetischer Feldfluktuationen vorgeschlagen wurden. Die Arbeit beschreibt analytische und numerische Rechnungen von Spin-Flip Raten auf Grundlage magnetischer Greensfunktionen. Fr einen Chip mit einem metallischen Top-Layer hängt das magnetische Rauschen hauptsächlich von der Dicke des Layers ab, solange die unteren Layer eine deutlich kleinere Leitfähigkeit haben. Auf Grundlage dieses Ergebnisses werden Skalengesetze für Verlustraten über einem dünnen metallischen Leiter hergeleitet. Eine gute bereinstimmung mit Experimenten wird in dem Bereich erreicht, wo der Abstand zwischen Atom und Oberfläche in der Grössenordnung der Eindringtiefe des Metalls ist. Da in Experimenten metallische Layer immer geätzt werden, um verschiedene stromleitende Bahnen vonenander zu trennen, wurde der Einfluss eines endlichen Querschnittsauf das magnetische Rauschen berücksichtigt. Das lokale Spektrum des magnetischen Feldes in der Nähe einer metallischen Mikrostruktur wurde mit Hilfe von Randintegralen numerisch untersucht. Das magnetische Rauschen hängt signifikant von der Polarisierung über flachen Leiterbahnen mit endlichem Querschnitt ab, im Unterschied zu einem unendlich breiten Leiter. Es wurden auch Korrelationen zwischen mehreren Leitern berücksichtigt. Im letzten Teil werden supraleitende Atomchips betrachtet. Magnetische Fallen, die von supraleitenden Bahnen im Meissner Zustand und im gemischten Zustand sind werden analytisch durch die Methode der konformen Abbildung und numerisch untersucht. Die Eigenschaften der durch supraleitende Bahnen erzeugten Fallen werden erforscht und mit normal leitenden verglichen: Sie verhalten sich qualitativ sehr ähnlich und

öffnen einen Weg zur weiteren Miniaturisierung von Fallen, wegen dem Vorteil von geringem magnetischem Rauschen. Wir diskutieren kritische Ströme und Felder für einige Geometrien.

Acknowledgments

First of all, I would like to thank my supervisors Prof. Martin Wilken and Dr. Carsten Henkel for giving me the opportunity to perform my PhD study in the Institute of Physics and Astronomy, Potsdam University. I will always be grateful for all their patient guidance and support. Particularly, I would like to thank Dr. Carsten Henkel for his patient discussion with me about my work in the past few years and for giving me the opportunities to present my work in several conferences, where I communicated with a lot of people in the relevant reserach domain.

I have had the luck and pleasure of working with a number of knowledgeable colleagues in the quantum optics group in Physics Institute, Potsdam University. I am grateful to Geesche Boedecker, Dr. Francesco Intravaia, Jürgen Schiefele and Holger Hoffmann, who were always available and heartily answered and discussed my questions about physics. I would like to thank Timo Felbinger for his kindly help with my problems of computer and mathematic softwares and also for his discussion about physics. I thank Harald Haakh for translating my abstract into german. I would like to express thanks, in alphabetical order, to Antonio Negretti, Maria Martin and Marc Herzog for their help both on study and daily life. I am indebted to our secretary Miss Marlies Path for her help with many practical work, such as work contract, insurance and so on.

I thank Elmar Haller, Dr. Peter Krüger and Prof. Jög Schmiedmayer for their experimental discussed data in the Chapter 1 and their fruitful discussion and collaboration. I also thank Valery Dikovsky, Vladimir Sokolovsky and Ron Folman for their fruitful collaboration and discussion about superconducting chips mainly by emails.

I would like to thank a few friends in Physics Institute who kept helping and encouraging me, Yin Chunhong, Zhou Yong, Li Ping and Wu Ye.

Finally, I give my thanks to my family. My parents have always encouraged and supported me all the time. My lovely son brings me a lot of fun. I thank my husband for his support.

Introduction

There has been a rapid development of trapping and manipulation of atoms on microfabricated solid-state surfaces, so called 'atom chips', in the past few years. Magnetic chip traps are now being implemented as the building blocks of the future quantum computers. Atom chips integrated with optical circuits also distribute coherent matter waves for interferometric and nanolithographic applications. Bose-Einstein condensation has been demonstrated on atom chips. Recently, trapped cold atoms have been investigated as new probes for electron current patterns and vortex dynamics.

Atom chip have opened novel directions by downscaling magneto-optical traps for ultra-cold atoms from the centimeter range to size of tens of microns and below. Quite arbitrary trap geometries can be designed with the help of miniaturized current-carrying wires on a chip that provide robust and steep magnetic potentials. These microfabricated conductors can carry large transport currents through small wire cross-sections, significantly increase magnetic field gradients and curvatures, leading to tighter confinements, large trap level spacing and small ground state size of atomic matter waves. In addition, they bring atoms closer to the conductors, which is helpful for miniaturization and integration. However, the proximity to the chip surface introduces additional decay channels. Magnetic field fluctuations lead to loss (decreasing the number of the trapped atoms), heating (increasing the temperature of the atoms) and decoherence (randomizing phases in superposition states). In particular, magnetic field fluctuations induced by thermally excited currents (Johnson noise) are most harmful at atom-surface distances of a few microns and limit the applications of atom chips, especiall when the long lifetime and coherence are required. Efforts have been taken on estimation, observation and reduction of these thermal noise. This is also the main theme of this thesis.

This thesis is built on previous work on thermal magnetic noise near solid surfaces. On theoretical side, Henkel *et al.* (1999) investigated the spin flip rate, as well as the heating, due to the thermal magnetic noise above a metallic surface (half-space). Decoherence due to magnetic field fluctuations has been estimated by Henkel *et al.* (2003). Rekdal *et al.* (2004) studied the thermal magnetic noise around a cylindrical conductor. Henkel (2005); Scheel *et al.* (2005) developed estimates for a thin conducting layer. On the experimental side, the loss induced by thermal currents in the conductors was observed by Jones *et al.* (2003); Harber *et al.* (2003). Lin *et al.* (2004); Zhang *et al.* (2005) performed experiments to study the loss rate due to thermal noise above a thin metallic layer. This thesis develops the theory for layered chips in a broader region of parameters. In additon, we address the important issue of metallic conductors with a finite lateral size, since these generically occur in real chip experiments.

Finally, we study in some detail superconducting wire structures and the magnetic traps that can be built from them. Superconducting chips have been proposed as a way to avoid thermal magnetic noise (Skagerstam *et al.*, 2006; Hohenester *et al.*, 2007), and technical noise can be reduced as well by using persistent currents, as shown experimentally by Mukai *et al.* (2007).

In the first chapter, we review the basic concepts of magnetic atom traps and guides and introduce a few simple atom devices such as beam splitter and interferometer. The miniaturization and integration of atom devices on a solid-state surface result in the 'atom chip'. We summarize the relevant parameter regions and outline the calculation of trap loss, heating, and decoherence rates and summarize previous results for the relevant magnetic noise spectra. Both thermal (Johnson) noise originating in the metallic chip components and technical noise from the supplies exterior to the chip are estimated.

In the second chapter, we focus on the lifetime of atoms trapped above a layered structure. The loss rate due to spin flips induced by the thermal magnetic noise depends on both the atomic dipole moment and magnetic field fluctuation sprectrum. We first simplify the internal matrix elements and then study the thermal magnetic noise. For comparison, we review the properties and scaling laws for atoms trapped above a bulk metal. The skin depth of the materials is identified as a characteristic scale. The lifetime of atoms trapped above layered structures are computed semi-analytically by means of the exact magnetic Green function and multi-layer reflection coefficients. The impact of a finite thickness of the metallic layer and the properties of sublayers on the trap lifetime are considered. The scaling laws for atoms trapped above a thin metallic layer are developed, providing a simple analytical approximations for the loss rate. Finally, we discuss a relevant experiment performed in the group of Jörg Schmiedmayer and compare our results with the experimental data.

In the third chapter, the impacts of the finite width of conductors on the magnetic noise are considered within a two-dimensional model. Magnetic noise around a metallic conductor with arbitrary cross-section is computed with the help of boundary integral equations. The singularities of the integral kernels are extracted and estimated. The magnetic noise around a cylindrical metallic wire is computed numerically as an example and compared with analytical results to validate our numerical method. We then compute the magnetic noise around a rectangular wire to see the impact of the finite width. We find that the finite width reduces magnetic noise and makes it strongly dependent on polarization. Finally, the interactions between multiple wires are studied.

In the last chapter, superconducting chips are investigated as an promising way to significantly reduce the magnetic noise. A self-consistent numerical calculation of magnetic field and supercurrents around superconductors in the Meissner state is derived. The supercurrent distributions in a superconducting wire with rectangular cross section are also computed analytically by means of conformal mapping. Properties of magnetic traps produced by superconducting wires with different shape are studied. We identify additional potential barriers near the wire edges induced by the screnning currents, that may have an impact on loading and manipulation atoms. The critical values of the transport current and external magnetic field are roughly estimated for a few geometries.

We conclude our work and outline our future interests at the end of the thesis.

Contents

Chapter 1

Magnetic traps for ultracold atoms

In this chapter we first give a basic description of magnetic traps and guides with arbitrary geometries, then go to atom chips where these traps are integrated onto a solid surface. Finally we discuss the interaction between atoms and the surfaces of atom chips, which plays an important role for trap lifetimes.

1.1 Introduction

Static magnetic fields were first applied to trap neutral particles by Krugler *et al.* (1978); Paul (1990). This technique then developed for trapping and manipulating atoms in magnetic potentials generated by a normal conductor (Migdall *et al.*, 1985) and by superconducting electromagnets (Hess *et al.*, 1987). Magnetic trapping potentials may act as simple Dewar container for storing cold atoms at microkelvin temperatures and even below. Gases of alkali-metal atoms have been trapped and cooled below the critical temperature for Bose-Einstein condensation in magnetic traps (Cornell & Wieman, 2002; Ketterle, 2002). The miniaturization and integration of magnetic traps and other devices on solid-state surface result in the 'atom chip' (Folman *et al.*, 2000). It can provide magnetic potentials of almost arbitrary geometries with microfabricated conducting wires. Steeper magnetic traps can be obtained on atom chips, since the microfabricated wires can carry larger current density through smaller cross sections and bring atoms closer to the chip surface where the field gradients are larger. Atom chips significantly simplify the trap setup (Reichel *et al.*, 1999) and effectively accelerate the condensation process (Hänsel *et al.*, 2001) compared to typical experiments and all-optical BEC (Barrett *et al.*, 2001). In addition, microfabrication techniques make it possible to integrate complex systems of multiple microscopic traps, wave guides and other atom optical devices on a single trapping chip (Folman *et al.*, 2002; Fortágh & Zimmermann, 2007). It makes atom chips attractive for a wide range of applications including quantum information processing with neutral atoms (Schmiedmayer *et al.*, 2002), integrated atom optics, matter-wave interferometry, compact atomic clocks (Treutlein *et al.*, 2004) precision force sensing, and studies of the interaction between atoms and surfaces.

However, magnetic field fluctuations do perturb the atoms trapped close to the chip surface at short distances and give rise to loss (reduction of the number of the atoms), heating (increas-

ing the temperature of the atoms) and decoherence (inducing a phase shift). Most of all, the magnetic noise arising from the thermally excited currents in the chip surface has a dominant impact on the trap lifetime and coherence and imposes ultimate limit to the trap-surface distance (Henkel *et al.*, 1999; Zhang *et al.*, 2005). These magnetic field fluctuations are stopping miniaturization and should be controlled for certain applications of atom chips (Harber *et al.*, 2003) which require long trap lifetime and coherence. In this chapter, we first introduce some basic magnetic atom guides and traps, atom devices and atom chips, then give some estimations of trap loss, heating and decoherence due to the magnetic field fluctuations. The material has been extracted from the review papers by Folman *et al.* (2002) and Fortágh & Zimmermann (2007).

1.2 Magnetic interaction

An atom with total spin $\mathbf{F}$ and magnetic moment $\boldsymbol{\mu} = g_F \mu_B \mathbf{F}$ in a magnetic field $\mathbf{B}$ experiences the Zeeman interaction

$$V_Z = -\boldsymbol{\mu} \cdot \mathbf{B} = -g_F \mu_B m_F B \,, \tag{1.1}$$

where μ_B is the Bohr magneton, g_F the Landé factor of the atomic hyperfine state, and m_F the magnetic quantum number. In the second equality, we use an adiabatic approximation where the magnetic moment $\boldsymbol{\mu}$ follows the direction of the magnetic field $\mathbf{B}$ adiabatically and m_F is a constant of motion. This is appropriate when discussing a trap in a static magnetic field. Then the potential V_Z is proportional to the modulus of the magnetic field $B = |\mathbf{B}|$. If the magnetic moment is parallel to the magnetic field and in the same direction, the magnetic potential V_Z is negative and minima of the potential energy are given by the maxima of the magnetic field modulus. An atom prefers the lowest energy state, and is therefore drawn towards the maxima of the field: this atom is in a strong-field-seeking state. In order to trap atoms in the strong-field-seeking state, a source of the magnetic field, such as a current-carrying wire, has to be located inside the trapping region, which is inconvenient for trapping and manipulating atoms (Schmiedmayer, 1995; Denschlag *et al.*, 1999). In contrast, if the magnetic moment is in the opposite direction to the magnetic field, the magnetic potential V_Z is positive and minima of the potential are also the minima of the field. An atom is then drawn towards the lowest magnetic field: it is in a weak-field-seeking state (Folman *et al.*, 2002). These traps are most common for neutral atoms because atoms can be trapped at a finite distance from the source of magnetic field.

1.3 Atom guides

1.3.1 Kepler guide

A simple trap for an atom in the strong-field-seeking state can be formed by a current-carrying wire, which makes the atom orbit around it (Vladimirskii, 1961; Schmiedmayer, 1992, 1995) (see Fig. 1.1).

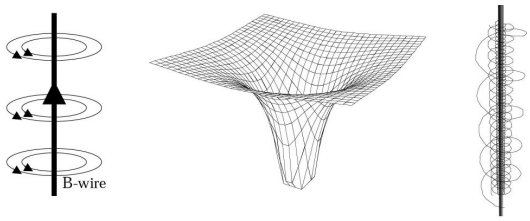

Figure 1.1: Guiding the atoms in their strong-field-seeking state as they circle around the wire. Left: current-carrying wire and magnetic field. Middle: magnetic potential. Right: typical trajectories of atoms. From Folman *et al.* (2002).

The adiabatic interaction potential is given by

$$V_Z = -\boldsymbol{\mu} \cdot \mathbf{B} = -\frac{\mu_0 g_F \mu_B m_F}{2\pi r} I_w \,, \tag{1.2}$$

where I_w is the transport current through the wire, r the distance from the wire center, and μ_0 the vacuum permeability. V_Z corresponds to a two-dimensional scalar Coulomb $(1/r)$ potential, in which atoms move in Kepler orbits. Hence this kind of guide is called 'Kepler guide'. If a thin wire carries a current $I_w = 1\mathrm{A}$ and a Rb atom in the $|F = 2, m_F = 1\rangle$ state is trapped at $1\mathrm{mm}$ away from the center of the wire, typically the trap depth has a magnitude of $100\mu\mathrm{K}$, sufficiently deep to trap atoms.

1.3.2 Side guide

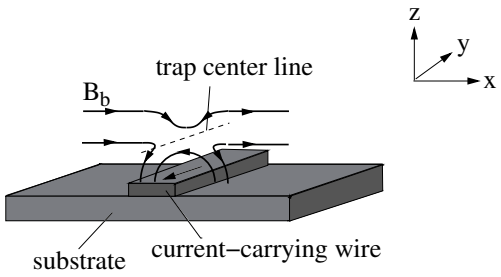

Figure 1.2: Guiding the atoms in their weak-field-seeking state along the dashed line above the current-carrying wire in a homogeneous bias field.

It was first pointed out by Frisch & Segrè (1933) that a straight current-carrying wire $\mathbf{I}_w = I_w \mathbf{e}_y$ placed in a homogeneous bias field $\mathbf{B}_b = B_b \mathbf{e}_x$ in a direction perpendicular to the wire can generate a quadrupole field with a well-defined two-dimensional field miminum, as shown in Fig. 1.2. This idea provides the basic concept for most of the magnetic microtraps implemented with atm chips. We assume , to begin with, that the guiding wire is a infinitesimally thin cylinder (the radius is much smaller than the trap height) and infinitely long. The total magnetic field is

$$\mathbf{B}(x, z) = \mathbf{B}_b + \frac{I_w \mu_0 (x\mathbf{e}_z - z\mathbf{e}_x)}{2\pi r^2} \,, \tag{1.3}$$

where $r = \sqrt{x^2 + z^2}$ is the distance from the origin (the center of the wire) to the evaluation point, axes as in Fig. 1.2. The magnetic field vanishes at a line parallel to the wire at the position $(x, z) = (0,\ I_w\mu_0/2\pi B_b)$ and forms a magnetic guide. Weak-field-seeking atoms are trapped radially in the xz plane around this line. For convenience, we use cylindrical coordinates (r', φ) with the origin at the field minimum to describe the magnetic field modulus (Fortágh & Zimmermann, 2007):

$$B(r', \varphi) = \frac{I_w\mu_0}{2\pi d} \frac{r'}{\sqrt{r'^2 + d^2 + 2r'd\cos(\varphi)}} \,. \tag{1.4}$$

The angle φ is defined relative to the z axis, $\varphi = 0$ parallel to the z axis in Fig. 1.2. d denotes the distance between the wire and trap center. The gradient at the trap center is independent of φ (Fortágh & Zimmermann, 2007):

$$\frac{\mathrm{d}B}{\mathrm{d}r}\Big|_{r=0} = \frac{B_b}{r_0} = \frac{\mu_0 I_w}{2\pi r_0^2} \,. \tag{1.5}$$

At the trap center, the spin states of the atoms may flip due to Majorana transitions, weak-field-seeking atoms change into strong-field-seeking atoms and escape from the trap (Sukumar & Brink, 1997). Adding a small magnetic field B_{ip} along the wire (y) direction can circumvent this loss mechanism by lifting the energetic degeneracy between the trapped and untrapped states. The resulting potential is conventionally called a Ioffe-Pritchard trap (Pritchard, 1983). At the same time, this samll magnetic field B_{ip} turns the linear trapping potential into a harmonic one. The harmonic guide is then characterized by the curvature in the transverse directions (Folman *et al.*, 2002)

$$\frac{\mathrm{d}^2B}{\mathrm{d}r^2}\Big|_{r=0} = \frac{B_b^2}{r_0^2 B_{ip}} = \frac{\mu_0^2 I_w^2}{4\pi^2 B_{ip} r_0^4} = \frac{4\pi^2 B_b^4}{\mu_0 B_{ip} I_w^2} \,. \tag{1.6}$$

The harmonic oscillation frequency is

$$\omega = \sqrt{\frac{\mu_B g_F m_F}{M} \left(\frac{\mathrm{d}^2B}{\mathrm{d}r^2}\right)} \propto \frac{B_b^2}{I_w} \,, \tag{1.7}$$

Where M is the mass of the atom.

1.3.3 Two-wire guides

Co-propagating currents

The magnetic fields formed by two parallel wires carrying equal co-propagating currents vanishes along the central line between the wires and increases and changes direction like a two-dimensional quadrupole. It can guide atoms around curves as shown in Fig. 1.3. A small horizontal (vertical) bias magnetic field displaces this waveguide vertically (horizonally). Such a configuration was used by Müller *et al.* (1999) to transport atoms between two vacuum chambers along a total guiding distance of $10\mathrm{cm}$.

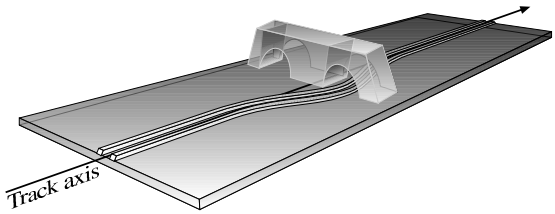

Figure 1.3: Two wires with co-propagating currents. Atoms can be guided around curves along the central line between the two wires. From Müller *et al.* (1999)

By adding an additional magnetic field parallel to the plane of the wires, different guides can be formed according to the modulus of the bias field B_b (Hinds *et al.*, 2001). There is a critical field B_0

$$B_0 = \frac{\mu_0 I_w}{\pi d} \,, \tag{1.8}$$

where d is the distance between the two wires. In the regime $B_b < B_0$, there are two lines of vanishing magnetic field in the symmetry plane between the wires, i.e., two linear quadrupole waveguides which can be made harmonic by superimposing an axial offset field. Taking the origin at the center of the two wires, the positions of the guide centers are given by

$$x = 0, \qquad z = \frac{dB_0}{2B_b}\left(1 \pm \sqrt{1 - \left(\frac{B_b}{B_0}\right)^2}\right) \,. \tag{1.9}$$

The two-wire guide shown in Fig. 1.3 does apply the lower trap position defined by the above equation. The corresponding gradient amounts to

$$b = \frac{2B_0}{d}\sqrt{1 - \left(\frac{B_b}{B_0}\right)^2}\left(1 \mp \sqrt{1 - \left(\frac{B_b}{B_0}\right)^2}\right) \,. \tag{1.10}$$

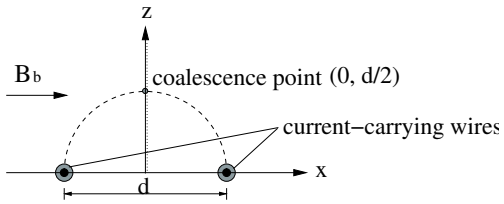

Figure 1.4: Two wires carry co-propagating currents in a lateral bias field. When $B_b < B_0$, two atom guides are on the z axis; if B_b increases, the two guides get closer, and merge into one when $B_b = B_0$ at point $(0, d/2)$, d is the distance between the two wires; if B_b continuously increases, the atom guide seperates into two again along the dashed semicircle.

If $B_b = B_0$, the two waveguides merge and form a hexapole waveguide. In the regime $B_b > B_0$, the hexapole waveguide falls apart into two quadruple ones again, each approaching

one of the wires on a semicircular trajectory, as shown in Fig. 1.4. The coordinates of the waveguide centers are

$$x = \pm\frac{dB_0}{2B_b}\left(\sqrt{\left(\frac{B_b}{B_0}\right)^2 - 1}\right) \quad , \quad z = \frac{dB_0}{2B_b} \; . \tag{1.11}$$

In this case, the field gradient is identical in both waveguides:

$$b = \frac{2B_b}{d}\sqrt{\left(\frac{B_b}{B_0}\right)^2 - 1} \; . \tag{1.12}$$

This configuration has been used to split Bose-Einstein condensates (Shin *et al.*, 2005).

Counter-propagating currents

In contrast, two parallel wires carrying counter-propagating equal current I_w with a bias field perpendicular to the plane of the wires, also form similar guides (Thywissen *et al.*, 1999). Now the critical field becomes

$$B_0 = \frac{2\mu_0 I_w}{\pi d} \; . \tag{1.13}$$

In the regime $B_b < B_0$, the two linear quadrupole atom guides are on the z axis

$$z = \pm\frac{d}{2}\sqrt{\frac{B_0}{B_b} - 1} \; . \tag{1.14}$$

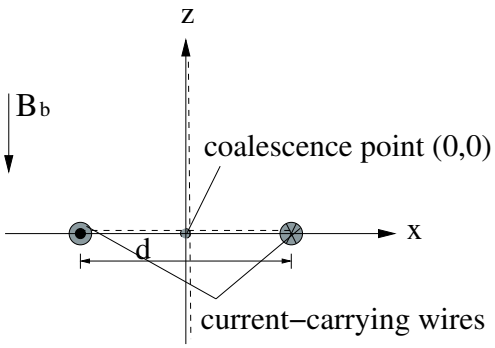

Figure 1.5: Two wires with counter-propagating currents guide atoms in a perpendicular bias field. d is the distance between the two wires. Again if $B_b < B_0$, there are two atom guides on the z axis; if B_b increases, the two guides move together along the z axis and merge into a single one at the middle point, then if B_b increases continuously, the guide seperates into two again and each moves in the wire plane towards the wire.

They approach the wire plane along the z axis as shown in Fig. 1.5 by increasing the bias field B_b and merge at $z = 0$ when $B_b = B_0$. In the regime $B_b > B_0$, the atom guide separates

into two again and each one moves in the wire plane towards one of the wires. The positions of the guide centers are given by

$$x = \pm\frac{d}{2}\left(1 - \sqrt{1 - \frac{B_0}{B_b}}\right) , \quad z = 0 . \tag{1.15}$$

Guiding of ultracold atoms using this scheme on an atom chip was demonstrated in Dekker *et al.* (2000). The advantage of this configuration and Fig.1.4 is that they can bring atoms close to the chip surface between the wires in a controlled way.

1.3.4 Guides with integrated bias field

It is convenient if the bias fields used in the above configurations can be generated on the chip. For the side guide formed by a current-carrying wire and an external field as described in Sec.1.3.2, the homogeneous bias field can be formed by two additional wires on the each side of the guiding wire. The direction of the currents in these wires has to be opposite to the current in the guiding wire. Three wires can be mounted on the same chip to get a self-sufficient guide (Cassettari *et al.*, 2000a), as shown in the left of Fig. 1.6. Similarly, the guides, as described in Sec.1.3.3, formed by two parallel wires carrying counter-propagating currents and a bias field, can be also formed by four wires in one plane, as shown in the right of Fig. 1.6. The two outer wires contribute the bias field. This configuration provides a tighter confinement than the former one. Guiding of atoms in a four-wire guide on a chip was demonstrated by Dekker *et al.* (2000).

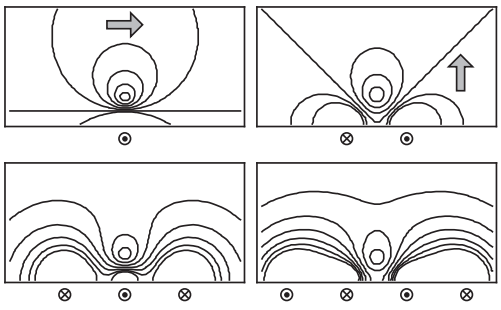

Figure 1.6: Magnetic potential above integrated wires. Upper left: a side guide formed by a current-carrying wire and a bias field perpendicular to the wire. The bias field can be replaced by two wires carrying opposite currents as lower left. Upper right: a side guide formed by two wires with counter-propagating currents in a bias field penpendicular to the wire plane. Similarly, the external bias field can be replaced by two wires carrying currents opposite to the neighbour one. From Cassettari *et al.* (2000b)

1.4 Atom traps

An easy way to create a magnetic trap is adding some 'endcaps' to the above atom guides. For example, a three-dimensional magnetic trap can be made by bending the current-carrying wire of the side guide described in Sec.1.3.2 (Reichel *et al.*, 1999; Haase *et al.*, 2001). The magnetic field from the bent leads creates pot barriers for the wire guide, confining the atoms along the central part of the wire (see Fig. 1.7). The size of the trap along this axis is then determined by the distance between the endcaps. There are two different geometries, 'U' and 'Z' traps, which are used in a large number of experiments for the axial termination of magnetic guides and for intermediate trapping as part of the loading procedure of microtraps.

1.4.1 U trap

Bending the both ends of a current-carrying wire in the same direction to form a 'U', as shown in the left of Fig. 1.7, creates a magnetic field that in combination with a homogemeous bias field forms a three-dimensional quadrupole trap. The bend leads result in a field configuration where a rotation of the bias field displaces the trap center but the field always vanishes completely at this position. A thermal gas can be stored in such a trap; however, a Bose-Einstein condensate would rapidly decay because of Majorana spin flips.

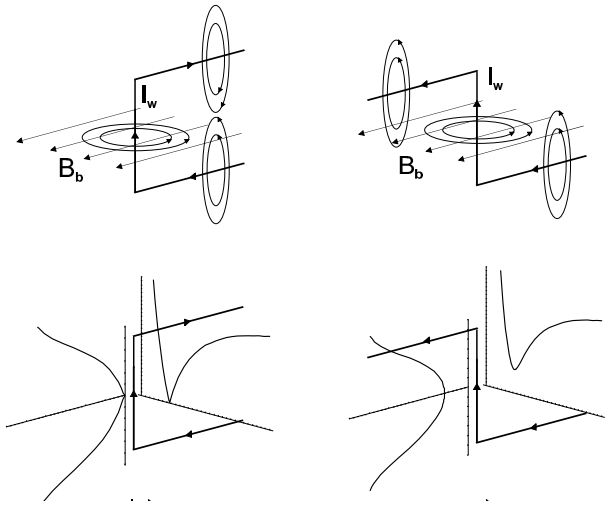

Figure 1.7: Left: 'U' trap with a zero minimum in the trapping center. Right: 'Z' trap with a nonzero minimum in the trapping center (Ioffe-Pritchard trap). From Folman *et al.* (2002)

1.4.2 Z trap

Bending both ends of a current-carrying wire in opposite directions to form a 'Z', as shown in the right of Fig. 1.7, creates a nonzero minimum at the trap center. When the bias field is parallel to the leads, this configuration creates a Ioffe-Pritchard trap. The potentials for the 'U'

and ‘Z’ trap scale similarly as for the side guide, but the finite length of the center bar and directions of the bending leads have to be taken into account. Simple scaling laws only hold as long as the distance of the trap center from the centeral wire is small compared to the length of the central bar (Cassettari *et al.*, 2000b; Haase *et al.*, 2001). Bending both ‘Z’ leads once more results in three parallel wires, which generate a self-sufficient ‘Z’ trap (Folman *et al.*, 2002).

1.5 Beam splitters

By combining two of the atom guides described in Sec.1.3, it is possible to design potentials where at some point two different paths are available for the atoms.

1.5.1 Y splitter

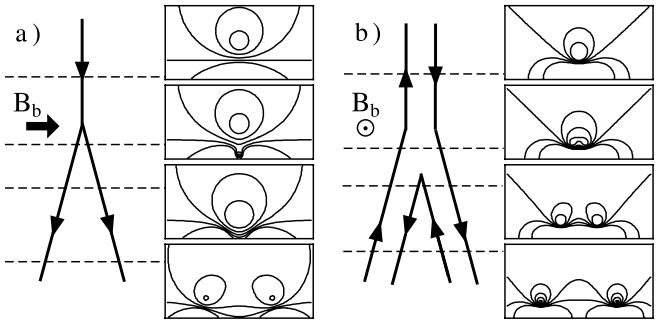

Figure 1.8: Magnetic potential at different points of a Y splitter. (a) A Y splitter is realized by a single wire which is split into two and placed in a horizontal bias field. (b) A Y spliter is realized by two parallel wires carrying current in opposite directions and placed in a vertical bias field. The input and output guides have identical characteristics. From Cassettari *et al.* (2000b)

Two side guides are merged into one to form a Y-shape beam splitter as shown in Fig. 1.8a. This has been investigated theoretically and experimentally by Cassettari *et al.* (2000a); Müller *et al.* (2000). This Y-shape splitter has one main input guide, which is the central wire of the Y, and two output guides corresponding to the left and right wires. On the input side a fourth ‘blind’ guide emerges out of the plane of the wires, i.e. from the surface of the chip, and joins the other three guides at the splitting point. The distances of the input and blind guides from the surface are

$$z_{\pm} = \frac{1}{2}\left(d_{split} \pm \sqrt{d_{split}^2 - d^2}\right) , \tag{1.16}$$

where d is the distance between the outgoing wires and

$$d_{split} = \frac{\mu_0 I_w}{\pi B_b} \,. \tag{1.17}$$

The input and blind guides merge at $d = d_{split}$ where the atom beam is split. By controlling the currents in the wires, atoms can be directed to the output arms of the Y with any desired ratio. It is the simplest beam splitter. The blind guide can be avoided by using the configuration shown in Fig. 1.8b. This double-wire geometry combined with a bias field perpendicular to the plane of the wires has a better symmetry than the one shown in Fig. 1.8a.

1.5.2 X splitter

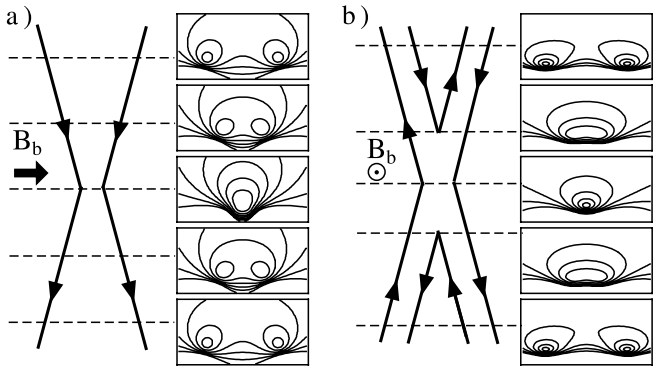

Figure 1.9: Magnetic potential at different points of a X splitter or coupler. (a) A two-wire X splitter. The two wires carry co-propagating currents and get closer, but do not touch each other in a horizontal bias field. (b) A four-wire X splitter formed by two two-wire counter-propagating side guides. From Cassettari *et al.* (2000b)

Another splitter geometry is based on the tunneling effect: two wires approach but not touch each other in a parallel bias field as shown in Fig. 1.9a. If the distance between the wires d is as small as d_{split}, the two waveguides above the wires merge and form a junction with four ports. Otherwise, if the closest separation between the wires is slightly larger than d_{split}, the atoms may tunnel between the guides similar to optical couplers in fiber optics. Similar atom splitter can be constructed with pairs of wires as shown in Fig. 1.9b, which has a better symmetry. In both cases, the wire currents and the bias field govern the splitting ratio in the output wires. And the potential shape in the inputs and outputs keeps exactly the same all over the splitting region compared to Y-shape splitters.

1.6 Interferometers

Using the above multiple-guide potentials and time dependent potentials which are able to split minima in two and recombine them as described in Sec.1.3.3, several kinds of chip-based atom interferometers have been investigated recently (Hänsel *et al.*, 2001; Andersson *et al.*, 2002; Negretti, 2005). We give two examples here.

1.6.1 Spatial interferometers

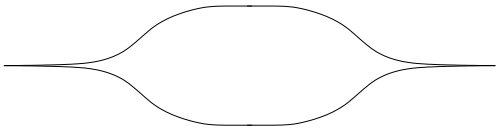

Figure 1.10: Sketch of a spatial interferometer. The simplest interferometer is realized by two Y splitters joined back to back. The first acts as splitter, and the second acts as recombiner. The output transverse states depend on the phase shift during transport along the two paths.

Two Y-beam splitters can be joined back to back as shown in Fig. 1.10 to form a multimode atomic interferometer (Andersson *et al.*, 2002). The first Y acts as splitter and the second as recombiner. The transverse modes in the input channel can be classified by their parity. Neighboring states with different parity become degenerate in that part of the interferometer where the two paths are well separated. For an adiabatic transport through the interferometer without any asymmetric perturbations, no transitions between the transverse states occur and the interferometer can be decomposed into independent two-state interferometers. The occupation of the two states in the output channel of each interferometer depends on the relative phase shift accumulated during the transport. An even phase shift of $2n\pi$ recovers the incoming states while an odd one of $(2n+1)\pi$ swaps the population of the two incoming states.

1.6.2 Temporal interferometers

A time-dependent atomic interferometer can be realized by using two parallel wires with co-propagating currents (Hinds *et al.*, 2001) as discussed in Sec.1.3.3. Changing the bias field one can split and recombine the potential minima as shown in Fig. 1.11. Starting with $B_b < B_0$ and an atom cloud in the ground state of the upper minimum, the corresponding wave function can be coherently split when B_b becomes larger than B_0. Then two spatially separated parts are obtained. If B_b is lowered again to $B_b = B_0$, the two parts are recombined. The result depends on the relative phase shift between the two spatially separated parts. If the phase shift is $2n\pi$, the ground state is recovered; otherwise, if the phase shift is $(2n+1)\pi$, the first excited state is achieved. Other value of the phase shift results in a superposition of the ground and first excited states.

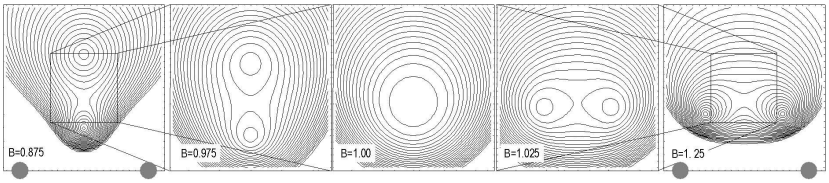

Figure 1.11: Equipotential lines of a temporal interferemeter formed by a two-wire side guide. The currents in both wires run in the same direction, the bias field is parallel to the wire plane. Denote $B = B_b/B_0$, when $B < 1$, there are two guides on y axis; increasing the bias field B_b, the two guides move towards each other vertically, and get together when $B = 1$; when $B > 1$, it is split into two laterally; then if lower the bias field to $B = 1$ again, two guides are recombined again. The final states depend on the phase shift of the two parts. From Folman *et al.* (2002)

1.7 Atom chips

To achieve versatile and highly controlled atom manipulation one would like to confine atoms in steep traps or guides which are small and precisely located. It turns out that this is possible in the near field of miniaturized complex structures, integrated into a solid-state surface, a concept that has been known as 'atom chips'. Microfabricated current-carrying wires on the chip surfaces can be designed to provide arbitrary magnetic trapping potential. In addition, these microscale wires can carry much higher current density, which is the key factor in creating a steep trap, with reasonable energy consumption, in contrast to free-standing current-carrying wires. The chip substrate is quite helpful to sustain high current densities, because it also serves as a heat sink. Together with the small cross-section, the microfabricated wires may produce larger magnetic field gradient and curvatures, hence a tighter confinement. To illustrate this, let us consider a side guide potential based on a flat guiding wire with a width $2w$ and carrying a current I. The magnetic field gradient increases as the atom-surface distance decreases till it is comparable to the wire width $2w$. The further reduction of the atom-surface distance will not significantly increases the magnetic field gradient. The required bias field for such a side guide trap at height $\sim w$ is proportional to $I/2w$ (Fortágh & Zimmermann, 2007), hence to the current density j at fixed thickness. Consequently, the largest possible field gradient depends on the ratio $j/2w$ which favours small wires, such as microfabricated wires on atom chips. In conclusion, the smaller the width and the shorter the atom-surface distance, the larger the field gradients and curvatures are. The drive for smaller width is stopped at a distance of about 100nm where surface decoherence effects and Van der Waals forces become so strong that they destabililize the trap. Ground-state sizes smaller than 10nm (Folman *et al.*, 2002) can be obtained in such steep chip traps. The resulting large trap level spacings help to suppress heating processes since the trapped particles decouple from low-frequency fluctuations.

Thanks to precise micro- and nanofabrication technology, conducting wires can be mounted on chips with an accuracy of $< 100\mathrm{nm}$. This, together with the small ground state size, allows one to know the exact positions of atoms on the chip surface, which may help to better control and manipulate atoms. In addition, microoptical devices and other devices can be integrated on the same monolithic chip, which opens a wide range of applications from matter wave

optics to quantum information processing. This high degree of integration unavoidably leads to multilayer atom chips, we study a simple example in Chap.2.

1.8 Electromagnetic field fluctuations

The shorter the atom-surface distances, the larger the magnetic field gradients, and the tighter the confinement that can be obtained for atoms. Cold atoms are therefore expected to be trapped and manipulated a few microns above a 'hot' chip surface. However, at such short distances, cold atoms are strongly disturbed by the surface through fluctuating electromagnetic fields. These may give rise to loss (reduction of the number of trapped atoms), heating (increasing of the temperature of atoms) and decoherence (inducing an uncertain phase). The electromagnetic field fluctuations limit the atom confinement and the atom-surface distance, they must be taken care of in applications of atom interferometry, quantum information processing and other atomic devices. This is a main theme of this work.

The fluctuating electromagnetic fields near the chip surface may induce atomic energy shifts and give rise to forces between atoms and surfaces, which is known as Van der Waals and Casimir-Polder forces. The energy shift due to the electric dipole polarizability leads to an attractive force between atoms and surfaces. It has been measured recently at distances of a few microns where it represents only a weak perturbation of the trapping potential (Harber *et al.*, 2005). At shorter distances, its magnitude increases as $1/z^3$ (Grimm & Ovchinnikov, 2000) and plays an important role at distances of the order of $100\mathrm{nm}$. It is difficult to trap atoms closer than $100\mathrm{nm}$ to the chip surface, because at this short distance Van der Waals forces become larger enough to attract the atoms to the chip surfaces. An energy shift due to the magnetic dipole polarizability exists as well and generates a repulsive force between atoms and surfaces, but its magnitude is much smaller than the electric one and does not modify significantly the trapping potentials (Henkel *et al.*, 2005).

In most recent atom chip experiments, atoms are trapped and manipulated at a few microns away from the chip surfaces. Let us focus on the traps at this distance. Van der Waals forces become so small that they are negligible. However, magnetic field fluctuations in the trap strongly perturb the trapped atoms. They induce transitions between internal spin states, leading to loss of atoms and decoherence of the internal states, and drive transitions between vibrational states of the trap, leading to heating and decoherence of the center-of-mass motion. In this section, we focus on the evaluation and comparison of these harmful effects of magnetic field fluctuations.

1.8.1 Trap loss

In free space, magnetic field fluctuations duo to thermal blackbody radiation at low frequency are too weak to induce a transition between atomic internal spin states on laboratory time scale. The presence of a dielectric or metallic surface significantly enhances magnetic field fluctuations (Purcell *et al.*, 1946), opens additional decay channels and increases the transition rate. In atom chips, this magnetic noise is induced by the thermal currents in the chip elements (Johnson noise) and dominates over magnetic noise in free space. In this section, we consider

magnetic field fluctuations produced by Johnson noise in the metallic substrate and also by technical noise in the wire currents. Recall the Zeeman interaction of an atom in a magnetic field Eq.(1.1),

$$V_Z(\mathbf{r},t) = -\boldsymbol{\mu}\cdot(\mathbf{B}_s(\mathbf{r}) + \mathbf{B}_{fl}(\mathbf{r},t)) \;, \tag{1.18}$$

where $\boldsymbol{\mu}$ is the magnetic dipole moment and $\mathbf{r}$ its (center of mass) position, $\mathbf{B}_s(\mathbf{r})$ is the static field which provides a trap for cold atoms, $\mathbf{B}_{fl}(\mathbf{r},t)$ the fluctuating field which represents the magnetic noise. For a trapped atom in a weak-field-seeking state, a loss process occurs when the fluctuating field $\mathbf{B}_{fl}(\mathbf{r},t)$ induces a transition $|i\rangle \rightarrow |f\rangle$ of the atom to a strong-field-seeking state (magnetic moment parallel to the trapping field $\mathbf{B}_s(\mathbf{r})$) (see Fig. 1.12). The magnetic potential then has the opposite sign, and the atom is rapidly expelled from the trap. These spin flips are described by the interaction Hamiltonian (1.18), and are induced by fields with a frequency around the Larmor frequency $\omega_L = (E_f - E_i)/\hbar$. A calculation of the transition rate based on Fermi's Golden Rule yields

$$\Gamma_{i\rightarrow f}(\mathbf{r}) = \sum_{\alpha\beta} \frac{\langle i|\mu_\alpha|f\rangle\langle f|\mu_\beta|i\rangle}{\hbar^2} S_B^{\alpha\beta}(\mathbf{r};-\omega_L) \;, \tag{1.19}$$

where $S_B^{\alpha\beta}$ is the magnetic field fluctuation spectrum evaluated at the transition frequency.

$$S_B^{\alpha\beta}(\mathbf{r},\omega_L) = \int_{-\infty}^{+\infty} \mathrm{d}\tau \; \langle B_{fl}^{\alpha}(\mathbf{r},t+\tau) B_{fl}^{\beta}(\mathbf{r},t)\rangle e^{i\omega_L\tau} \;. \tag{1.20}$$

Only the fluctuating field $\mathbf{B}_{fl}(\mathbf{r},t)$ is relevant, here, as the static field has no contribution to the magnetic field fluctuation spectrum at nonzero frequency. The spectrum is taken at the trap center $\mathbf{r}$, assuming that the spatial extension of the trap is sufficiently small, compared to the scale on which S_B varies.

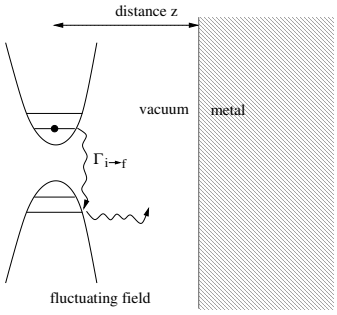

Figure 1.12: An atom is trapped at a certain distance away from a surface. The trap potential depends on the internal atomic states. If the state is changed due to the fluctuating field, the atom may be strongly perturbed and lost from the trap.

Surface noise

Since the effect of blackbody radiation is small enough to be negligible, the near field generated by the surface gives the dominant contribution to the magnetic noise, hence the transition rate. Here we focus on the magnetic noise induced by a metallic surface at a room temperature. Henkel *et al.* (1999) have investigated the loss rate of atoms above a half space due to the magnetic near-field noise. The loss rate increases rapidly as the atom-surface distance decreases. The magnetic field fluctuation spectrum depends on the imaginary part of the complex permittivity $\epsilon(\mathbf{r},\omega) \approx 2\mathrm{i}/k^2\delta^2$, where k is the wave vector and $\delta = \sqrt{2\epsilon_0\varrho\omega}/k$ the skin depth, a characteristic length scale on which an electromagnetic field entering a metal is damped. (ϱ is the conductivity of the metal.) Typically, for a gold surface $\varrho = 1.7 \times 10^{-6}\Omega$ cm and $\delta = 70\mu$m, when we consider a Larmor frequency $\omega_L/2\pi = 5$MHz. In the high temperature limit ($k_B T_s \gg \hbar\omega_L$) and at low trap height ($z \ll \delta$), the thermal magnetic field spectrum above a half space is given by (Henkel *et al.*, 1999)

$$S_B^{\alpha\beta}(\omega_L, z) = \frac{\mu_0 k_B T_s}{16\pi\omega_L\delta^2 z} s_{\alpha\beta} \ , \tag{1.21}$$

where z is the atom-surface distance, k_B is the Boltzmann constant, T_s the temperature of the substrate and $\hbar$ the Planck constant, $s_{\alpha\beta}$ is a diagonal tensor with the elements $s_{xx} = s_{yy} = 1,\ s_{zz} = 2$. The strength of thermal noise depends on the atom-surface distance and the skin depth. In the opposite region $z \gg \delta$, the magnetic field fluctuation spectrum must be multiply with a factor $(\delta/z)^3$, and become much smaller. This limit also describes a superconductor (δ becomes small). When an atom is trapped at 10μm away from the surface, the magnetic noise power is $\sqrt{S_B} \sim (\mathrm{pT}/\sqrt{\mathrm{Hz}})$. For a magnetic moment being of the order of the Bohr magneton μ_B, this translates into a loss rate of a magnitude $10\mathrm{s}^{-1}$ (Folman *et al.*, 2002).

The loss rate above a planar surface induced by the thermal current noise has been observed experimentally by (Jones *et al.*, 2003; Harber *et al.*, 2003). Loss rates for other geometries have been studied also: Rekdal *et al.* (2004) have computed the thermal magnetic noise around a cylindical wire; Scheel *et al.* (2005) have predicted the trap lifetime above a thin film, while Lin *et al.* (2004) have done the relevant experiment. A thin metallic layer can help to reduce the thermal noise and increase the trap lifetime (Zhang *et al.*, 2005). We discuss this in more detail in Chap.2.

Technical noise

Current fluctuations in the chip wires due to the instability of the supply can generate magnetic field fluctuations and induce loss processes. The noise spectrum of the driving current I_w is denoted by $S_I(\omega_L)$. Neglecting the finite wire size, the magnetic field at distance z is $B_w = \mu_0 I_w/2\pi z$. Within the low frequency approximation $w_L z/c \ll 1$, the magnetic field fluctuation spectrum is given by (Henkel *et al.*, 2003)

$$S_B^{\alpha\beta} = \left(\frac{\mu_0}{2\pi z}\right)^2 S_I(\omega_L) t_{\alpha\beta} \ , \tag{1.22}$$

where $t_{\alpha\beta}$ is a diagonal tensor with the elements $t_{xx} = 1,\ t_{yy} = t_{zz} = 0$, and $S_I(\omega_L)$ is the noise spectrum of the current in the guiding wire. For convenience, we take the shot noise of a

current I_w, $S_{SN} = eI_w \approx 1.6 \times 10^{-19}(I_w/1\mathrm{A})\mathrm{A}^2/\mathrm{Hz}$ as a reference value. Typically, at trap height 10 μm and $S_I(\omega_L)/S_{SN} = 100$, the loss rate has a magnitude of 1 s^{-1} (Folman *et al.*, 2002). Stable current supplies are hence required for atom chips. It may be necessary to reduce current noise even below the shot-noise level, which can be achieved with superconducting wires or permanent magnets (Hinds & Hughes, 1999). We discuss superconducting atom chips in Chap.4.

1.8.2 Trap decoherence

If the fluctuating magnetic field has a nonzero component along the static trapping field, it may shift the Larmor frequency randomly and hence perturb the relative phase in a superposition of two (trapped) spin states. Folman *et al.* (2002); Henkel *et al.* (2003) predicted that the decoherence rate depends on the spectrum of the frequency fluctuations $S_{\Delta\omega}(\omega)$ at the low-frequency limit

$$\Gamma = \frac{S_{\Delta\omega}(\omega \to 0)}{4} \ . \tag{1.23}$$

The shift of the Larmor frequency induced by magnetic field fluctuations at the trap center along the trapping field ($B^{\parallel}_{fl}$) is

$$\Delta\omega_L(t) = -\frac{\langle i|\mu_{\parallel}|i\rangle}{\hbar} B^{\parallel}_{fl}(\mathbf{r}, t) \ , \tag{1.24}$$

where $\mu_{\parallel}$ is the magnetic moment in the direction of the trapping field. The decoherence rate is proportional to the spectrum of the magnetic field fluctuations along the trapping field. Since the thermal magnetic noise in this field component has the same order of the magnitude as in the component perpendicular to the trapping field (Henkel *et al.* (1999), see also in Chap.2), hence the decoherence rate due to magnetic noise is comparable to the loss rate (Eq.(1.21)). Here, we also use that the frequency dependence of surface-induced noise is flat (Henkel *et al.*, 2003). Typically, at the same parameters we discussed for the loss rate, the decoherence rate is of the order of 10 s^{-1} (Folman *et al.*, 2002).

Similarly, the decoherence rate due to current fluctuations in the wire can be computed and it is in the same order of spin flip loss rate due to technical noise (Eq.(1.22)). The impact of the wire current fluctuations on the coherence is somewhat less than that of the thermal magnetic noise. Hence the thermal magnetic noise is a dominant harmful source for decoherence of the trapped atoms as well as for trap loss.

1.8.3 Trap heating

Magnetic field fluctuations also give rise to transitions between the motional states of the trapped atoms, leading to trap heating (Gehm *et al.*, 1998; Turchette *et al.*, 2000). Magnetic noise due to fluctuations of the wire current turns out to give the dominant contribution to the heating rate. Fluctuations of the equilibrium trap position excite transitions to neighboring both higher and lower quantum states, from n to $n\pm1$ (Folman *et al.*, 2002; Fortágh & Zimmermann, 2007).

Heating rate may be investigated with help of harmonic oscillator model (Henkel *et al.*, 1999). For simplicity, we take a one-dimensional harmonic trap potential with angular frequency ω and with a ground-state size $a_0 = (\hbar/2M\omega)^{1/2}$, where M is the mass of the vibrating atom and assume that the atom is initially prepared in the osscillator ground state $|0\rangle$. Fluctuations in the trap position induced by a force F acting on the atom excite the atom from the ground state to the first excited vibrational state, with a rate given by (Gehm *et al.*, 1998; Henkel *et al.*, 1999)

$$\Gamma_{0\to 1} = \frac{a_0^2}{2\hbar^2} S_F(\omega) = \frac{S_F(\omega)}{4\hbar\omega M} \tag{1.25}$$

where $S_F(\omega)$ is the noise spectrum of the force acting on the atom and defined in the same way as $S_B(\omega)$ in Eq.(1.20). Magnetic field fluctuations arising from both thermally excited currents and technical currents lead to this transition.

Technical noise

Heating may result from fluctuations of the driving currents on the atom chip, which randomly shift the location of the trap center. The fluctuations of the trap center Δz are generated by the force $F = M\omega^2\Delta z$ (Folman *et al.*, 2002). From Sec.1.3.2, a fluctuation ΔI_w in the wire current shifts the side guide trap by $\Delta z = \mu_0 \Delta I_w / 2\pi B_b$ where B_b is the (constant) bias field. The force spectrum required for the heating rate Eq.(1.25) is proportional to the current noise spectrum $S_I(\omega)$

$$S_F(\omega) = \left(\frac{\mu_0 M\omega^2}{2\pi B_b}\right)^2 S_I(\omega)\ . \tag{1.26}$$

Again for Rb atoms at a trap frequency of 100 kHz, $S_I(\omega_L)/S_{SN} = 100$ and $B_b = 50$G, the heating rate has a magnitude of 1 s^{-1} (Folman *et al.*, 2002). Comparing with the other sources of noise, the technical noise is probably the dominant source of the heating on the atom chip (Henkel *et al.*, 2003), even for very stable current supply used in experiments. This probably explains the BEC lifetime in the experiment of Reichel (2002).

Thermal fluctuations

Magnetic field fluctuations generated by thermally excited currents in the substrate are equivalent to a force given by the gradient of the Zeeman interaction $F_Z = \nabla(\boldsymbol{\mu}\cdot\mathbf{B})$, and give rise to fluctuations of the trap position, leading to heating. The force spectrum is dependent on the magnetic gradient noise. Considering a planar substrate (half space) and a short distance between the atom and surface $z \ll \delta$, the force spectrum is (Henkel *et al.*, 1999)

$$S_F^{\alpha\beta}(\omega) = \frac{\mu_0^2 k_B T_s}{32\pi\varrho} \frac{\langle \boldsymbol{\mu}^2\rangle + \langle \mu_\parallel^2\rangle}{z^3} \tag{1.27}$$

where $\boldsymbol{\mu}$ is the magnetic moment and $\mu_\parallel$ the component of the magnetic moment parallel to the static trapping field and z distance between the atom and surface. Typically for lithium atoms at a trap frequency of 100 kHz and a height of $z = 10$ μm and Au surface at 300K, the heating rate has the order of 10^{-4} s^{-1} (Folman *et al.*, 2002). It is much smaller than the heating rate due to technical noise.

1.9 Conclusion

Over the last few years, rapid progress has been achieved on trapping and manioulating atoms on atom chips. The atoms can be controlled and manipulated through variation of the magnetic confinement potential provided by current-carrying wires integrated on atom chips. Consequently, atom chips are attractive for various applications, including atom interferometry (Hänsel *et al.*, 2001c; Hinds *et al.*, 2001), realization of BEC (Reichel, 2002) and coherent atom transport (Hänsel *et al.*, 2001). The trap lifetime and coherence of trapped atoms are required to be maintained as long as possible in most applications. In the proximity of atoms close to the chip surface, magnetic field fluctuations introduce additional dacay channels, leading to loss, heating and decoherence (Henkel *et al.*, 1999; Folman *et al.*, 2002; Henkel *et al.*, 2003; Fortágh & Zimmermann, 2007). At a trap height of a few microns, magnetic noise arising from thermally excited currents in metallic conducting wires exceeds all other harmful influences on the atoms (technical noise, residual gas collisions and so on) and imposes dominant limit on the trap lifetime and coherence. Efforts of controlling and reduction of magnetic noise generated by the metallic components on the atom chips have to be made to increase the lifetime and coherence of trapped atoms. This is the main theme and emphasis of this thesis. Chap.2 is devoted to loss (decoherence has a comparable magnitude) induced by thermal magnetic noise which is generated by planar metallic chips. Chap.3 discusses the impact of finite lateral size of the conducting element on the thermal magnetic noise. Superconductors are impromising to significantly reduce the thermal noise and technical noise (Skagerstam *et al.*, 2006; Hohenester *et al.*, 2007). Magnetic traps provided by superconducting chips are investigated in Chap.4.

Chapter 2

Lifetime of magnetically trapped atoms in a layered chip

In this chapter we investigate the lifetime of magnetically trapped atoms above layered structures. For comparison, we first review the main properties of trap lifetimes above a metallic half-space. Magnetic field fluctuations generated by thermal currents in a metallic layered chip are computed numerically and asymptotically identifying scaling laws for the lifetime of trapped atoms. Finally, we introduce the relevant experiments performed by the group of Jörg Schmiedmayer, and compare theory and experiment. The materialof this zharpter is adapted from the paper "Relevance of sub-surface chip layers for the lifetime of magnetically trapped atoms", B. Zhang, C. Henkel, E. Haller, S. Wildermuth, S. Hofferberth,P. Krüger and J. Schmiedmayer.

2.1 Magnetic dipole moment

As we introduced in Sec.1.8.1 that thermal magnetic field fluctuations are main sources of loss and decoherence of trapped atoms above atom chips. Recall Eq.(1.19)

$$\Gamma_{i\to f}(\mathbf{r}) = \sum_{\alpha\beta} \frac{\langle i|\mu_\alpha|f\rangle\langle f|\mu_\beta|i\rangle}{\hbar^2} S_B^{\alpha\beta}(\mathbf{r};-\omega_{fi}) \ . \tag{2.1}$$

The loss rate depends on both the atom dipole moment and the magnetic field noise spectrum. Let us first review some basic formulas of the matrix elements $\langle i|\mu_\alpha|f\rangle$ (Henkel *et al.*, 1999). The total magnetic moment operator of an atom is generally given by

$$\boldsymbol{\mu} = -\mu_B(g_L\mathbf{L} + g_S\mathbf{S} + g_I\frac{m_e}{m_p}\mathbf{I}) \ , \tag{2.2}$$

with μ_B the Bohr magneton, $\mathbf{L}$ the total orbital angular momentum operator, $\mathbf{S}$ the electronic spin operator, $\mathbf{I}$ the nuclear spin operator and g_L, g_S and g_I the corresponding g-factors. Since the proton mass m_p is larger than the electron mass m_e by three orders of magnitude, we can

neglect the contribution of the nuclear magnetic moment. Furthermore, the reasonable restriction to an atom ground state with $L = 0$ simplifies the problem to the calculation of matrix elements of only electronic spin operator. Because the magnetic field fluctuation spectrum $S_B^{\alpha\beta}$ above the planar structure is diagonal as we will see in Sec.2.2, we can focus on the following terms

$$|\langle f|\mu_\alpha|i\rangle|^2 = \mu_B^2 g_S^2 |\langle f|S_\alpha|i\rangle|^2 \ . \tag{2.3}$$

It is convenient to use the raising and lowering operators

$$S_\pm|m_i\rangle = \sqrt{S(S+1) - m_i(m_i \pm 1)}|m_i \pm 1\rangle \ , \tag{2.4}$$

$$S_x = \frac{1}{2}(S_+ + S_-) \ ,$$

$$S_y = \frac{\mathrm{i}}{2}(S_- - S_+) \ , \tag{2.5}$$

to calculate the matrix elements (Sakurai, 1994).

The trapped atom is subjected to a constant offset magnetic field in the center of the trap, assuming it is not moving. Without loss of generality we can assume the magnetic field to be lying within the xz plane, since the diagonal tensor of magnetic field correlation is invariant under rotations of the xy plane (see Fig. 2.1). It is convenient to choose the quantization axis parallel to the magnetic field and denote the basis states by $|m\rangle_\theta$, if the magnetic field forms an angle θ with respect to the z axis. Rewrite the above Eq.(2.3), we get

$$|\langle f|\mu_\alpha|i\rangle|^2 = \mu_B^2 g_S^2 |_\theta\langle f|S_\alpha|i\rangle_\theta|^2 \ . \tag{2.6}$$

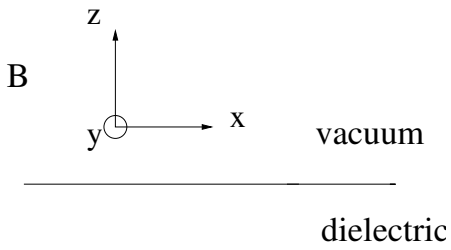

Figure 2.1: Coordinate system. The upper half space is vacuum, the lower part is filled with a dielectric. We choose the z axis perpendicular to the surface and the xy plane parallel to the surface. The magnetic field has symmetry in the xy plane.

By expanding the spin vector components in a rotated coordinate system (denoted by primes) adapted to the trap basis and using raising S'_+ and lowering S'_- operators in the trap

basis, the matrix elements are evaluated as following (Henkel *et al.*, 1999)

$$\begin{aligned}
{}_\theta\langle m_f|S_x|m_i\rangle_\theta &= \left({}_\theta\langle m_f|S'_+|m_i\rangle_\theta + {}_\theta\langle m_f|S'_-|m_i\rangle_\theta\right)\frac{\cos\theta}{2} \\
&\quad + {}_\theta\langle m_f|S'_z|m_i\rangle_\theta \sin\theta \ , \\
{}_\theta\langle m_f|S_y|m_i\rangle_\theta &= \frac{\mathrm{i}}{2}\left({}_\theta\langle m_f|S'_-|m_i\rangle_\theta - {}_\theta\langle m_f|S'_+|m_i\rangle_\theta\right) \ , \\
{}_\theta\langle m_f|S_z|m_i\rangle_\theta &= \left({}_\theta\langle m_f|S'_+|m_i\rangle_\theta + {}_\theta\langle m_f|S'_-|m_i\rangle_\theta\right)\frac{-\sin\theta}{2} \\
&\quad + {}_\theta\langle m_f|S'_z|m_i\rangle_\theta \cos\theta \ ,
\end{aligned} \tag{2.7}$$

where S'_z is the z component of the spin operator. Let us first consider the case of an electronic spin $S = 1/2$, an atom transits from a trapped level $|m_i\rangle_\theta = |-1/2\rangle_\theta$ to an untrapped level $|m_f\rangle_\theta = |1/2\rangle_\theta$. The spin matrix elements Eq.(2.7) are

$$\begin{aligned}
{}_\theta\langle 1/2|S_x|-1/2\rangle_\theta &= \frac{\cos\theta}{2} \ , \\
{}_\theta\langle 1/2|S_y|-1/2\rangle_\theta &= -\frac{\mathrm{i}}{2} \ , \\
{}_\theta\langle 1/2|S_z|-1/2\rangle_\theta &= -\frac{\sin\theta}{2} \ .
\end{aligned} \tag{2.8}$$

If we take into account of the nuclear spin states, we may need the Clebsch-Gordan coefficients $C_{Fm}^{m_s m_I}$, since

$$|Fm\rangle = \sum_{m_S, m_I} C_{Fm}^{m_s m_I} |m_s m_I\rangle \ . \tag{2.9}$$

For example, considering the transition from $|F_i, m_i\rangle = |2,2\rangle$ to $|F_f, m_f\rangle = |2,1\rangle$ and $\theta = \pi/2$, the required the squares of the matrix elements in Eq.(2.1) are $|\langle 2,1|S_x|2,2\rangle|^2 = |\langle 2,1|S_y|2,2\rangle|^2 = 1$ and $|\langle 2,1|S_z|2,2\rangle|^2 = 0$. Together with the magnetic field spectrum we discuss below, we can evaluate the lifetime according to Eq.(2.1).

2.2 Magnetic field correlations

According to the fluctuation-dissipation theorem (Sidles *et al.*, 2003), the spectral density of the magnetic field fluctuations $S_B^{\alpha\beta}(\mathbf{r}, \omega)$ is proportional to the imaginary part of the field's Green function $H_{ij}(\mathbf{r}, \mathbf{r}'; \omega)$

$$S_B^{ij}(\mathbf{r}, \mathbf{r}'; \omega) = \frac{2\hbar}{1 - \mathrm{e}^{-\hbar\omega/k_B T}} \mathrm{Im} H_{ij}(\mathbf{r}, \mathbf{r}'; \omega) \ , \tag{2.10}$$

where T is the temperature of the surface and k_B the Boltzmann constant. In terms of the Bose-Einstein mean occupation number $\overline{n}_{th} = 1/(\mathrm{e}^{\hbar\omega/k_B T} - 1)$ and for $\omega > 0$, the above equation can be rewritten as (Henkel *et al.*, 1999),

$$\begin{aligned}
S_B^{ij}(\mathbf{r}, \mathbf{r}'; \omega) &= 2\hbar(\overline{n} + 1)\mathrm{Im} H_{ij}(\mathbf{r}, \mathbf{r}'; \omega) \ , \\
S_B^{ij}(\mathbf{r}, \mathbf{r}'; -\omega) &= 2\hbar\overline{n}\mathrm{Im} H_{ij}(\mathbf{r}, \mathbf{r}'; -\omega) \ .
\end{aligned} \tag{2.11}$$

As an example, let us consider the ratio of transition rates for the spin flips $|i\rangle \rightarrow |f\rangle$ and $|f\rangle \rightarrow |i\rangle$. It is given by

$$\frac{\overline{n}}{\overline{n}+1} = \mathrm{e}^{-\frac{\hbar\omega}{k_B T}} \tag{2.12}$$

in agreement with the principle of detailed balance. At zero temperature, $\overline{n} = 0$, and the second line in Eq.(2.11) vanishes. The relaxation dynamics is then entirely due to spontaneous decay[1], induced by the vacuum fluctuations of the magnetic field. At high temperature, $\overline{n} \gg 1$, the fluctuation spectrum becomes independent on the sign of ω. Therefore, decay and excitation rates are then nearly the same.

Recall that the Green function describes the magnetic field radiated by a point magnetic moment. This field is the sum of the magnetic field in free space plus the field reflected from the surface. The free space field leads to a term $H_{ij}^{vac}(\mathbf{r}, \mathbf{r}'; \omega)$ in the Green function that is actually independent of the trap position $\mathbf{r}$ and gives the spectral density of the blackbody field (the Planck law):

$$S_B^{(vac)ij}(\boldsymbol{r}; \omega) = S_B^{(vac)}(\omega)\delta_{ij} \ , \tag{2.13}$$

$$S_B^{(vac)} = \frac{\hbar\mu_0\omega^3}{3\pi c^3(1 - e^{-\hbar\omega/k_B T})} \ . \tag{2.14}$$

To calculate the field reflected from the surface, we expand the free-space magnetic field in plane waves and apply the reflection coefficients $r_{s,p}(u)$ for each wave incident on the surface. Here, s and p label the two transverse field polarizations and u is the sine of the angle of incidence. The corresponding spectral density depends only on the distance z to the surface and may be written in terms of a dimensionless tensor $h_{ij}(kz)$ (Agarwal, 1975)

$$S_B^{(ref)ij}(\mathbf{r}, \omega) = S_B^{(vac)}(\omega)h_{ij}(kz) \ , \tag{2.15}$$

where $k \equiv \omega/c$. h_{ij} is diagonal with elements $h_{xx} = h_{yy} = h_{\parallel}$ and $h_{zz} = h_{\perp}$ given by (Henkel *et al.*, 1999)

$$h_{\parallel}(kz) = \frac{3}{4}\mathrm{Re}\int_0^{+\infty} \frac{u\mathrm{d}u}{\sqrt{1-u^2}} e^{2ikz\sqrt{1-u^2}}(r_p(u) + (u^2-1)r_s(u)) \ , \tag{2.16}$$

$$h_{\perp}(kz) = \frac{3}{2}\mathrm{Re}\int_0^{+\infty} \frac{u^3\mathrm{d}u}{\sqrt{1-u^2}} e^{2ikz\sqrt{1-u^2}} r_s(u) \ . \tag{2.17}$$

The range $u > 1$ corresponds to the evanescent part of the angular spectrum a magnetic dipole generates in free space. The square roots occurring in Eqs.(2.16) and (2.17) are chosen with positive imaginary part.

[1] the only process that survives in Eq.(2.1), if $-\omega_{fi} > 0$

2.2.1 Half space

For a half-space structure, the reflection coefficients in Eq.(2.16 and 2.17) are given by the Fresnel formulas at the surface,

$$r_s(u) = \frac{\sqrt{1-u^2}-\sqrt{\varepsilon-u^2}}{\sqrt{1-u^2}+\sqrt{\varepsilon-u^2}}\,, \tag{2.18}$$

$$r_p(u) = \frac{\varepsilon\sqrt{1-u^2}-\sqrt{\varepsilon-u^2}}{\varepsilon\sqrt{1-u^2}+\sqrt{\varepsilon-u^2}}\,, \tag{2.19}$$

where ε is the relative dielectric function of the material. It is often described by the Drude model. In our case, the dielectric function is dominated by the zero-frequency pole, we use the approximation

$$\varepsilon = \frac{\mathrm{i}}{\varepsilon_0 \varrho \omega} = \frac{2\mathrm{i}}{k^2\delta^2}\,, \tag{2.20}$$

where ε_0 the permittivity in vacuum, ϱ is the metallic resistance. For metals with good conductivity (small resistance), the second term in Eq.(2.20) is much larger than 1, so that we only take the first term in the following calculations. The skin depth δ is the chraracteristic length scale on which an electromagnetic wave entering a metal is damped. It is given by (for $\omega > 0$) (Jackson, 1975)

$$\delta = \frac{1}{k}\sqrt{2\varepsilon_0\varrho\omega}\,. \tag{2.21}$$

We will see that the skin depth is an important parameter in scaling laws for spin flip transitions above planar structures.

For typical trap frequencies the corresponding electromagnetic wavelength is much larger than z, so we can restrict our calculations to the quasi-static limit $z \ll \lambda$ and find analytical expressions for the tensor elements Eqs.(2.16) and (2.17). The inspection of Eqs.(2.16) and (2.17) shows that the exponential $\mathrm{e}^{2\mathrm{i}kz\sqrt{1-u^2}} \approx \mathrm{e}^{-2kzu}$ provides a cutoff only for very large value $u \gg 1/(kz) \gg 1$. On the other hand, the other factors in the integrands increase as powers of u. The value of the integral is thus dominated by values $u \sim u_{max}$ around the maximum $u_{max} \sim 1/(kz)$. It is therefore accurate to use asymptotic expansions of the Fresnel coefficients for large $u \gg 1$. According to Eqs.(2.18) and (2.19). The asymptotic form of the coefficients depends on whether u_{max}^2 is much smaller or larger than the magnitude $|\varepsilon|$ of the dielectric constant. According to the relation Eq.(2.20) between ε and δ, these two regimes correspond to whether z is larger or smaller than δ.

The limit $1 \ll |\varepsilon|^{1/2} \ll u$ corresponds to a distance small compared to the skin depth, $z \ll \delta \ll \lambda$. In this regime, we get the following asymptotic expressions for the Fresnel coefficients (2.18 and 2.19)

$$\begin{aligned} r_s(u) &\to \frac{\varepsilon-1}{4u^2}\,, \\ r_p(u) &\to \frac{\varepsilon-1}{\varepsilon+1}\,. \end{aligned} \tag{2.22}$$

Insert Eq.(2.22) into the integrals Eq.(2.16), and notice that $r_p(u) \approx 1,\ (u^2-1)r_s(u) = (\varepsilon-1)/4 \gg 1$, so the contribution of $r_p(u)$ is negligible. Then the integrals Eqs.(2.16) and

(2.17) for the tensor elements are evaluated to

$$\begin{aligned} h_{\parallel}(kz) &\approx \frac{3}{32kz}\mathrm{Im}\frac{(\varepsilon-1)}{4} = \frac{3}{16k^3\delta^2 z}\ , \\ h_{\perp}(kz) &\approx = 2h_{\parallel}(kz)\ . \end{aligned} \tag{2.23}$$

In the opposite limit of a small skin depth $\delta \ll z \ll \lambda$, the Fresnel coefficients should be expanded in the regime $1 \ll u \ll |\varepsilon|^{1/2}$

$$\begin{aligned} r_s(u) &\rightarrow -1 + \frac{2\mathrm{i}u}{\sqrt{\varepsilon}}\ , \\ r_p(u) &\rightarrow 1 + \frac{2\mathrm{i}}{u\sqrt{\varepsilon}}\ . \end{aligned} \tag{2.24}$$

This corresponds to nearly perfect conductors. In this region, $\mathrm{Im}\, r_s(u)$ is also much larger than $\mathrm{Im}\, r_p(u)$ by a factor u^2, $r_p(u)$ is then again negligible in Eq.(2.16). So the integrals Eqs.(2.16) and (2.17) for the tensor elements are evaluated to

$$\begin{aligned} h_{\parallel}(kz) &\approx \frac{9}{16(kz)^4}\mathrm{Im}\frac{1}{\sqrt{\varepsilon}} = \frac{9\delta}{32k^3z^4}\ , \\ h_{\perp}(kz) &\approx 2h_{\parallel}(kz)\ . \end{aligned} \tag{2.25}$$

To summarize, in both regions we have $\mathrm{Im}\ r_s(u) \gg \mathrm{Im}\ r_p(u)$, and Eq.(2.16) can be simplified by cancelling $r_p(u)$. The integrals Eqs.(2.16) and (2.17) are therefore only dependent on $r_s(u)$, and the perpendicular element $h_{\perp}$ is double of the parallel element $h_{\parallel}$. With Eqs.(2.23) and (2.25), we can compute the magnetic field spectrum Eq.(2.15) and the loss rate which is simplified to

$$\Gamma_{-\frac{1}{2}\rightarrow\frac{1}{2}} = \frac{\mu_B^2 g_S^2 \sin\theta^2}{4\hbar^2} h_{\parallel} S_B^{(vac)}\ . \tag{2.26}$$

Eqs.(2.23) and (2.25) also show that the skin depth determines the spectral distribution of the elctromagnetic near field above bulk substrates.

2.2.2 Layered chip

For a layered chip, r_λ ($\lambda = s, p$) are the effective reflection amplitudes from the multilayer structure, as illustrated in Fig. 2.2. At the lowest interface, the Fresnel reflection coefficients apply and are given by

$$r'_{s,n} = \frac{\sqrt{\varepsilon_n - u^2} - \sqrt{\varepsilon_{n+1} - u^2}}{\sqrt{\varepsilon_n - u^2} + \sqrt{\varepsilon_{n+1} - u^2}} \tag{2.27}$$

$$r'_{p,n} = \frac{\varepsilon_{n+1}\sqrt{\varepsilon_n - u^2} - \varepsilon_n\sqrt{\varepsilon_{n+1} - u^2}}{\varepsilon_{n+1}\sqrt{\varepsilon_n - u^2} + \varepsilon_n\sqrt{\varepsilon_{n+1} - u^2}} \tag{2.28}$$

where ε_n is the permittivity of the nth layer. The effective reflection coefficient of the nth layer is (Yeh, 1988)

$$r_{\lambda,n} = \frac{r'_{\lambda,n} + r_{\lambda,n+1}e^{i\tau_{n+1}}}{1 + r'_{\lambda,n}r_{\lambda,n+1}e^{i\tau_{n+1}}} \tag{2.29}$$

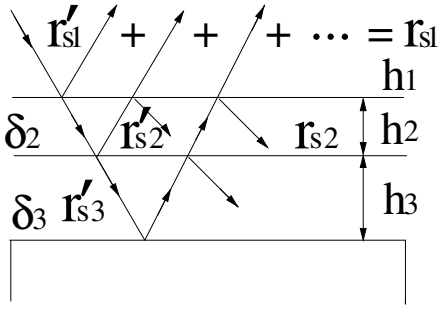

Figure 2.2: A chip with two layers on top of a semi-infinite substrate. h_n is the thickness of the n'th layer, δ_n denotes the optical path length for a single down and up ray in the n'th layer. $r'_{\lambda n}$ are the Fresnel reflection coefficients at the interface between the layers no. n and $n+1$ ($\lambda = s, p$), while $r_{\lambda n}$ are the effective (multilayer) reflection coefficients from the nth layer.

where $r'_{\lambda,n}$ is the Fresnel coefficient Eq.(2.28 or 2.27) and $r_{\lambda,n+1}$ the amplitude for the layered structure below; τ_n is the complex phase shift in the layer:

$$\tau_n = 2h_n k\sqrt{\varepsilon_n - u^2}\ , \tag{2.30}$$

h_n is the layer thickness and the square root is chosen with positive imaginary part. In the case of Fig. 2.2, the lowest layer is $n = 3$ and we put $r_{\lambda,3} \equiv r'_{\lambda,3}$. We then apply Eq.(2.29) recursively for the next layers, until the reflection from the topmost layer, $r_{\lambda,1} = r_{\lambda,1}(u)$, is found. This is the coefficient we need in Eqs.(2.16) and (2.17). The integral over u is computed numerically. The singularity $1/\sqrt{1-u^2}$ at the point $u = 1$ can be removed with change of variable

$$v = \begin{cases} \sqrt{1-u^2} & 0 < u < 1 \\ \mathrm{i}\sqrt{u^2-1} & u > 1\ . \end{cases} \tag{2.31}$$

2.3 Discussion of trap lifetime

2.3.1 Impact of subsurface layers

We discuss here the relevance of the subsurface layers on the lifetime.

We plot in Fig. 2.3 the trap lifetime above a gold layer deposited on a substrate with varying resistivity ϱ_3 normalized to a gold layer suspended in vacuum ($\varrho_3 = \infty$). The subsurface layer hardly has an impact on the trap lifetime, as long as the topmost layer has a resistance that is smaller by at least two orders of magnitude. We now give an analytical argument to understand this more clearly. As mentioned in Sec.2.2.1, it is reasonable to use the asymptotic expansion of the reflection coefficients Eqs.(2.27) $\sim$ (2.29) for large $u \gg 1$. Let us focus on a distance comparable to the skin depth in the gold layer (subscript 2) at the transition frequency, and a sub-surface layer with a much smaller conductivity. We check that the integrands in Eqs.(2.23) and (2.25) peak around $u^2_{max} \sim |\varepsilon_2| \gg |\varepsilon_3| \gg 1$. If we consider the first order expansion in

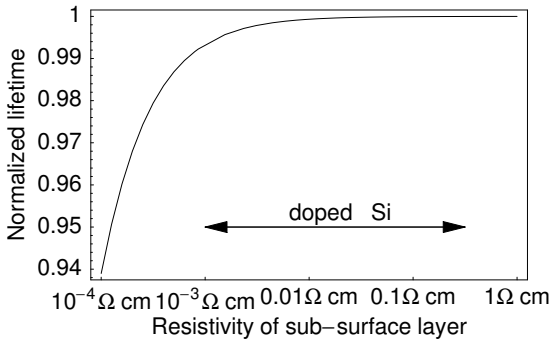

Figure 2.3: Trap lifetime vs. resistivity of sub-surface layer, normalized to a single layer suspended in vacuum (gold, $3.1\,\mu$m thick, resistivity $2.2\,\mu\Omega$cm). The distance from the trapped atom to the surface is $10\,\mu$m. The layer permittivities are $\varepsilon_0\varepsilon_n = i/(\omega\varrho_n)$ and $\omega/2\pi = 1.1\,$MHz.

this regime, we get

$$r_{s,1} = \frac{(1-\Delta_s^2)(1-e^{i\tau_2})}{(1-\Delta_s)^2-(1+\Delta_s)^2 e^{i\tau_2}}\,, \tag{2.32}$$

with

$$\Delta_s = i\sqrt{\varepsilon_2 - u^2}/u\,. \tag{2.33}$$

And

$$r_{p,1} = -1 + \Delta_p \frac{1+e^{i\tau_2}}{1-e^{i\tau_2}}\,, \tag{2.34}$$

where

$$\Delta_p = 2i\sqrt{\varepsilon_2 - u^2}/(\varepsilon_2 u)\,. \tag{2.35}$$

Note that $|\Delta_p| \ll 1$ around u_{max}, while $|\Delta_s| \sim 1$. From the equations above, we see that ε_3 has cancelled from the multilayer coefficients. This means that the sub-surface layer has no effect on the trap lifetime as long as its resistance is larger than the topmost (metallic) layer and the trap is at a distance comparable to the skin depth in the metal or smaller. This result is important for us to get further simplified expression of reflection coefficients, and then the trap lifetime: we can assume that there is a single metallic layer in vacuum when the sub-surface resistance is larger than the topmost (metallic) layer.

In Fig. 2.4, we plot the lifetime (normalized to the lifetime above a gold half-space) for varying thickness of the topmost layer. The black solid line is the asymptotic result obtained by inserting Eqs.(2.32) and (2.34) into the integrals for the Green functions. The triangles and squares mark calculations for a gold/silicon and gold/vacuum structure, using the full multilayer reflection coefficients Eq.(2.29). We see that the three situations give the same trap lifetime. For these chip parameters, reducing the gold layer thickness thus improves the trapping conditions. This happens because the layer being much thinner than the skin depth at the relevant frequency ($\delta \equiv (2\varrho/(\mu_0\omega))^{1/2}$), it is a thermal radiation source across its whole thickness. The dashed (red) curve in the figure gives the result of the quasi-static approximation

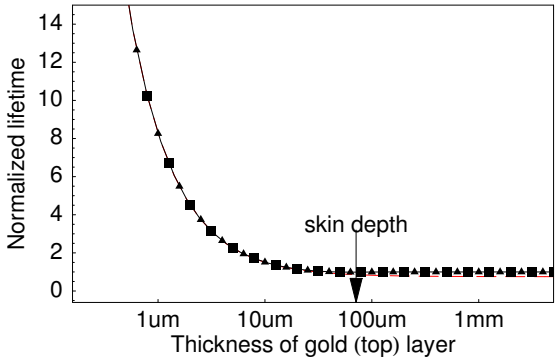

Figure 2.4: Trap lifetime vs. thickness t of the top layer (gold), normalized to a gold half-space; distance of trapped atoms to the surface: $z = 10\,\mu\mathrm{m}$. Triangles: gold/silicon structure; boxes: gold layer in vacuum. For these two, the full multilayer reflection coefficients are used. Black solid line: based on the asymptotic expansion Eqs.(2.32) and (2.34) of the reflection coefficients in the magnetic Green tensor. Dashed (red) line: prediction $(t + z)/t$ of the quasistatic theory, valid when z is much smaller than the skin depth. The arrow marks the skin depth in gold at the transition frequency $1.1\,\mathrm{MHz}$. The layer resistivities are given in Fig. 2.3.

introduced in (Henkel & Pötting, 2001); it is valid for a trap distance $z \ll \delta$ and gives a good approximation for the chosen parameters.

2.3.2 Asymptotic expansion

Based on Sec.2.3.1, we can simplify the layered chip into a single layer suspended in vacuum as long as the layers below have a much smaller conductivity. Then Eq.(2.29) is simplified to

$$r_\lambda = r'_\lambda \frac{1 - \mathrm{e}^{\mathrm{i}k_0 h\sqrt{\varepsilon - u^2}}}{1 - r'^2_\lambda \mathrm{e}^{\mathrm{i}k_0 h\sqrt{\varepsilon - u^2}}}\,, \tag{2.36}$$

where ε is the permittivity of the metal, h is the thickness of metallic layer, λ denotes the polarizations s and p, r'_λ is Fresnel coefficient. As we discussed in Sec.2.2.1, for a bulk substrate the magnetic filed spectrum is only dependent on $r_s(u)$. We assume that this is still true for layered structures and only focus on the reflection coefficeint of s polarization and the parallel component of magnetic noise spectrum $h_\parallel$. Insert the asymptotics of Fresnel coefficients Eqs.(2.22) and (2.24) into Eq.(2.36) respectively, we get the asymptotics for reflection coefficient r_s in different regimes as listed in Table 2.1. In fact when the thickness h becomes comparable to the skin depth δ, the reflection coefficients above layer structure have the same expressions as those above half space.

The parallel component of the magnetic noise spectrum $h_\parallel$ is computed based on the asymptotics in Table 2.1 and listed in Table 2.2. Recall that the perpendicular component of the magnetic noise spectrum is the double of the parallel one $h_\perp = 2h_\parallel$. We plot the lifetime $1/\Gamma$ of trapped atoms (based on Eq.(2.26)) above the metallic layer in Fig. 2.5. The trap

layer	$k_0 u \ll 1/\delta$	$h/\delta^2 \ll k_0 u \ll 1/h$	$1/h \ll k_0 u$
$\mathrm{Im}\, r_s(u)$	$\mathrm{Im}\, \dfrac{-1+(1+\mathrm{i})k_0 u\delta}{1+\mathrm{i}k_0\delta^2/h}$	$\dfrac{h}{k_0 u \delta^2}$	$\dfrac{1}{2k_0^2 u^2 \delta^2}$

Table 2.1: Asymptotic approximations to the reflection coefficients from a layer. The limit $k_0 u \gg \omega/c$ is taken throughout.

	$z \ll \delta$	$\delta \ll z$	
half space $h_\parallel$	$\dfrac{3}{16k_0^3\delta^2 z}$	$\dfrac{9\delta}{32k_0^3 z^4}$	
	$z \ll h \ll \delta$	$h \ll z \ll \delta^2/h$	$\delta^2/h \ll z$
layer $h_\parallel$	$\dfrac{3}{16k_0^3\delta^2 z}$	$\dfrac{3h}{16k_0^3\delta^2 z^2}$	$\dfrac{9\delta^2}{32k_0^3 h z^4}$

Table 2.2: Approximations for the parallel component of the magnetic noise spectrum $h_\parallel$ above a half space and a metallic layer. The perpendicular component can be obtained by $h_\perp = 2h_\parallel$.

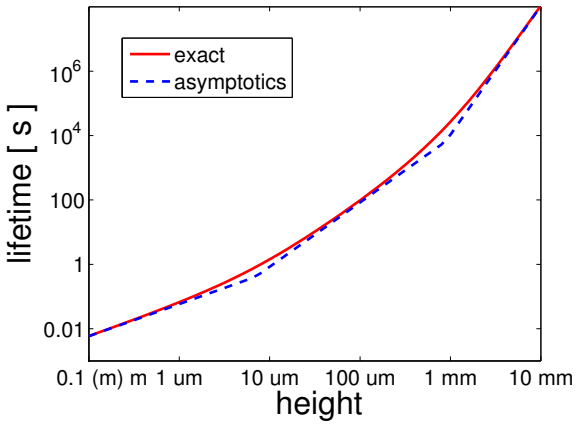

Figure 2.5: Lifetime vs. trap height above a thin layer. Solid line: numerical results based on Eqs.(2.27) and (2.30). Dashed lines: asymptotic approximations based on Table 2.2. The layer is 7μm thick, and the skin depth is 70μm. The atom transits from $|F_i, m_i\rangle = |2, 2\rangle$ to $|F_f, m_f\rangle = |2, 1\rangle$, the transition (Larmor) frequency being $\omega_{fi}/2\pi = 1.1$ MHz.

lifetime decreases as the thin layer is approached, but has different power laws in the different regions. When the trap height is smaller than the thickness of the layer, the bulk and the thin layer behave the same (see the first colume in Table 2.2. In the region $h \ll z \ll 3\delta^2/2h$, the spin flip rate is proportional to the volume of metallic layer, hence to the layer thickness (Henkel *et al.*, 1999; Folman *et al.*, 2002). The power law is reversed for $z \gg 3\delta^2/2h$, in this region the lifetime is proportinal to the layer thickness and the lifetime above a thick layer is longer than that above a thinner one (Scheel *et al.*, 2005). This can also be also seen in Fig. 2.6.

2.3.3 Dependence on skin depth

Fig.2.6 illustrates how the lifetime depends on the skin depth of the material, The atom is trapped at $60\mu\mathrm{m}$ away from the surface, and the spin loss is due to the transition $|F_i, m_i\rangle = |2, 2\rangle$ to $|F_f, m_f\rangle = |2, 1\rangle$. The solid curve corresponds to the bulk substrate (half space), the dashed lines and circles both correspond to a $1\mu\mathrm{m}$ thick layer. The dashed lines show the lifetime in the different regions as listed in Table 2.2. The circles are computed numerically. The approximations are in a good agreement with the exact results, they only slightly underestimate the lifetime in the transition region. When the skin depth is less than the thickness $1\mu\mathrm{m}$, the bulk metal and the thin layer produce almost the same noise, because the source of the noise mainly lies within one skin depth of the metal. In this region, the lifetime scales as $1/\delta$. Increasing the skin depth but keeping it less than $\sqrt{hz}$ for the thin layer and less than z for the bulk metal, the lifetime above the bulk metal still scales as $1/\delta$, whereas the lifetime above the thin layer is proportinal to h/δ^2, shorter than above bulk maetal. Similar result is observed by Varpula & Poutanen (1984); Scheel *et al.* (2005). The asymptotic formula for the region $\delta \ll \sqrt{hz}$ (the third colume in Table 2.2), has not be given before, to our knowledge. In the region $\sqrt{hz} \ll \delta$ for the thin layer and $z \ll \delta$ for the bulk metal, both lifetimes inrease as δ^2. The thin layer gives a longer lifetime than the bulk metal by a factor of z/h. The minimal lifetime is obtained at $\delta \simeq \sqrt{hz}$ above a thin layer or $\delta = z$ above a bulk metal. When an atom is trapped above a thin layer, we should avoid the atom-surface distance $z = \delta^2/h$. For a bulk metal, we should avoid the atom-surface distance $z = \delta$. The atom suffer the strongest noise in these two cases.

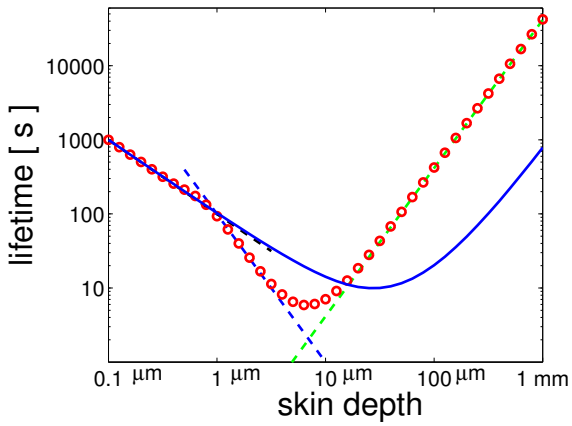

Figure 2.6: Lifetime vs. skin depth. The atom-surface distance is $60\mu\mathrm{m}$. Solid line: bulk substrate (half space). Dashed lines and circles: $1\mu\mathrm{m}$ thick layer. The dashed lines show the approximations in Table 2.2, the circles are computed numerically.

2.4 Experiment

Over the last three years, the reduction of lifetimes in traps close to conducting surfaces has been investigated in a number of experiments. Both the influence of technical noise (Leanhardt *et al.*, 2003) and thermal noise near bulk conductors of different materials (Harber *et al.*, 2003; Fortágh *et al.*, 2002; Jones *et al.*, 2003) have been found to be in quantitative agreement with the theory presented above. Layered structures, which promise to reduce loss rates due to thermal currents, have been explored in one experiment by the Vuletic group (Lin *et al.*, 2004) which investigated the loss above a $2\mu\mathrm{m}$ thick and $10\mu\mathrm{m}$ wide Cu wire and a Si substrate. Here we introduce an experiment done by Schmiedmayer group, which allows to investigate the loss due to spin flips over a thin metal layer in a configuration where the contributions of technical noise can be kept constant and the thermal noise sources can be studied over a wide range of distances near a multilayer structure.

2.4.1 Experimental setup

The experiments were performed with the standard atom chip setup in Heidelberg and described by Krüger (2004); Wildermuth *et al.* (2004). One starts with more than 10^8 ^{87}Rb atoms accumulated in a mirror magneto-optical trap (MOT) a few mm from the chip surface. The atoms are subsequently transferred to a purely magnetic Z-wire trap and cooled to $\sim 10\mu$K by radio frequency (RF) evaporation. Both the MOT and the magnetic trap are based on copper wire structures mounted directly underneath the chip. The resulting sample of $> 10^6$ atoms is then loaded to the selected chip trap, where a second stage of RF evaporative cooling creates either a BEC or thermal cloud just above the condensation temperature.

2.4.2 Atom chip setup

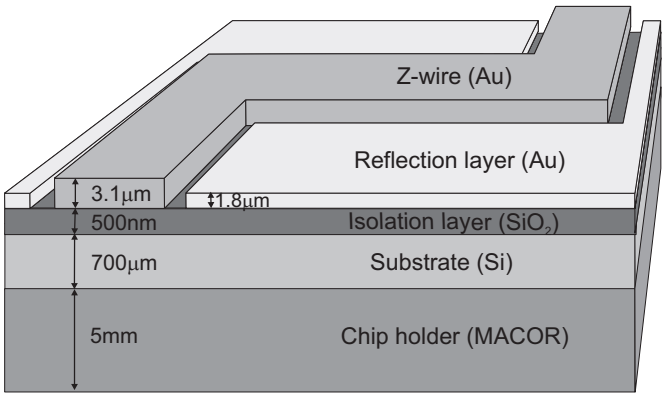

Figure 2.7: Layer structure of the chip. The resistivities of the layers are $\varrho > 10^6\Omega$cm (MACOR), $\varrho = 1.7\mu\Omega$cm (copper), $\varrho = 17\mathrm{m}\Omega$cm (doped silicon), $\varrho > 10^4\Omega$cm (SiO_2) and $\varrho = 2.2\mu\Omega$cm (gold). From Zhang *et al.* (2005)

The atom chip incorporates various different layers (see Fig. 2.7). The chip itself was fabricated using our standard method described by Groth *et al.* (2004). It is grown on a 700 μm thick silicon substrate covered with an insulation layer of SiO_2 (500nm) and a Ti adhesion layer (35nm). The gold layers with the desired wire patterns are created using a nano-lithographic lift-off technique adapted for thick ($> 1\,\mu$m) layers. The major area in this chip is covered with a 1.8 μm thick reflection layer containing gaps (width 10 μm) to isolate the current carrying wires. The thicker Z-wire structures were fabricated with a two layer technique allowing a thickness of 3.1 μm (wire cross section $3.1 \times 100\,\mu$m^2). The atom chip structure is placed on top of a 5mm thick ceramics chip holder (MACOR).

2.4.3 Lifetime measurements

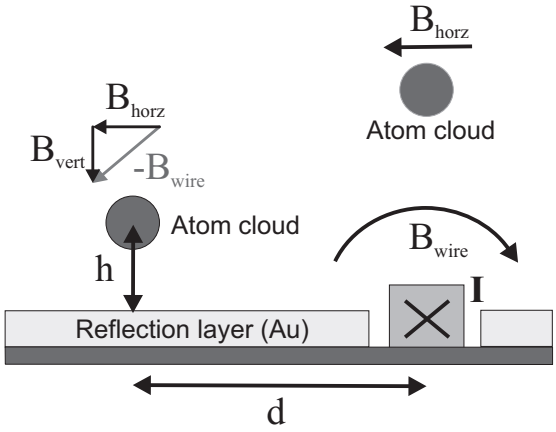

Figure 2.8: Lateral trap displacement. An external horizontal magnetic field $\mathbf{B}_{horz}$ cancels the circular magnetic field $\mathbf{B}_{wire}$ of a current carrying wire directly over the wire. By applying an additional vertical field $\mathbf{B}_{vert}$ perpendicular to the chip surface, the trap can be positioned at a distance d from the wire and a height z above the chip surface. From Zhang *et al.* (2005)

The lifetimes of trapped ultra cold ^{87}Rb atoms were measured in a Ioffe-Pritchard type microtrap generated by currents flowing through the Z-shaped wire. The measurements are done with $\sim 1 \cdot 10^5$ thermal atoms at $\sim 1\,\mu$K in a trap created with a current of 2 A and a Larmor frequency of $\omega_{fi}/2\pi = 1.1$ MHz at the trap minimum (corresponding to a field of 1.5 G).

The microtraps on the chip are created in the side guide configuration described in Sec.1.3.2. In the standard configuration the trap center lies directly above the center of the Z wire (see Fig. 2.8). By adding a vertical magnetic field component $\mathbf{B}_{vert}$, the trap minimum is rotated around the central wire of 'Z'. By adjusting the strength and orientation of the bias field the trap minimum can be positioned at a given distance d from the current carrying wire and at a given height z above the 1.8 μm thick gold layer of the chip (Fig. 2.8).

Placing the trap a significant distance away from the Z-wire permits us to keep the trap parameters nearly constant for each height above the surface. The further away one moves,

the easier it is to keep the traps equal, independent of the height for the same wire current. But the traps get shallower at larger distance from the trapping wire. A shallow trap cannot be brought close to the surface for the lifetime measurements, because the trap depth is reduced due to the atom-surface interaction potential. Atoms are thus lost not only by spin flip but also by evaporation across the potential barrier towards the chip surface. This leads to a significant cooling of the sample: in a dense cloud, evaporation leads typically to a final temperature of about 1/10th of the trap depth.

For each lifetime measurement the trapped atoms are imaged either in situ or after a time-of-flight expansion. The former allows measurements down to lower atom number, the latter allows us to determine both the number of atoms and the temperature of the atoms. Both measurements of atom number agree, and both are used to determine the lifetime of the trapped clouds.

The independent measurement of the temperature is crucial because it permits to see if There are additional losses due to surface induced evaporation. A decrease in temperature is a direct indication that in addition to spin flips, atoms cross the lowered potential barrier towards the surface. It is observed that the decay of the atom number is then generally non-exponential. The height at which this becomes important varies from $z = 3\,\mu$m for moderately confining traps directly over the wire up to $z = 40\,\mu$m for very shallow traps at a lateral distance $d = 520\,\mu$m from the trapping wire.

In the following comparison between calculation and experiment we only consider data where the temperature stays constant so that the main loss mechanicms are surface-induced spin flips and background collisions.

2.4.4 Comparison theory–experiment

To investigate the influence of the thermal noise we choose a distance $d = 280\,\mu$m as a compromise between being dominated by technical noise for small d and losing atoms due to evaporation towards the surface at large d.

In order to make a comparison between theory and experiment, we plot in Fig. 2.9 both experimental data (symbols) and numerical calculations (lines). A fair agreement is found down to distances of a few microns when the theory takes into account (i) the finite thickness of the topmost (gold) layer and (ii) a distance-independent loss rate (red line). We stress that the latter rate is taken from the experimental data (saturation at large distance) so that the theory has no adjustable parameters. The figure shows that the lifetime above a thin (few μm thick) gold layer is significantly enhanced compared to a gold half space. We have checked that adding a MACOR or copper substrate below the thick silicon wafer does not change the results of the calculation. We attribute the discrepancy between experiment and theory to atom-surface potentials that lower the potential barrier towards the surface, as also suggested by the Vuletic group (Lin *et al.*, 2004). As mentioned above, this mechanism becomes more important at short distance (below a few micron).

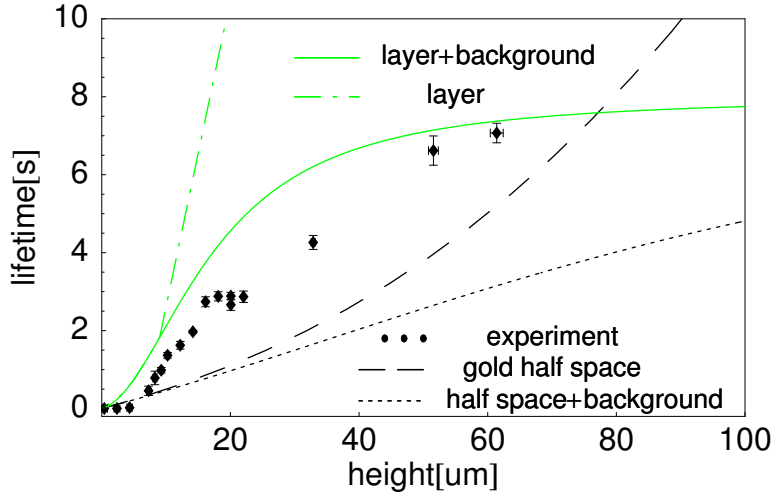

Figure 2.9: Experimental data and theoretical predictions for the trap lifetime in a miniaturized magnetic Ioffe-Pritchard type trap. Symbols: Life time data for a trap laterally displaced by $280\,\mu$m with respect to the current-carrying wire structure. Below $10\,\mu$m distance, surface evaporation decreases the lifetime. Lines: theoretical predictions with different level of detail for loss processes (spin flips) induced by thermal surface noise. The atom transits from $|F_i, m_i\rangle = |2, 2\rangle$ to $|F_f, m_f\rangle = |2, 1\rangle$, the transition (Larmor) frequency being $\omega_{fi}/2\pi = 1.1\,$MHz. Black lines: bulk substrate (gold half-space). Green lines: layered chip (thin gold layer, doped silicon substrate, see parameters in Fig. 2.7). The thin SiO_2 isolation layer is neglected. Solid and dashed lines: calculation including trap lifetime at large distance.

2.5 Conclusion

We have studied the lifetime of magnetically trapped atoms above a layered atom chip. Numerical calculations have been performed for the loss rate due to spin flips induced by thermal magnetic near fields, taking into account multiple reflections in the layers. The magnetic noise depends essentially on the thickness of the topmost metallic layer, as long as the the layers below have a much smaller conductivity. The same magnetic noise would be obtained with a metallic membrane suspended in vacuum. A thin layer helps to increase the trap lifetime if its thickness is substantially thinner than the skin depth at the Larmor frequency, inversely it gives a shorter lifetime than a bulk metal when its thickness is comparable to the skin depth. Our results are in a good agreement with the experiment performed by Schmiedmayer group. Trap loss at a large lateral distance from the wire is dominated by thermally induced spin flips. At shorter distance, atom-surface potentials of the van der Waals-Casimir-Polder type lower the trap barrier and open additional loss channels.

Chapter 3

Magnetic noise around 2D metallic microstructures

We investigated lifetimes of trapped atoms above infinite planar structures in three spatial dimensions in the former chapters. However actual experiments often use metallic wires of finite lateral size, for example, in atom chips where a continuous metallic layer is etched to define wires that can be addressed with different currents. Considering the finite lateral size, we restrict to two spatial dimensions(2D) geometries to simplify the calculations. And because it is not convenient to interpolate atom trap lifetimes in 2D directly, we focus on the local spectrum of the magnetic field near a 2D metallic microstructure at finite temperature. This is a first step towards an accurate estimate of lifetimes of trapped atoms near 3D structures with finit lateral size. In order to see the impact of finitely lateral size on the magnetic field, we derive the magnetic field above infinite planar wires and study its properties first, then investigate the magnetic field around arbitrary geometries with boundary integral equations and with an approximation based on incoherent summation of local current elements. We compare the infinite planar wire with a rectangular wire to find the impact of finite lateral size. The magnetic field around multiwires are discussed. This chapter is based on paper Zhang & Henkel (2007).

3.1 Magnetic dipole radiation

Recall the fluctuation-disspation theorem, the fluctuations of the thermal magnetic field $\mathcal{B}(\mathbf{r};\omega)$ can be given by

$$\mathcal{B}_{ij}(\mathbf{r};\omega) = \frac{2\hbar}{\mathrm{e}^{\hbar\omega/k_BT}-1}\mathrm{Im}\, B_{ij}(\mathbf{r},\mathbf{r}';\omega)\ , \tag{3.1}$$

where the temperature-dependent prefactor is the Bose-Einstein occupation number, and the Green function $G(\mathbf{r},\mathbf{r}';\omega)$ gives the magnetic field generated at $\mathbf{r}$ by a point magnetic dipole located at $\mathbf{r}'$ and oscillating at the frequency ω, $B_i(\mathbf{r},t) = \mathcal{G}_{ij}(\mathbf{r},\mathbf{r}';\omega)\mu_j\,\mathrm{e}^{-\mathrm{i}\omega t} + \mathrm{c.c.}$. We are thus led to solve the following electrodynamic problem: find the complex magnetic field amplitude $\mathbf{B}(\mathbf{r};\omega|\boldsymbol{\mu})$ created by a monochromatic point dipole $\boldsymbol{\mu}(t) = \boldsymbol{\mu}\,\mathrm{e}^{-\mathrm{i}\omega t} + \mathrm{c.c.}$ located

at position $\mathbf{r}'$. We then compute

$$B_{ij}(\mathbf{r},\mathbf{r}';\omega) = \frac{\partial B_i(\mathbf{r};\omega|\boldsymbol{\mu})}{\partial \mu_j} \tag{3.2}$$

In the limit $\mathbf{r} \to \mathbf{r}'$ this field becomes the singular 'self field' and requires a cutoff in wavevector space. Its imaginary part is cutoff-independent, however, and given by $\operatorname{Im}\mathbf{B}(\mathbf{r}';\omega) = \mu_0\omega^2\boldsymbol{\mu}/(8c^2)$ in two-dimensional free space ($\mu_0\omega^3\boldsymbol{\mu}/(6\pi c^3)$ in 3D).

The field $\mathbf{B} = \mathbf{B}(\mathbf{r};\omega|\boldsymbol{\mu})$ can be found from the vector potential $\mathbf{A}$ that solves the inhomogeneous Maxwell equation

$$\nabla\times\nabla\times\mathbf{A} - k_0^2\varepsilon(\mathbf{r})\mathbf{A} = \mu_0\nabla\times\boldsymbol{\mu}\delta(\mathbf{r}-\mathbf{r}'), \tag{3.3}$$

where $k_0 = \omega/c$. The right-hand side is the current density corresponding to the magnetic dipole. There is no free charge density and we work in the gauge $\mathbf{E} = \mathrm{i}\omega\mathbf{A}$.

We now focus on the following geometry (Fig. 3.1, right): the position $\mathbf{r}'$ of the source (i.e., where the magnetic noise spectrum is actually needed) is located in vacuum, and the metallic microstructures are filling a domain $\mathcal{D}$ where $\operatorname{Im}\varepsilon(\mathbf{r};\omega) = \sigma(\mathbf{r};\omega)/(\varepsilon_0\omega)$ is nonzero (and large). The outside domain is called $\mathcal{D}'$. There, the vector potential satisfies an inho-

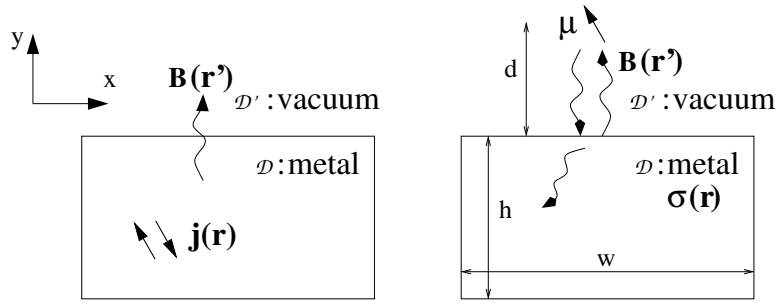

Figure 3.1: Sketch of the considered geometry: (left) current fluctuations in a microstructure generate magnetic field fluctuations $\mathbf{B}(\mathbf{r}')$ at a position position $\mathbf{r}'$ outside it. (right) The magnetic noise spectrum is calculated from the magnetic field radiated by a point magnetic dipole $\boldsymbol{\mu}$ located at $\mathbf{r}'$. $\mathcal{D}$ and $\mathcal{D}'$: domains where the conductivity $\sigma(\mathbf{r};\omega)$ is nonzero or zero, respectively.

mogeneous Helmholtz equation with wavenumber k_0. All length scales we consider (distance dipole–microstructure d, object size) are much shorter than the wavelength so that k_0 is actually very small and can be neglected in a first approximation. This is the magnetostatic regime. (The finite value of k_0 is, of course, at the origin of the nonzero magnetic LDOS in free space.) We cannot make the magnetostatic approximation in $\mathcal{D}$ because there, we have a wavenumber $k_0\sqrt{\varepsilon(\mathbf{r};\omega)} = (1+\mathrm{i})/\delta(\mathbf{r})$, and the (local) skin depth $\delta(\mathbf{r})$ is one of the characteristic length scales at hand. The fields in the domains $\mathcal{D}$ and $\mathcal{D}'$ are connected by the usual matching conditions: the components of $\mathbf{A}$ tangential to the boundary are continuous, and $\mathbf{B}$ is continuous (the material is non-magnetic).

Eq.(3.3) provides a unique solution subject to the boundary condition that at infinity, the field behaves like an outgoing wave. In two [three] dimensions, this corresponds to a vector potential proportional to $\mathrm{e}^{\mathrm{i}k_0 s}/\sqrt{s}$ [$\mathrm{e}^{\mathrm{i}k_0 s}/s$] in the free space domain $\mathcal{D}'$ when the distance $s = |\mathbf{r} - \mathbf{r}'| \to \infty$ to the source becomes large compared to λ. In the magnetostatic limit $k_0 \to 0$, the free space asymptotics is actually never reached at finite distances. The relevant boundary condition is then the same as for the scalar potential of an electric dipole: the vector potential goes to zero like $1/s$ [like $1/s^2$] in two [three] dimensions, respectively.

Since we deal with a metallic object with $|\varepsilon| \gg 1$, it is tempting to perform the calculation based on the surface impedance boundary condition. The latter links the tangential components of magnetic field and vector potential by $B_t = -\mathrm{i}\omega Z A_z$, where $\omega Z = (1+\mathrm{i})/\delta$. Note that this is a local relation that can only hold if the scale of variation of the fields on the object surface is much larger than the skin depth δ. In the present study, a point-like source illuminates the object with its near field [$A_{\mathrm{bulk}}(\mathbf{r} - \mathbf{r}')$ in Eq.(3.5)], and this field shows a typical extension of the order of the object-source distance d. The surface impedance approximation is hence expected to break down for $d \ll \delta$. We shall confirm this explicitly for the planar structures discussed in the following Sec.3.2.

3.2 Infinite planar layer

3.2.1 Wave equation in 2D

The magnetic moment is chosen in the computational plane (the xy-plane), as shown in Fig. 3.1[1]. Adapting the wave equation (3.3) to two dimensions, we find that the vector potential has a single nonzero component that points out of the plane. We then work with a scalar function $A(\mathbf{r}) = A(x, y)$ that solves

$$\nabla^2 A + k_0^2 \varepsilon(\mathbf{r}) A = \mu_0 \left(\mu_y \partial_{x'} - \mu_x \partial_{y'}\right) \delta(\mathbf{r} - \mathbf{r}') \tag{3.4}$$

In a homogeneous medium ('bulk'), the solution with the appropriate boundary conditions is

$$A_{\mathrm{bulk}}(\mathbf{r} - \mathbf{r}') = \frac{\mathrm{i}\mu_0}{4} \left(\mu_y \partial_{x'} - \mu_x \partial_{y'}\right) H_0(k_0 \sqrt{\varepsilon} |\mathbf{r} - \mathbf{r}'|) \tag{3.5}$$

where H_0 is the Bessel function of the third kind (Hankel function), usually denoted $H_0^{(1)} = J_0 + \mathrm{i}Y_0$. From this, we get the magnetic field by taking the 'curl', $B_x = \partial_y A$, $B_y = -\partial_x A$. The resulting self field in free space is

$$\mathrm{Im}\, \mathbf{B}(\mathbf{r}'|\boldsymbol{\mu}) = \tfrac{1}{8}\mu_0 k_0^2\, \boldsymbol{\mu} \tag{3.6}$$

provided the dipole $\boldsymbol{\mu}$ is real. In the magnetostatic limit, this field is negligibly small. The bulk solution Eq.(3.5) then goes over into

$$A_{\mathrm{bulk}}(\mathbf{r} - \mathbf{r}') \approx -\frac{\mu_0}{2\pi} \frac{(x - x')\mu_y - (y - y')\mu_x}{|\mathbf{r} - \mathbf{r}'|^2} \tag{3.7}$$

[1] If the magnetic moment is on the z direction, then the magnetic field only has a nonzero z-component. Its normal derivative jumps on the boundary. $\varepsilon H_n(r \in \underline{\partial\mathcal{D}} = H_n(r \in \overline{\partial\mathcal{D}}$. We compute the magnetic field by solving the wave equation 3.3 too, but replace the vector potential by a scalar magnetic field H_z.

This equation describes the field with which the dipole 'illuminates' the sample. Note that it is scale-free: the typical 'spot size' on the microstructure is only determined by the distance d between dipole and top surface.

3.2.2 Reflected field

In this section, we consider that the boundary of the medium is the plane $y = 0$; the field at the source point $\mathbf{r}' = (0, d)$ is then related to the (Fresnel) reflection coefficients from the surface. We expand the solution to Eq.(3.4) in plane waves (wavevector k parallel to the boundary) and have above the medium ($y > 0$):

$$\begin{aligned} A(x,y) &= \mu_0(\mu_x\partial_{y'} - \mu_y\partial_{x'}) \int_{-\infty}^{+\infty} \frac{\mathrm{d}k}{2\pi} \frac{\mathrm{e}^{\mathrm{i}k(x-x')}}{2\kappa} \\ &\quad \times \left(\mathrm{e}^{-\kappa|y-y'|} + r(k)\mathrm{e}^{-\kappa(y+y')}\right) \end{aligned} \tag{3.8}$$

where $\kappa = \sqrt{k^2 - k_0^2}$. (The square root is chosen such that $\mathrm{Re}\,\kappa \geq 0$ and $\mathrm{Im}\,\kappa \geq 0$.) The coefficient $r(k)$ describes the reflection of the field from the medium boundary, which is discussed in Chap.2. Here in order to find out how the reflection coefficient, hence the magnetic field, depends on wave vector k and skin depth δ, we rewrite Eqs.(2.19) and (2.18) as function of k and δ

$$r(k) = r_{\text{half space}}(k) \equiv \frac{\kappa - \kappa_\mathrm{m}}{\kappa + \kappa_\mathrm{m}}, \qquad \kappa_\mathrm{m} = \sqrt{k^2 - 2\mathrm{i}/\delta^2} \tag{3.9}$$

for a medium with skin depth δ filling the half-space $y < 0$. For a layer (thickness h) on top of a substrate, we have

$$r_{\text{layer}}(k) = \frac{r_{\text{top}} + r_{\text{bottom}}\mathrm{e}^{-2\kappa_\mathrm{m}h}}{1 - r_{\text{top}}r_{\text{bottom}}\mathrm{e}^{-2\kappa_\mathrm{m}h}} \tag{3.10}$$

where $r_{\text{top}} = r_{\text{half space}}$ is given by Eq.(3.9) and r_{bottom} describes the reflection from the layer–substrate interface. It is given by Eq.(3.9) with the replacements $\kappa \mapsto \kappa_\mathrm{m}$, $\kappa_\mathrm{m} \mapsto \kappa_\mathrm{s} = (k^2 - \varepsilon_\mathrm{s}k_0^2)^{1/2}$ where ε_s is the substrate permittivity, details see Sec.2.2.2.

All the relevant information for the magnetic noise power is contained in the reflection coefficient $r(k)$. In fact, when the integral in Eq.(3.8) is performed and the imaginary part taken, it turns out that the reflected waves (second term) dominate over the free space contribution (first term) by at least a factor $\lambda^2\delta/d^3 \gg 1$. This is connected to the fact that the relevant wavenumbers k for our problem are of the order of $1/(y + y') = 1/(2d)$ which is much larger than k_0. We can hence apply the approximation $\kappa \approx |k|$. The reflection coefficient Eq.(3.9) for the metallic half-space then depends only on the parameter $k\delta$. For the metallic layer geometry, we focus for simplicity on a substrate whose conductivity is much smaller than in the metal. The influence of the substrate has been studied by Zhang *et al.* (2005): already a ratio of 10 to 100 between the substrate and layer conductivities is sufficient to make the substrate behave like vacuum. We then have $r_{\text{bottom}} \approx -r_{\text{top}}$ in Eq.(3.10).

3.2.3 Polarization dependence

Let us analyze first the dependence on the orientation of the source dipole. If $\boldsymbol{\mu}$ is perpendicular to the medium (only $\mu_y \neq 0$), the reflected field is given by

$$B_y(\mathbf{r}|\mu_y) = \mu_0\mu_y \int_{-\infty}^{\infty} \frac{\mathrm{d}k}{2\pi}\frac{k^2}{2\kappa} r(k) \mathrm{e}^{\mathrm{i}k(x-x')}\mathrm{e}^{-\kappa(y+y')} \tag{3.11}$$

The limit $\mathbf{r} \to \mathbf{r}'$ yields an imaginary part

$$\mathrm{Im}\, B_y(\mathbf{r}'|\mu_y) = \mu_0\mu_y \mathrm{Im} \int \frac{\mathrm{d}k}{2\pi}\frac{k^2}{2\kappa} r(k) \mathrm{e}^{-2\kappa d}. \tag{3.12}$$

Repeating the calculation for a parallel dipole, we find for $\mathrm{Im}\, B_x(\mathbf{r}'|\mu_x)$ the same expression as Eq.(3.12), and consequently the noise spectrum is isotropic, $\mathcal{B}_{xx} = \mathcal{B}_{yy}$. This is a remarkable property of a laterally infinite structure in 2D. (In 3D, the polarization perpendicular to a planar interface has a noise power twice as large as the parallel polarization (Varpula & Poutanen, 1984; Henkel *et al.*, 1999).) We show below that a significant polarization anisotropy arises above a metallic wire of finite width.

3.2.4 Wavevector dependence

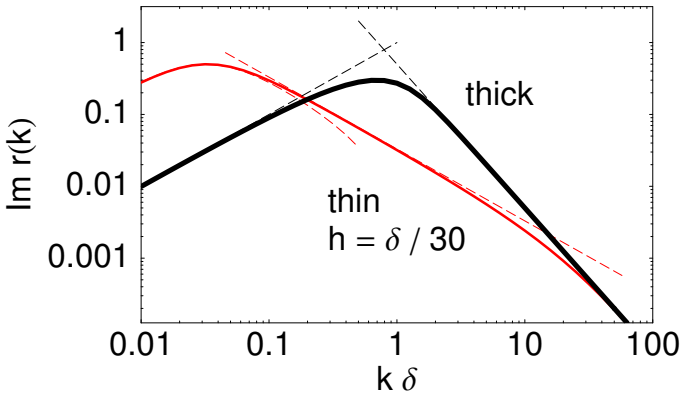

Figure 3.2: Reflection coefficients Eqs.(3.9) and (3.10) for thin and thick metallic layers. We plot the imaginary part only. The dashed lines represent the formulas of Table 3.1. The wavenumber is scaled to the inverse skin depth $1/\delta$. For the thick layer, $h = \infty$. We take the conductivity of gold at room temperature and a frequency $\omega/2\pi \approx 1.1\,\mathrm{MHz}$ in all figures. This leads to the value $\delta = 71\mu\mathrm{m}$ and a vacuum wavelength $\lambda \approx 3.8 \times 10^6\delta$.

The reflection coefficient Eq.(3.10) is plotted in Fig. 3.2 for typical layers. Consider first a thickness larger than a few skin depths. One observes a maximum value of its imaginary part (relevant for the magnetic LDOS) when the decay constant $\kappa \approx k$ is matched to $1/\delta$. This is

confirmed by an asymptotic analysis whose results are given in Table 3.1. (See (Henkel *et al.*, 1999; Biehs *et al.*, 2007) for details on the asymptotic expansion.) One of the two limiting cases (namely $k_0 \ll k \ll 1/\delta$) corresponds precisely to the surface impedance approximation where the reflection coefficient Eq.(3.9) is approximated by

$$r(k) \approx -1 + (1+\mathrm{i})|k|\delta \tag{3.13}$$

Here, the skin depth is much smaller than the lateral period and the field barely penetrates into the material. Fig. 3.2 and Table 3.1 show strong deviations in the opposite regime $k \gg 1/\delta$ that is relevant at distances $d \ll \delta$.

Consider now a layer much thinner than the skin depth. From Fig. 3.2, different regimes can be read off that are separated on the k-axis by the scales $h/\delta^2 \ll 1/h$, as can be seen in Fig. 3.2. It is worth noting that for small k, thin layers show even larger losses [$\mathrm{Im}\, r(k)$] than thick ones; the maximum is shifted towards the smaller value $k \sim h/\delta^2$ and has a larger amplitude. This behaviour has been recognized before in magnetic noise studies in the kHz range (Varpula & Poutanen, 1984). In the infrared range, it is also well known that the absorption by a metallic layer can be optimized at a specific thickness. (See, e.g., (Bauer, 1992) for incident far-field radiation where $|k| \leq k_0$.) Conversely, for a given thickness h and dipole distance d, the magnetic noise power shows a maximum as the skin depth is changed (Varpula & Poutanen, 1984; Scheel *et al.*, 2005). This 'worst case' occurs when the characteristic wavevector $1/d$ is matched to h/δ^2.

	$k \ll 1/\delta$	$1/\delta \ll k$	
$\mathrm{Im}\, r_{\mathrm{half\ space}}(k)$	$k\delta$	$\dfrac{1}{2k^2\delta^2}$	
	$k \ll 1/\delta$	$h/\delta^2 \ll k \ll 1/h$	$1/h \ll k$
$\mathrm{Im}\, r_{\mathrm{layer}}(k)$	$\mathrm{Im}\, \dfrac{-1+(1+\mathrm{i})k\delta}{1+\mathrm{i}k\delta^2/h}$	$\dfrac{h}{k\delta^2}$	$\dfrac{1}{2k^2\delta^2}$

Table 3.1: Asymptotic approximations to the reflection coefficients from a half-space and a layer. We distinguish between thin (thickness $h \ll \delta$) and thick layers ($h \geq \delta$, 'half space'). The first and second columns (thin layer) overlap in an intermediate k-range (see Fig. 3.2). The magnetostatic limit $k_0 \ll k$ is taken throughout. These formulas are plotted as dashed lines in Fig. 3.2.

3.2.5 Distance dependence

The asymptotics in k-space translate into power laws for the dependence of the magnetic power spectrum $\mathcal{B}_{ii}(d;\omega)$ on distance d, as shown in Fig. 3.3. In fact, the integrand in Eq.(3.12) peaks around $k \sim 1/(2d)$, and the result of the integration is determined, to leading order, by the behaviour of $r(k)$ in this range. We thus find the power laws summarized in Table 3.2 and visible in Fig. 3.3. We use as convenient unit in all the plots the noise level $\mu_0 k_\mathrm{B} T/(\omega\delta^2)$. Normalized to blackbody radiation (in 2D free space), this level is $(2/(k_0\delta))^2 \sim 1.5 \times 10^{12}$ at

1.1 MHz for gold at room temperature, a striking illustration of the Purcell effect (Purcell *et al.*, 1946). A common trend is that the magnetic noise power increases as the metallic medium is approached. As the distance d is getting much smaller than the thickness h, thin and thick layers behave the same, as expected. At larger distances, but still smaller than the skin depth, the noise power is proportional to the volume of metallic material, hence to the layer thickness (Henkel & Pötting, 2001; Folman *et al.*, 2002). This trend is reversed for $d > \delta\sqrt{\delta/2h}$ where thin layers give a larger noise level than thick ones (Varpula & Poutanen, 1984; Scheel *et al.*, 2005).

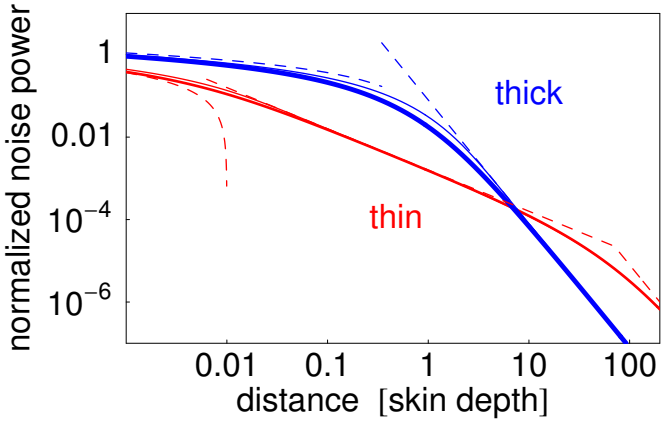

Figure 3.3: Local magnetic noise power $\mathcal{B}_{ii}(d;\omega)$ vs. distance from metallic layer in double logarithmic scale (2D calculation). Top curve [blue]: thick layer; bottom curve [red]: thin layer. The dashed lines give the leading order power laws of Table 3.2. The thick curves arise from the numerical integration of Eq.(3.8), the thin curves are an interpolation formula described in the text. The magnetic noise power is isotropic above a planar structure in 2D (the perpendicular and parallel field components have the same power). It is scaled to $\mu_0 k_B T/(\omega\delta^2)$, and the distance is scaled to the skin depth δ. Thin [thick] layer: $h = 0.01\,\delta$ [$3\,\delta$].

	$d \ll \delta$	$\delta \ll d$	
$\mathcal{B}_{ii,\text{half space}}(d)$ (unit: S_B)	$\dfrac{\log(\delta/d)}{2\pi}$	$\dfrac{\delta^3}{4\pi d^3}$	
	$d \ll h \ll \delta$	$h \ll d \ll \delta^2/h$	$\delta^2/h \ll d$
$\mathcal{B}_{ii,\text{layer}}(d)$ (unit: S_B)	$\dfrac{\log(h/d)}{2\pi}$	$\dfrac{h}{2\pi d}$	$\dfrac{\delta^4}{4\pi h d^3}$

Table 3.2: Power laws for the magnetic noise spectrum in two dimensions above a half space and a thin metallic layer (dashed lines in Fig. 3.3). The noise spectrum is given in units of $S_B = \mu_0 k_B T/(\omega\delta^2)$.

A reasonably accurate approximation that interpolates between these power laws can be found by performing the k-integral using the asymptotic formulas of Table 3.1 in their respective domains of validity. The result is a sum of incomplete gamma functions $\Gamma(n, x, x')$ ($n = 0, 1, 2$) that is plotted as thin lines in Fig. 3.3 (for details see the appendix). We have

checked that the asymptotics of the gamma function reproduce the power laws summarized in Table 3.2. There are regimes where the sub-leading terms give significant corrections, in particular in the transition regions between the power laws.

Finally, the surface impedance approximation gives a magnetic noise that is represented in Fig. 3.3 by the dashed line close to the 'thick layer' for $d > \delta$. The agreement with the full calculation in this range is expected: the 'illuminating field' is getting more and more uniform on the scale of the skin depth. At shorter distances, the surface impedance approximation severely overestimates the noise level because it cannot describe properly field variations on scales smaller than δ. For the thin layer, the conventional surface impedance approach gives a wrong result even if $d > \delta$ because top and bottom surfaces do not decouple from each other. This can be repaired using effective (thickness-dependent) surface impedances, see, e.g., Tuncer & Neikirk (1993) and citations therein.

3.3 Boundary integral equations

We now describe numerical calculations that we have performed to estimate the importance of the finite lateral size of the metallic structure. This is particularly relevant, for example, in atom chips where a continuous metallic layer is etched to define wires that can be addressed with different currents (Folman *et al.*, 2002; Reichel, 2002; Fortágh & Zimmermann, 2007). It is actually desirable to minimize the amount of metallic material, leaving just a few wires to create the fields for atom trapping. In fact, it has been argued that the magnetic noise power roughly scales with the metallic volume as long as the characteristic distances are smaller than the skin depth (Henkel & Pötting, 2001; Folman *et al.*, 2002). For laterally finite structures, this claim as well as other calculations have been based so far on approximate methods that fail to reproduce even the planar layer to within a factor of two or three (Henkel & Pötting, 2001; Lin *et al.*, 2004; Henkel, 2005; Dikovsky *et al.*, 2005). The numerical results we describe here are a first step toward an accurate estimate of magnetic noise power near structures of finite size.

3.3.1 Integral equations

Within the assumption of near field radiation being in equilibrium with the metallic object, we compute the noise power from the magnetic Green function in Eq.(3.1). The magnetic field radiated by a point source and reflected by the object solves the wave Eq.(3.4). We reformulate the wave equation in terms of boundary integral equations using Green theorem. This has been described elsewhere (Nieto-Vesperinas, 1991; Harrington, 1993; Rockstuhl *et al.*, 2003; Rogobete & Henkel, 2004). We review the basic formulas and outline the main difficulties

here.

$$\mathbf{r} \in \mathcal{D}' : \quad A(\mathbf{r}) = A_{\rm bulk}(\mathbf{r}-\mathbf{r}') - \oint_{\overline{\partial\mathcal{D}}} \mathrm{d}a(\mathbf{x}) \left[G_1(\mathbf{r}-\mathbf{x})F(\mathbf{x}) - \frac{\partial G_1}{\partial n}(\mathbf{r}-\mathbf{x})A(\mathbf{x}) \right] , \quad (3.14)$$

$$\mathbf{r} \notin \mathcal{D} : \quad A(\mathbf{r}) = \oint_{\underline{\partial\mathcal{D}}} \mathrm{d}a(\mathbf{x}) \left[G_\varepsilon(\mathbf{r}-\mathbf{x})F(\mathbf{x}) - \frac{\partial G_\varepsilon}{\partial n}(\mathbf{r}-\mathbf{x})A(\mathbf{x}) \right] . \quad (3.15)$$

where $A_{\rm bulk}(\mathbf{r}-\mathbf{r}')$ is given in Eq.(3.5), $\mathrm{d}a(\mathbf{x})$ the (scale) surface element at the integration point $\mathbf{x}$. The nonzero component A of the vector potential and its normal derivative $F = \partial A/\partial n \equiv \mathbf{n}\cdot\nabla A$ on the object surface $\partial\mathcal{D}$ ($\mathbf{n}$ is the outward unit normal to $\partial\mathcal{D}$) are both continuous. Actually, F is equal to the tangential magnetic field. G_1 and G_ε are Green functions in free space and object respectively, ie.

$$G_\varepsilon(\mathbf{r}) = \frac{\mathrm{i}}{4} H_0(k_0\sqrt{\varepsilon}|\mathbf{r}|) . \quad (3.16)$$

The integral runs over the 'inner face' $\underline{\partial\mathcal{D}}$ and the 'outer face' $\overline{\partial\mathcal{D}}$ of the boundary of the wire respectively. From Eqs.(3.14) and (3.15), we see that once the vector potential and its normal derivative on the boundary are known, we can compute the vector potential everywhere. Thus we are led to the question: find out the vector potential and its normal derivatives on the boundary. The idea is to approach the evaluate point $\mathbf{r}$ in Eqs.(3.14) and (3.15) on the boundary, so that one gets a self-consistannnt system.

3.3.2 Singularity

We must take care of the singularity of the Green function and its normal derivative when we evaluate Eqs.(3.14) and (3.15) on the boundary. If we would take the magnetostatic limit, $G_1(\mathbf{r}) \to -(2\pi)^{-1}\log|\mathbf{r}|$, the Green functions in vacuum and in the medium would differ (in sub-leading order) by a constant, leading to inconsistencies. We avoid this by retaining the finite value of k_0 even for the vacuum Green function. Using the short-distance asymptotics for the Hankel function, we have

$$r \to 0 : \qquad G_\varepsilon(r) \simeq -\frac{1}{2\pi}\log(k_0\sqrt{\varepsilon}r) + \frac{1}{2\pi}(\log 2 - \gamma) + \frac{i}{4} , \quad (3.17)$$

where γ is the Euler constant. We take the integral over a small surface element σ which is centered around the point $\mathbf{r}$. We assume that $F(\mathbf{x}) = \partial\mathbf{A}(\mathbf{x})/\partial\mathbf{n}(\mathbf{x})$ varies slowly with $\mathbf{x}$ and replace it by its value $F(\mathbf{r})$ at the center of the surface element. We get the approximation of the integral

$$I(\mathbf{r}) = \int_\sigma \mathrm{d}a(\mathbf{x}) G_\varepsilon(\mathbf{r}-\mathbf{x})F(\mathbf{x}) \simeq F(\mathbf{r})\sigma\frac{1}{4\pi}\left(-2\gamma + \mathrm{i}\pi - 2(\log(k_0\sigma\sqrt{\varepsilon}/4) - 1)\right) , \quad (3.18)$$

with this approximation the error of the numerical scheme scales as σ^2.

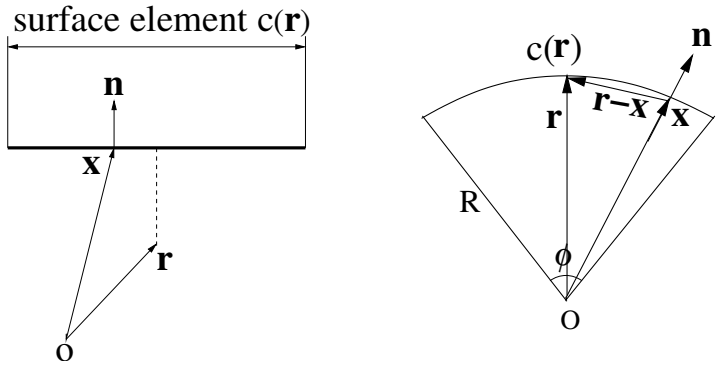

Figure 3.4: The evaluation point $\mathbf{r} = (x_0, y_0)$ approches the boundary, the singularity of $\partial G(\mathbf{r}, \mathbf{x})/\partial n(\mathbf{x})$ under the integral has to be taken into account. $c(\mathbf{r})$ is a small surface element centered aroun $\mathbf{r}$, o the origin, $\mathbf{x} = (x, y)$ the surface point, $\mathbf{n}$ the outward normal unit vector.(left) $c(\mathbf{r})$ is supposed to be flat. (right) $c(\mathbf{r})$ is curvature, R the radius of curvature, ϕ the angle corresponding to the surface element.

Now let us consider the second term in Eqs.(3.14) and (3.15).

$$\oint \mathrm{d}a(\mathbf{x}) \frac{\partial G_\varepsilon}{\partial n}(\mathbf{r} - \mathbf{x}) A(\mathbf{x}) \ . \tag{3.19}$$

Similarly, when the point $\mathbf{r}$ approaches the boundary, the singularity of $\partial G(\mathbf{r}, \mathbf{x})/\partial n(\mathbf{x})$ under the integral has also to be taken into account. We extract a small neighbourhood $c(\mathbf{r})$ centered around the point $\mathbf{r} = (x_0, y_0)$ (See Fig. 3.4). $c(\mathbf{r})$ is so small that we suppose it is flat or the radius of this small surface is infinity. The normal derivative of the Green function at short-distance is approximately given by

$$\begin{aligned} \frac{\partial G_\varepsilon(\mathbf{r}, \mathbf{x})}{\partial n(\mathbf{x})} &\simeq -\frac{\mathbf{n}(\mathbf{x}) \cdot (\mathbf{r} - \mathbf{x})}{2\pi |\mathbf{r} - \mathbf{x}|^2} \\ &= \frac{1}{2\pi} \frac{\mathbf{n} \cdot (\triangle x \mathbf{t} + \triangle y \mathbf{n})}{(\triangle x)^2 + (\triangle y)^2} \\ &= \pm \frac{1}{2\pi} \frac{|\triangle y|}{(\triangle x)^2 + (\triangle y)^2} \ , \end{aligned} \tag{3.20}$$

where $\mathbf{x} = (x, y)$, $\triangle x = x - x_0$, $\triangle y = y - y_0$ and $\mathbf{t}$ is the tangential unit vector, the sign depends on whether the point $\mathbf{r}$ approaches the boundary from inside $(-)$ or outside $(+)$.

Integrating Eq.(3.20) over the surface element $c(\mathbf{r})$ leads to

$$\begin{aligned}\int_{c(\mathbf{r})} \mathrm{d}a(\mathbf{x}) \frac{\partial G_\varepsilon}{\partial n}(\mathbf{r}-\mathbf{x}) A(\mathbf{x}) &\approx \pm\frac{1}{2\pi} \lim_{|\triangle y|\to 0} A(\mathbf{r}) \int_{-c/2}^{c/2} \frac{|\triangle y|}{(\triangle x)^2+(\triangle y)^2} \mathrm{d}\triangle x \\ &= \pm\frac{1}{2\pi} A(\mathbf{r}) \lim_{|\triangle y|\to 0} \arctan\frac{\triangle x}{|\triangle y|}\Bigg|_{-c/2}^{c/2} \\ &= \pm\frac{1}{2} A(\mathbf{r}) \,. \end{aligned} \tag{3.21}$$

The above approximations are sufficient for objects with flat boundary, but for objects with curved boundary as shown in Fig. 3.4 a faster convergence can be obtained by taking into account the finite radius of the extracted small surface element $c(\mathbf{r})$. Recalling the asymptotic for the normal derivative of the Green function at the short-distance limit (the first line in Eq.(3.20)) and considering $\mathbf{r}$ on the curved boundary (as shown in the right of Fig. 3.4), we have

$$\mathbf{n}(\mathbf{x})\cdot(\mathbf{r}-\mathbf{x}) = -2R\sin^2\left(\frac{\phi(\mathbf{r})}{4}\right) \,, \tag{3.22}$$

$$|\mathbf{r}-\mathbf{x}|^2 = 4R^2\sin^2\left(\frac{\phi(\mathbf{r})}{4}\right) \,, \tag{3.23}$$

where R is the radius of curvature, ϕ the angle corresponding to the observation point $\mathbf{r}$. R and ϕ are both finite for a curved surface element; but $R\to\infty$ and $\phi\to 0$ for a flat one. Integrating $\partial G(\mathbf{r},\mathbf{x})/\partial n(\mathbf{x})$ over the small neighborhood $c(\mathbf{r})$ gives

$$\begin{aligned}\int_{c(\mathbf{r})} -\frac{\mathbf{n}(\mathbf{x})\cdot(\mathbf{r}-\mathbf{x})}{2\pi|\mathbf{r}-\mathbf{x}|^2}\mathrm{d}a(\mathbf{x}) &= \int_{c(\mathbf{r})}\frac{1}{4\pi R}\mathrm{d}a(\mathbf{x}) \\ &= \frac{\phi(\mathbf{r})}{4\pi} \,, \end{aligned} \tag{3.24}$$

If $R\to\infty$, the boundary is flat, $\mathbf{n}\cdot(\mathbf{r}-\mathbf{x})=0$, then the above integral is zero. That is why we can ignore it for objects with flat boundaries. Note that if the evaluation point approaches the curved boundary from outside or inside, then the δ-function implied by Eq.(3.21) has to be taken into account too

$$A(\mathbf{r})\int_{c(\mathbf{r})}\frac{\partial G(\mathbf{r},\mathbf{x})}{\partial n(\mathbf{x})}\mathrm{d}a(\mathbf{x}) = \left(\pm\frac{1}{2}+\frac{\phi(\mathbf{r})}{4\pi}\right)A(\mathbf{r}) \,. \tag{3.25}$$

Applying Eq.(3.25) in Eqs.(3.14) and (3.15) and denoting the rest of the surface integral (excluding c) by $\mathcal{P}\int$, we get

$$\begin{aligned}\left(\frac{1}{2}+\frac{\phi(\mathbf{r})}{4\pi}\right)A(\mathbf{r}) &= A_{\mathrm{bulk}}(\mathbf{r}-\mathbf{r}') - \\ &\quad \mathcal{P}\int_{\underline{\partial\mathcal{D}}}\mathrm{d}a(\mathbf{x})\left[G_1(\mathbf{r}-\mathbf{x})F(\mathbf{x}) - \frac{\partial G_1}{\partial n}(\mathbf{r}-\mathbf{x})A(\mathbf{x})\right] \,, \end{aligned} \tag{3.26}$$

$$\left(\frac{1}{2}-\frac{\phi(\mathbf{r})}{4\pi}\right)A(\mathbf{r}) = \mathcal{P}\int_{\underline{\partial\mathcal{D}}}\mathrm{d}a(\mathbf{x})\left[G_\varepsilon(\mathbf{r}-\mathbf{x})F(\mathbf{x}) - \frac{\partial G_\varepsilon}{\partial n}(\mathbf{r}-\mathbf{x})A(\mathbf{x})\right] \,. \tag{3.27}$$

$\phi \neq 0$, when the above two Eqs.(3.26) and (3.27) are applied for curved objects for example cylindrical superconducting wires or the round smooth corner of a rectangular wire; wheras $\phi = 0$ for flat boundaries, for example the flat parts of a rectangle and a strip. Both the observation point $\mathbf{r}$ and the integration points $\mathbf{x}$ are taken on the object boundary $\partial\mathcal{D}$ here. The unknowns in the above two equations are just the vector potential and its normal derivatives. Note that extracting the singularities results in a different prefactor in the left of the equations. In the next Sec.3.4, we will see that for a circular wire with the same disrcetized element (300 elements) on the boundary, applying the curvature coorection (Eq.3.24) leads to a faster convergence.

3.3.3 Reflected field

Once the fields A, F are known on the surface, the reflected field at the source position ($\mathbf{r}'$) can be found from Eq.3.40 without the first term

$$A_{\mathrm{ref}}(\mathbf{r}') = -\oint_{\overline{\partial\mathcal{D}}} \mathrm{d}a(\mathbf{x}) \left[G_1(\mathbf{r}'-\mathbf{x})F(\mathbf{x}) - \frac{\partial G_1}{\partial n}(\mathbf{r}'-\mathbf{x})A(\mathbf{x}) \right] . \tag{3.28}$$

Note that G_1 and $\partial G_1/\partial n$ are both essentially real here (the imaginary parts scale with k_0). The magnetic noise, via $\mathrm{Im}\,\mathbf{B}(\mathbf{r}')$, is thus determined by the imaginary parts of A and F on the object boundary. This is not surprising since the induced current density is $\sigma E = \mathrm{i}\omega\sigma A$.

3.3.4 Numerics

For numerical solution, we discretize Eqs.(3.26) and (3.27) on a finite element decomposition of the object boundary and approximate the integrals by Riemann sums. This is the so called "method of moments" (Rogobete & Henkel, 2004; Bancroft, 1996). The integrals are evaluated at discrete points centered in the decomposition elements, and each point $\mathbf{r}_i$ carries two unknowns $A_i = A(\mathbf{r}_i)$ and $F_i = F(\mathbf{r}_i)$. Eqs.(3.26) and (3.27) are transformed into a linear system, which can be solved with standard numerical tools.

3.4 Circular wire

In this section we check accuracy of numerics by evaluating the magnetic field around a circular wire surrounded by vacuum (see Fig. 3.5) numerically, and then comparing with the analytical results. A magnetic dipole $\boldsymbol{\mu} = (\mu, 0)$ is placed at the center of the circle, the radius of the circle is $R = 10\mu\mathrm{m}$. We compute the magnetic field at $r = 20\mu\mathrm{m}$ from the origin O. φ denotes the polar angle between the evaluation point $\mathbf{r}$ and the dipole $\boldsymbol{\mu}$. First we deduce the analytical formulas for magnetic field at r, then compute the magnetic field using the boundary integral Eqs.(3.26) $\sim$ (3.28) numerically. Finally, we compare the results to validate our numerical method.

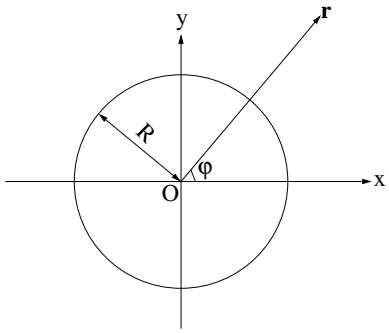

Figure 3.5: A circular wire in vacuum. A unit magnetic dipole $\boldsymbol{\mu} = (1, 0)$ is placed at the origin O, the radius is $R = 10\mu$m, $r = |\mathbf{r}| = 20\mu$m is the distance between the origin and the observation point $\mathbf{r}$, φ the polar angle between $\mathbf{r}$ and the dipole $\boldsymbol{\mu}$.

3.4.1 Analytics

The magnetic field caused by the magnetic dipole $\boldsymbol{\mu} = (\mu, 0)$ can be discribed with a vector potential $\mathbf{A} = \mathbf{e_z} A$, which can be given in polar coordinates inside and outside the circle

$$inside: \quad A(r) = A^{\varepsilon}_{\text{dip}} + \beta \frac{\mathrm{i}\mu_0 k_0 \sqrt{\varepsilon} \sin\varphi}{4} J_1(k\sqrt{\varepsilon} r)\mu \ , \tag{3.29}$$

$$outside: \quad A(r) = \gamma A^{1}_{\text{dip}} \ , \tag{3.30}$$

where $A^{\varepsilon}_{\text{dip}}$ and A^{1}_{dip} are the vector potentials produced by a dipole in object with permetivity ε and vacuum ($\varepsilon = 1$) respectively,

$$A^{\varepsilon}_{\text{dip}} = \mu \frac{\mathrm{i}\mu_0 k_0 \sqrt{\varepsilon} \sin\varphi}{4} H_1(k_0\sqrt{\varepsilon} r) \ , \tag{3.31}$$

$$A^{1}_{\text{dip}} = \frac{\mathrm{i}\mu_0 k_0 \sin\varphi}{4} H_1(k_0 r) \ . \tag{3.32}$$

Here $\sin\phi = y/r$ as defined in Fig. 3.5 and H_1 is the first order of Hankel function; J_1 the first order of Bessel function, β corresponds to the field reflected from the boundary of the circular wire, γ determines the transmitted field out of the wire. β and γ can be fixed by the boundary conditions. Because A and its radial derivative $\partial A/\partial r$ are both continous across the boundary and we use H_1' and J_1' denote the deviatives of H_1 and J_1 respectively, we have on the boundary

$$\sqrt{\varepsilon} H_1(k_0\sqrt{\varepsilon} R) + \beta\sqrt{\varepsilon} J_1(k_0\sqrt{\varepsilon} R) = \gamma H_1(k_0 R) \ , \tag{3.33}$$

$$\varepsilon H_1'(k_0\sqrt{\varepsilon} R) + \beta\varepsilon J_1'(k_0\sqrt{\varepsilon} R) = \gamma H_1'(k_0 R) \ . \tag{3.34}$$

Using the Wronskian for the Bessel functions that occurs in the determinant of the linear system, we get

$$\gamma = \frac{2i\sqrt{\varepsilon}/\pi k_0 R}{\sqrt{\varepsilon}J_1'(k_0\sqrt{\varepsilon}R)H_1(k_0R) - J_1(k_0\sqrt{\varepsilon}R)H_1'(k_0R)} , \tag{3.35}$$

$$J_1'(k_0r) = \frac{1}{2}(J_0(k_0\sqrt{\varepsilon}r) - J_2(k_0\sqrt{\varepsilon}r)) , \tag{3.36}$$

$$H_1'(k_0r) = \frac{H_1(k_0r)}{k_0r} - H_2(k_0r) , \tag{3.37}$$

where H_2 is the second order of Hankel function, J_2 the second order of Bessel function. Apply Eq.(3.35) in Eq.(3.29), the magnetic field outside the circular wire can be computed everywhere. The x component of the magnetic field (denoted by B_{xx}) created by this magnetic dipole $\boldsymbol{\mu} = (\mu, 0)$ can be found by taking the y derivative of A

$$\begin{aligned} B_{xx}(r) &= \gamma\partial_y A^I_{dip}(r) \\ &= -\gamma\mu\mu_0\frac{\mathrm{i}}{4}k_0\frac{\partial}{\partial y}(\sin\varphi H_1(k_0r)) \\ &= \gamma\mu\mu_0\frac{\mathrm{i}}{4}k_0(-\frac{1}{r}H_1(k_0r) + k_0\frac{y^2}{r^2}H_2(k_0r)) \end{aligned} \tag{3.38}$$

3.4.2 Numerics

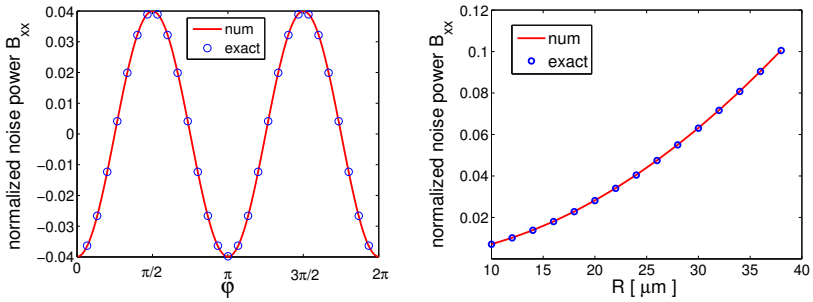

Figure 3.6: (left) Magnetic niose spectra $\mathcal{B}_{xx}$ vs. the evaluation angle ϕ with fixed $r = 20\mu$m. The radius of the circular wire is $R = 10\mu$m. (right) Magnetic niose spectra $\mathcal{B}_{xx}$ vs. R at the fixed eveluation point $r = 40\mu\text{m}, \phi = 5\pi/8$. In both plots the noise is produced by a unit dipole $\boldsymbol{\mu} = (1, 0)$ at the center of the circle and it is normalized by $S_B = \mu_0 k_B T/(\omega\delta^2)$. Circles: based on Eq.(3.38). Solid line: based on the boundary integral equations Eqs.(3.26) and (3.27). The surface is discretized into 300 elements. The skin depth is $\delta = 70\mu$m.

Note in this section the dipole source is inside the circle and along the x direction, the incident field A_{bulk} is still given by Eq.(3.5), but we need move it from Eq.(3.26) to Eq.(3.27). As described in Sec.3.3, evaluate Eqs.(3.26) and (3.27) on the boundary of the circular object to fix the vector potential A and its normal derivative F on the boundary, then apply Eq.(3.28)

to evaluate the vector potential outside A^{out}, finally get the magnetic field B_{xx} created by this dipole by taking the y derivative of A^{out}. We discretize the circle shown in Fig. 3.5 into at least 300 elements which leads to a linear system with 9×10^4 matrix elements. The normalized noise power $\mathcal{B}_{xx}$ at $r = 20\mu\text{m}$ is plotted in the left of Fig. 3.6, it periodically varies as the angle ϕ defined in Fig. 3.5. We plot the magnetic noise $\mathcal{B}_{xx}$ at the fixed eveluation point $r = 40\mu\text{m}, \phi = 5\pi/8$ versus varying radius in the right of Fig. 3.6. The noise increases as the radius increases and the evaluation point gets closer to the surface. It can be seen that the numerical results are in a good agreement with analytical results.

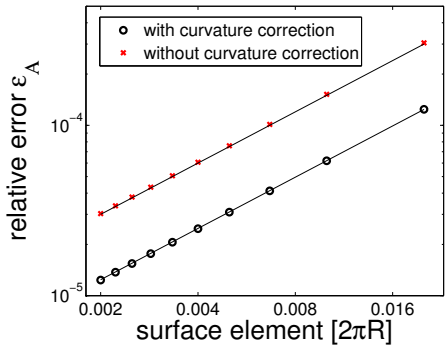

Figure 3.7: Relative error of the vector potential $\mathbf{A}$ vs. the surface elements normalized by $2\pi R$. ϵ_ψ is computed by Eq.(3.39). Circles: A_{num} in Eq.(3.39) is computed with curvature correction by taking into account the finite radius of the surface element ($\phi \neq 0$). Crosses: A_{num} in Eq.(3.39) is computed without curvature correction, the boundary element is supposed to be flat ($\phi = 0$). The error scales as the surface element σ (solid lines). For a circular wire, a faster convergency can be obtained by applying curvature correction. We discretize the surface into 300 uniform elements.

The convergence can be improved by taking into account the finite radius of the discretized surface element (curvature correction, $\phi \neq 0$). We define the relative error of the vector potential as

$$\epsilon_A = \left(\frac{\oint |A_{num}(\mathbf{x}) - A_{ana}(\mathbf{x})|^2 \mathrm{d}\mathbf{x}}{\oint |A_{ana}(\mathbf{x})|^2 \mathrm{d}\mathbf{x}} \right)^{1/2} , \tag{3.39}$$

where A_{ana} is given by Eq.(4.23), A_{num} is defined by Eq.(3.26) or (3.27). We plot the relative error of the scalar potential ϵ_A vs the discretized surface element in Fig. 3.7. Circles are computed with curvature correction, crosses are computed without curvature correction. It is obvious that a faster convergence can be obtained by applying the curvature correction in the boundary integral equations. We discretize the boundary into uniform elements throughout this chapter. One can also discretize the boundary into non-uniform elements and use 'Galerkin method': expand the integrands in Eq.(3.26) or (3.27) in terms of 'basis functions' (eg. δ-function); then project the vector potential A onto the same basis as 'test functions' to find the expension coefficients. This will leads to similar convergence to the numerics we used.

3.5 Incoherent summation

We outline here the adaptation of the incoherent summation method of (Dikovsky *et al.*, 2005; Henkel & Pötting, 2001; Varpula & Poutanen, 1984) to two dimensions. The thermal spectrum of the current density is given at low frequencies ($\hbar\omega \ll k_B T$) by (Landau *et al.*, 1984)

$$\langle j^*(\mathbf{x};\omega) j(\mathbf{x}';\omega')\rangle = 2\pi\delta(\omega-\omega')2k_B T\sigma(\mathbf{x};\omega)\delta(\mathbf{x}-\mathbf{x}') \; . \tag{3.40}$$

This spectrum is already integrated over a unit length in the z-direction (parallel to the current) along which the current density is assumed to be uniform (two-dimensional geometry). In this formulation, σ is (the real part of) the 3D conductivity that we assume local, as reflected by the spatial δ-correlation. We only take into account currents parallel to the z-direction. Each current element generates a magnetic field in the xy-plane that we compute in the magnetostatic approximation and ignoring the presence of the embedding metal. The latter point is the key approximation made. This gives a magnetic noise spectrum (integrated over a unit length along z)

$$\mathcal{B}_{ij}(\mathbf{x};\omega) = \frac{S_B}{\pi^2}\left(\delta_{ij}(\operatorname{tr} Y) - Y_{ij}\right) \tag{3.41}$$

$$Y_{ij}(\mathbf{x}) = \int\limits_V \mathrm{d}^2\mathbf{x}' \frac{(x_i - x_i')(x_j - x_j')}{|\mathbf{x}-\mathbf{x}'|^4} \tag{3.42}$$

$$S_B = \frac{\mu_0 k_B T}{\omega\delta^2} \; , \tag{3.43}$$

where V is the $2D$ volume occupied by the metal. The 'geometrical tensor' Y_{ij} is dimensionless (a specific 2D property) and depends only on the ratio of observation distance and object size. The skin depth only enters via the scalar factor S_B.

For a microstructure with rectangular cross section, an observer located above the center of the structure sees a noise power

$$\begin{aligned}
\frac{\mathcal{B}_{xx}(d;\omega)}{S_B} &= \frac{1}{2\pi^2}\left[\left[\arctan(\frac{x'}{y-y'})\right]_{x'=-\frac{w}{2}}^{\frac{w}{2}}\right]_{y'=-h}^{0} \\
&\quad + \frac{1}{2\pi^2}\left[\left[\operatorname{Im}\operatorname{Li}_2(\frac{\mathrm{i}x'}{y-y'})\right]_{x'=-\frac{w}{2}}^{\frac{w}{2}}\right]_{y'=-h}^{0} \\
\frac{\mathcal{B}_{yy}(d;\omega)}{S_B} &= \frac{1}{2\pi^2}\left[\left[\arctan(\frac{y-y'}{x'})\right]_{x'=-\frac{w}{2}}^{\frac{w}{2}}\right]_{y'=-h}^{0} \\
&\quad + \frac{1}{2\pi^2}\left[\left[\operatorname{Im}\operatorname{Li}_2(\frac{\mathrm{i}x'}{y-y'})\right]_{x'=-\frac{w}{2}}^{\frac{w}{2}}\right]_{y'=-h}^{0}
\end{aligned} \tag{3.44}$$

where $\operatorname{Li}_n(\cdot)$ is the polylogarithm and we have used the notation

$$\Big[[f(u,v)]_{u=a}^{b}\Big]_{v=c}^{d} \equiv f(a,c) - f(a,d) - f(b,c) + f(b,d) \tag{3.45}$$

By symmetry, $\mathcal{B}_{xy} = \mathcal{B}_{yx} = 0$.

3.6 Finite lateral wire

3.6.1 Single rectangular wire

We have solved the integral equations for rectangular wires of thickness h and width w. In a first step, we have validated our numerical scheme by comparing flat, wide wires ($w \gg h$) to the infinite layer results of Sec.3.2. Typical plots are shown in Fig. 3.8 where the magnetic noise power (symbols) is plotted vs. the distance d above the wire centre. Good agreement with the analytical results for an infinitely wide wire (solid lines) is only obtained at short distance, where for geometrical reasons the wire appears wider. At distances above $20\,\mu\mathrm{m}$, the deviations start to grow. In all the plots, we take a skin depth $\delta = 70\,\mu\mathrm{m}$. The slow convergence in the limit $w \to \infty$ can be attributed to the long-range behaviour of the fields; this is more pronounced in two dimensions compared to three. Note in particular the strong splitting between the two polarization directions for the thick wire that does not occur above an infinitely wide wire in 2D (Sec.3.2.3). Interestingly, the y-component (crosses) shows more noise above a thick wire while this tendency is reversed above a thin wire. This polarization anisotropy could provide a tool to improve the lifetime in a magnetic trap: one orients the static trapping field parallel to direction of the strongest noise. (In fact, trap loss and spin flips are induced by magnetic fields perpendicular to the static trap field.) The choice of a trapping field along the weak noise direction is favorable if one wants to reduce the dephasing rate of the trapped spin states (generated by fluctuations of the Larmor frequency, see (Folman *et al.*, 2002)).

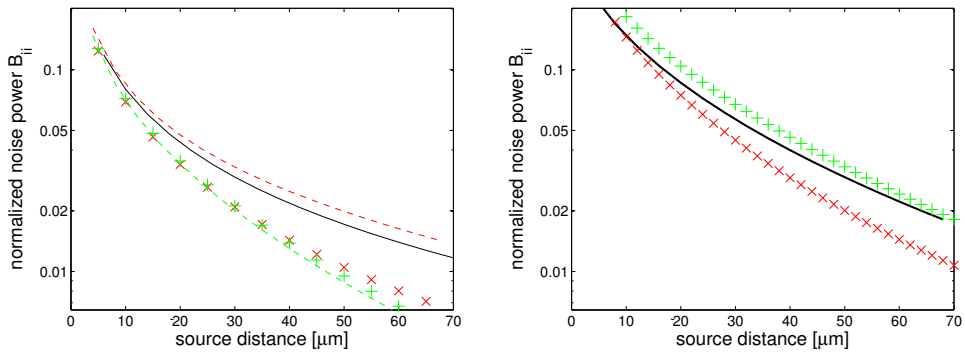

Figure 3.8: Magnetic noise spectra $\mathcal{B}_{ii}(d)$ vs. distance d above the centre of thin (left) and thick (right) metallic wires. Symbols $+$ ($\times$): numerical calculation for the $\mathcal{B}_{yy}$ ($\mathcal{B}_{xx}$) component. Solid lines: infinitely wide wire (layer), as computed in Sec.3.2. Dashed lines: incoherent summation (thin layer only, upper curve: $\mathcal{B}_{xx}$), see Sec. 3.5. Thin wire: width and thickness $200 \times 7\,\mu\mathrm{m}$; thick wire: $200 \times 160\,\mu\mathrm{m}$. The skin depth is $\delta = 70\,\mu\mathrm{m}$.

Another finite-size effect is shown in Fig. 3.9 where the position is varied parallel to the top surface of a thin wire. Above the centre of wide wires, the noise levels are nearly constant

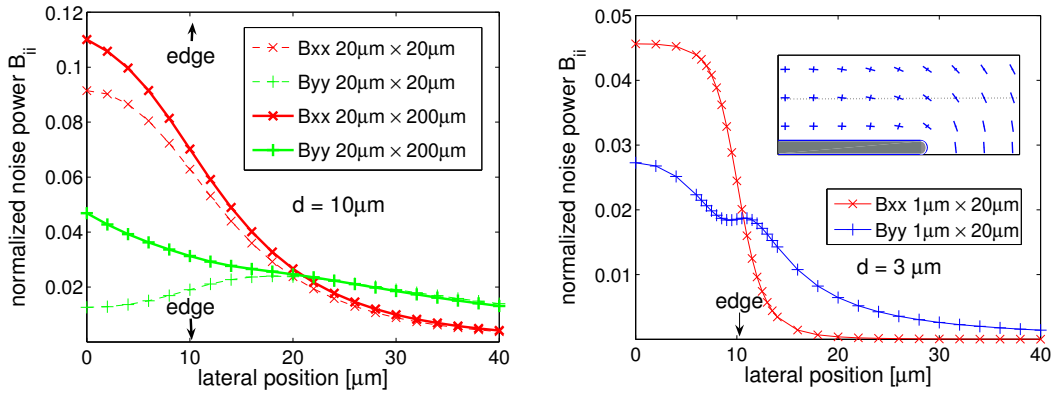

Figure 3.9: Magnetic noise spectra $\mathcal{B}_{ii}(d)$ vs. lateral position, at a fixed distance d. The arrows mark the edges of the wires. Symbols $\times$ [+]: spectrum $\mathcal{B}_{xx}$ [$\mathcal{B}_{yy}$] parallel [perpendicular] to the top face of the wire. Skin depth: $\delta = 70\,\mu$m.
Left panel: thickness and width are $20 \times 200\,\mu$m (wide wire) and $20 \times 20\,\mu$m (narrow wire). Distance $d = 10\,\mu$m. Right panel: thickness and width are $1 \times 20\,\mu$m, distance $d = 3\,\mu$m (see dotted line of inset). Inset: illustration of anisotropic noise near the wire edge. The crosses are oriented along the polarization vectors that show maximum and minimum noise, the 'arm lengths' being proportional to the rms noise. The magnetic field noise is dominantly azimuthal, with field lines circling around the wire. The dotted line ($d = 3\,\mu$m) shows the positions scanned through in the right panel.

(not shown). Beyond the wire edges, one observes a sharp drop in $\mathcal{B}_{xx}$, with a characteristic scale fixed by the distance. The y-component shows a broad maximum near the edge that is more pronounced for narrow wires. This is due to a gradually changing direction of maximum noise that is 'azimuthal' with respect to the object, as expected for magnetic fields generated by currents flowing perpendicular to the computational plane (see inset of Fig. 3.9). We find the direction of maximum noise by looking for the eigenvectors of the symmetric 2×2 matrix $\mathcal{B}_{ij}$. [2]

In Figs. 3.10 and 3.11, the thickness of the wire is changed with the observation point remaining above the centre. We observe an approximately linear increase with the width that saturates slowly. We also note that $\mathcal{B}_{xx}$ (left) levels off faster than $\mathcal{B}_{yy}$ (right). The difference between Fig. 3.10 and Fig. 3.11 is the distance of observation: at short distance (Fig. 3.10), the largest widths show a noise power fairly close to the planar layer limit (cf. the symbols at the right end). At distances comparable to the skin depth (Fig. 3.11), the deviations from the planar layer limit (symbols) are still large. Note also that the noise has dropped in amplitude and that the increase with width is slower.

This behaviour can be qualitatively understood using the 'incoherent summation' approximation The solid lines in Fig. 3.10 demonstrate that incoherent summation gives a reliable

[2] In Fig. 3.9, careful look shows that the eigenvectors are not orthogonal very near to the wire's corner. This is due to an artefact of our numerical method that converges very slowly at these points.

approximation if the skin depth is the largest length scale (not true for the thick wire). The noise power always increases with the metallic volume within this approximation, however, and it may also happen that a wider wire produces a slightly weaker noise (x-polarized curve for a thin wire in Fig. 3.10). This is qualitatively similar to the trend of Fig. 3.3 where a thick layer can produce less noise than a thin one at distances larger than the skin depth. The polarization anisotropy is also qualitatively reproduced by the incoherent summation method, although $\mathcal{B}_{xx}$ is overestimated (Fig. 3.10 left). In fact, due to damping on the scale of δ, not the entire volume of the thick layer contributes to the noise. The dashed lines in Fig. 3.8 and further calculations show that the quantitative agreement is systematically better for the field component perpendicular to the nearest metal surface (here, $\mathcal{B}_{yy}$).

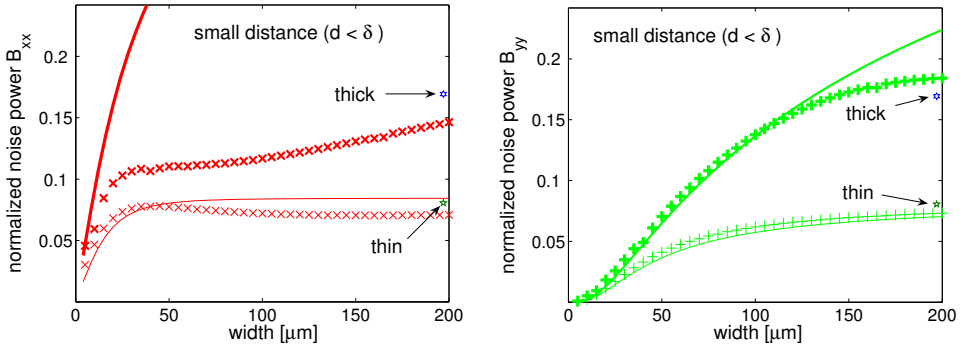

Figure 3.10: Magnetic noise spectra vs. the width of a rectangular wire. (left) x-polarization, parallel to the top face; (right) y-polarization. Symbols: numerical calculations; solid lines: incoherent summation approximation (see Sec.3.5). The symbols on the right margin give the values for an infinitely wide wire (layer). The observation point is located above the wire centre, at a distance $d = 10\,\mu\mathrm{m}$. The wire thickness is $7\,\mu\mathrm{m}$ (thin) and $160\,\mu\mathrm{m}$ (thick). Skin depth: $\delta = 70\,\mu\mathrm{m}$.

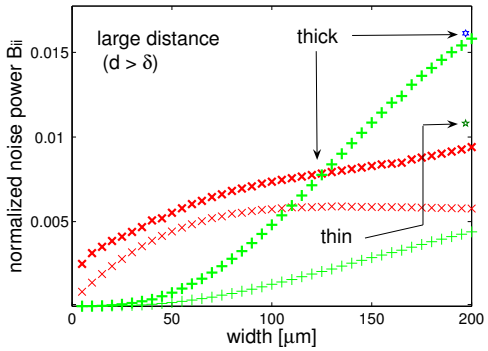

Figure 3.11: Same as Fig. 3.10, but at an observation distance $d = 75\,\mu\mathrm{m}$. Results from the incoherent summation are not shown, as they strongly deviate.

3.6.2 Multiple wires

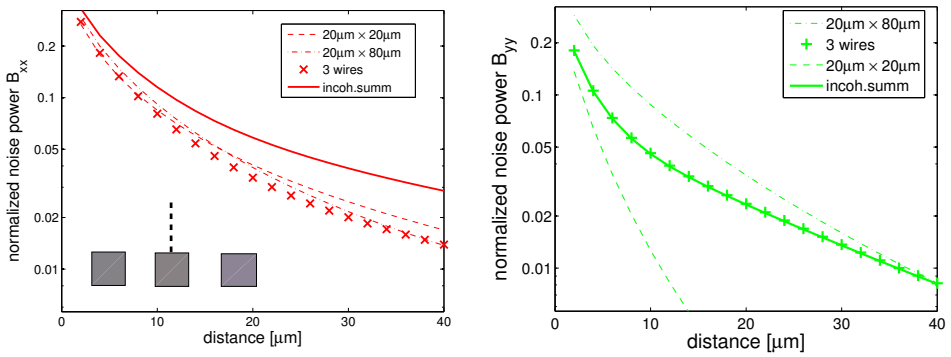

Figure 3.12: Noise power generated by three wires, as a function of distance (see inserted sketch, with the dashed line illustrating the observation points). The wires have a quadratic cross section $20\,\mu\mathrm{m} \times 20\,\mu\mathrm{m}$ and are separated by a gap of $20\,\mu\mathrm{m}$. The noise is measured above the center of the central wire. Left panel: horizontal polarization, right panel: vertical polarization. Symbols: numerical result; solid line: incoherent summation. For comparison is shown: a single wire of same cross section (dashed line) and a wide wire $20\,\mu\mathrm{m} \times 80\,\mu\mathrm{m}$ with approximately the same volume (dash-dotted line). Skin depth $\delta = 70\,\mu\mathrm{m}$.

This is the generic situation in miniaturized magnetic traps ('atom chips') with wires being defined by etchings in a metallic layer. We consider three wires of identical cross section and smaller than the skin depth. We show in Fig. 3.12 the dependence on the vertical distance, above the central wire. Our results interpolate smoothly between a single narrow wire ($d \ll w$) and a single wide wire ($d \gg 2w$), as could have been expected. In fact, the three geometries give nearly the same noise in the azimuthal (B_x) polarization. While for B_y, larger differences can be seen in the right of Fig. 3.12. The incoherent summation approximation overestimates B_x noise component (similar to Fig. 3.10). We attribute this to correlations between the current fluctuations in neighboring wires that are not captured by incoherent summation. On the other hand, this approximation gives an excellent agreement for the weaker noise component B_y.

When we shift the observation point laterally, along the axis connecting the wire centres, we get Fig. 3.13. The stronger B_x-polarization shows maxima of noise above each wire, as expected. In the B_y-polarization, a maximum occurs in the gap between the wires. This conforms to the general trend of 'azimuthal noise' illustrated in Fig. 3.9 (inset). It is also interesting that above the central wire ($x = 0$), three wires generate less noise than only one and also less than a single wide wire (approximately a merger of the three). This observation goes into the same direction as the experiments reported by Nenonen *et al.* (1996) where a reduction of thermal magnetic fields was achieved by cutting a metallic film into stripes. We attribute this behaviour to negative correlations between the currents in neighboring wires brought about by the propagation of the magnetic field between them. In fact, the noise could only increase if the wire currents were strictly uncorrelated.

The performance of the incoherent summation approximation (solid lines) can be clearly

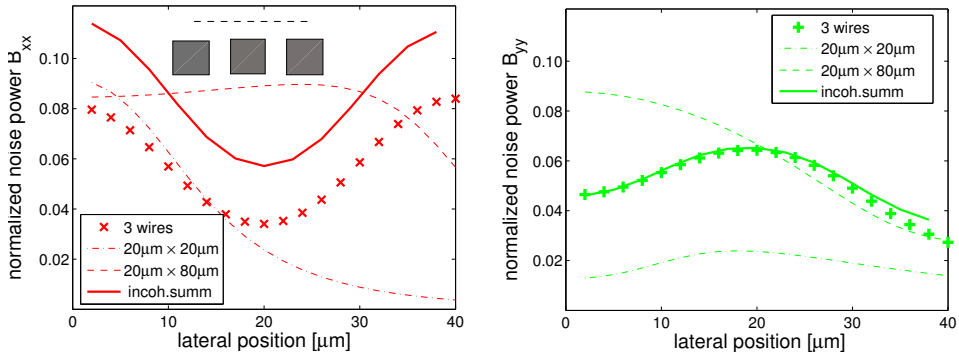

Figure 3.13: Same as Fig. 3.12, but at fixed distance $d = 10\,\mu\mathrm{m}$, scanning the lateral position. $x = 0$ is above the center of the central wire.

seen, the trends being similar to Fig. 3.12: good agreement for the B_y-polarization, overestimation of the perpendicular case due to the neglect of correlation effects.

3.7 Conclusion

We have described in this chapter numerical and analytical results for the thermal fields surrounding a two-dimensional metallic object of arbitrary cross-section. The role of the skin depth δ as a characteristic length scale has been highlighted. At distances smaller than δ, the spectral noise power roughly scales with the volume of the metallic material (Figs. 3.3, 3.10, 3.11). We have reviewed a simple method based on this idea, the 'incoherent summation approximation'. It systematically overestimates the noise power in one of the two field polarizations, but otherwise reproduces the main features as long as the skin depth is the largest scale. The strong polarization anisotropy that we have found suggests strategies to minimize loss or decoherence due to thermal magnetic fields, that has been observed in recent experiments (Harber *et al.*, 2003; Lin *et al.*, 2004; Zhang *et al.*, 2005): this can be done by suitably choosing the direction of the static trapping fields. We have also shown that the noise power can be significantly non-additive when dealing with multiple objects. This could be relevant for the discrepancy between experiment and theory observed in (Zhang *et al.*, 2005), although our method (restricted to 2D) does not permit quantitative predictions of trap lifetimes. Estimation of trap lifetimes (in 3D) above conductors with arbitrary cross-section is our next aim.

Appendix

Uniform approximation

We give here the example how we get the power laws for magnetic noise spectrum listed in Table 3.2 from Eq.(3.12). The integral over k in Eq.(3.12) can be performed analytically if the power-law approximations of Table 3.1 are used for the reflection coefficients. We split

the integration range at the crossing points between the power laws and sum the contributions. The full expression is cumbersume, and we quote here only the most complicated case, the thin layer in the range $k_0 \ll k \ll 1/\delta$ (first column of Table 3.1). The integral can be handled with the formula

$$\begin{aligned}
&\int_{k_1}^{k_2} \mathrm{d}k \, \frac{(-1+(1+\mathrm{i})k\delta)k\,\mathrm{e}^{-2kd}}{1+\mathrm{i}kt} \\
&= (1-\mathrm{i})\frac{\delta}{4td^2}\Gamma(2,2k_1d,2k_2d) \\
&\quad + \frac{f}{2d}\Gamma(1,2k_1d,2k_2d) \\
&\quad + \frac{\mathrm{i}\,f}{t}\,\mathrm{e}^{-2\mathrm{i}d/t}\Gamma(0,2k_1d-2\mathrm{i}d/t,2k_2d-2\mathrm{i}d/t)
\end{aligned} \tag{3.46}$$

where $t = \delta^2/h$ and $f = (1+\mathrm{i})\delta/t^2 + \mathrm{i}/t$. In this case, $k_1 = k_0$ and $k_2 = (t\delta)^{-1/2}$. The incomplete gamma function is defined by

$$\Gamma(n,b,a) = \Gamma(n,b) - \Gamma(n,a) \tag{3.47}$$

$$\Gamma(n,a) = \int_a^\infty \mathrm{d}t\, t^{n-1}\mathrm{e}^{-t} \tag{3.48}$$

Using the asymptotics of the gamma function Abramowitz & Stegun (1972), we get the power laws in Table 3.2. The logarithmic behaviour arises from

$$a \ll 1 : \qquad \Gamma(0,a) \approx -\log a. \tag{3.49}$$

Chapter 4

Magnetic traps with superconducting wires

Recently superconducting atom chips have been suggested as a perspective way to improve lifetimes and coherence of the trapped atoms, because the thermal noise and technical noise can be significantly reduced by using superconductors, especially those in the Meissner state. In this chapter, we investigate magnetic traps formed by superconducting wires carrying a transport current and placed in a bias field. The trapping field and distribution of supercurrents around superconducting wires with arbitrary cross-sections are computed numerically and analytically. Properties and Parameters of magnetic traps based on superconducting chips are discussed. Critical magnetic field and transport current are considered and estimated approaximationally. This chapter is based on the work collaborated with the group of Ron Folman, which leads to the paper Dikovsky *et al.* (2008).

4.1 Superconducting atom chips

Compared to a normal metal, a superconductor (SC) has several advantages for atom chips. Due to the infinite conductivity, superconducting wires significantly reduce Johnson noise, which is the dominant source of atom loss especially when the trap distance is less than $10\mu\mathrm{m}$. And there is practically zero voltage drop across the superconducting elements, whereas in normal metallic chips the relatively high electrical field across wires leads to deformation and shift of the potential well on atom chips (Fortágh & Zimmermann, 2007). Besides, technical noise can be reduced by using persistent currents, which are carried in closed loops without any damping. These persistent currents allow one to disconnect superconducting wires from current supplies during the experiments, avoiding the noise caused by the instability of the current supplies. These unique properties of superconductors make them popular for atom chips.

Atom chips with superconducting (SC) elements have been realized first by Nirrengarten *et al.* (2006); Mukai *et al.* (2007). Both groups trapped ^{87} Rb atoms with 'U' and 'Z' traps formed by superconducting wires. Nirrengarten *et al.* (2006) trapped up to 8.2×10^5 atoms in a

Ioffe-Pritchard trap at a distance of $440\mu\mathrm{m}$ from the chip surface, with a temperature of $40\mu\mathrm{K}$. The current-carrying wires were made of niobium and the chip was operated at a temperature of $4.2\mathrm{K}$. The lifetime was observed to be about $115\mathrm{s}$, which is slightly longer than that of trapped atoms above normal metallic atom chips. Based on this work, a BEC has been first observed on a superconducting niobium atom chip by Roux *et al.* (2008). 1×10^4 Rb atoms trapped at a distance of $85\mu\mathrm{m}$ from the chip surface below $100\mathrm{nK}$. The atom cloud can be compressed and brought as close as $50\mu\mathrm{m}$ from the chip surface. Mukai *et al.* (2007) applied a persistent current in a 'Z' wire by making it part of a closed loop to remove the technical noise due to the current supply. The 'Z' trap was made of a $100\mu\mathrm{m}$ wide molecular-beam epitaxy-grown MgB_2 strip carrying a supercurrent of $2.5\mathrm{A}$. The atom chip was also operated at a temperature of $4.2\mathrm{K}$.

On the theoretical side, Hohenester *et al.* (2007) estimated that the lifetime of Rb atoms trapped at $1\mu\mathrm{m}$ from a superconducting niobium chip at $4.2\mathrm{K}$ can exceed $1000\mathrm{s}$, whereas, the lifetime drops below $1\mathrm{s}$ at the same distance from a normal metallic chip at the same temperature. They also predicted that at higher distances from a niobium chip, the lifetime of Rb atoms can be much longer up to $10^{11}\mathrm{s}$. Skagerstam *et al.* (2006) also computed the magnetic noise caused by superconductors in the Meissner state and predicted that compared to atoms trapped above a normal metallic chip, the enhancement of lifetime of atoms above a superconducting chip could be millions.

4.2 Properties of superconductors

It is well known when the temperature T, the current I and the external magnetic field B are less than the critical values T_{c1}, I_{c1} and $B_{c1}(T)$, the resistivity of superconductor decreases to zero and the magnetic field is expelled from the superconductor —— the Meissner effect (Landau *et al.*, 1984). In the Meissner state the magnetic field can only penetrate into a superconductor over a small depth λ_L from the surface —— the London penetration depth. It increases with temperature as $\lambda_L(T) = \lambda_L(T=0) \times [1-(T/T_{c1})^4]^{-1/2}$, where $\lambda_L(T=0)$ has an order of $40\mathrm{nm}$ (eg. niobium). The supercurrents only flow within the London penetration depth λ_L, they screen the external magnetic field so that there is no magnetic field beyond the London penetration depth in the superconductors. When the thickness t of the superconducting wire is much larger than the the London penetration depth λ_L, we can suppose that the currents are only on the surface (sheet current approximation) and denote the critical sheet current by J_{c1}.

Superconducting materials are classified as type I and type II according to their different behavior when the magnetic field is increasing. Type I superconductors (pure metals as Pb, Al, Hg) only have the first critical values T_{c1}, I_{c1} and $B_{c1}(T)$. When the temperature, the current and the external magnetic filed are all below the critical values, type I superconductors are in the Meissner state, otherwise, they behave the same as the normal metal. Type II superconductors (Nb and its compound, Mg_2) have the first and second critical values, when the temperature, the current and the magnetic filed are all below the first critical values, they are also in the Meissner state and behave as well as type I superconductors. If any parameters ($T,\ I,\ B$), exceed the first critical values, but still remain below the second critical values T_{c2}, I_{c2} and $B_{c2}(T)$, the type

type I	T_{c1} (K)	λ (nm, 0 K)	B_{c1} (mT)		$J_{c1} = B_{c1}/\mu_0$ (A/m)
Pb	7.2	37	55		4.4×10^4
type II	T_{c2} (K)	λ (nm, 0 K)	B_{c1} (mT)	B_{c2} (T)	j_{c2} (A/m ^{2})
Nb	9.3	39	140	0.28	5×10^{10}
MgB_2	40	140	30	15	$> 10^{11}$

Table 4.1: Critical values of some typical superconductors. The penetration depth λ_L are given at zero temperature, the critical magnetic field and critical (sheet) current density are given at 4.4K. Data collected from Larbalestier *et al.* (2001); Blatter *et al.* (1994); Finnemore *et al.* (1966); Nirrengarten *et al.* (2006) and references therein.

II superconductors transist into the mixed state where the magnetic flux particially penetrates into the superconductors in terms of vortices. These vortices arrange themselves in a regular structure, so called Abrikosov lattice. In an isotroptic Type II superconductor, each vortex looks like a cylindrical tube with a radius Λ_L. In such a tube, supercurrents circulate around a normally conduting core of a size $\sim \xi$ (superconducting coherence length) and decay on a distance about λ_L from the core. The magnetic flux induced by the circulating supercurrents in each tube (vortex) equal to a single flux quantum $\Phi_0 = \pi\hbar/e = 2.07^{-15}\mathrm{T\ m}^2$ (e is the electron charge). In most type II superconductors $\xi < \lambda_L$. If the temperature, the current or the magnetic field become larger than the second critical value, the vortex cores merge and the type II superconductor transits into a normal conductor where the current density becomes uniform in the whole volume. Typically the second critical values are much higher the first ones. We list the critical values of some typical type I superconductors and some type II superconductors which are used in the experiments in Table 4.1. Type II superconductors in the mixed state can freeze a magnetic flux, which makes them different from both the normal metal and the superconductors in the Meissner state. And they produce higher noise than those in the Meissner state.

4.3 Basic equations for SC in the Meissner state

To study the trapping field around a superconductor in the Meissner state, we simplify the structure to two spatial dimensions by assuming invariance along the y direction and we apply the boundary integral method described in Sec.3.3 for superconducting wires also. We focus on the following configuration in this chapter: a pure superconducting wire with a transport current I is placed in an external bias magnetic field $\mathbf{B}_b$. The bias magnetic field is in the xz plane and the transport current flows along the y direction. For a superconducting wire made of niobium at temperature 4.2K, the penetration depth $\lambda_L \sim 40\mathrm{nm}$ is infinite small compared to the thickness of the wire $t \gtrsim 0.8\mu\mathrm{m}$. We make in this chapter the approximation that the supercurrents flow only on the surface of the wire. These surface currents prevent the magnetic field from penetrating the superconducting wire. Thus there is no magentic field inside the superconductor (the meissner effect). Outside the superconductor, the screening

current induced by the bias field $\mathbf{B}_b$ (in the y direction) produces a magnetic field in the xz plane; on the other hand the magnetic field produced by the transport current I lies in the xz plane too, therefore the total magnetic field (the bias field and field generated by the transport current) is in the xz plane and independent on y due to the symmetry. We describe the total magnetic field outside of the wire in terms of a scalar potential ψ and a vector potential $\mathbf{A} = \mathbf{e}_y A$

$$\mathbf{B}(\mathbf{x}) = -\nabla\psi(\mathbf{x}) + \nabla \times \mathbf{A}(\mathbf{x}) \; . \tag{4.1}$$

We shall prove below that the scalar potential ψ describes the field caused by the external field and the vector potential A gives the field caused by the transport current in the superconducting wire.

The magnetic field normal to the superconductor surface is continuous because $\nabla \cdot \mathbf{B} = 0$. The magnetic field inside the superconductor is zero, the normal magnetic field must then vanish on the surface

$$\mathbf{n}(\mathbf{x_s}) \cdot \mathbf{B}(\mathbf{x}_s) = 0 \; , \tag{4.2}$$

where $\mathbf{n}(\mathbf{x}_s)$ is the outward normal at the point $\mathbf{x}_s$ which is on the superconductor surface. Apply Eq.(4.1) in the above equation, we have

$$\begin{aligned} \mathbf{n}(\mathbf{x_s}) \cdot \mathbf{B}(\mathbf{x_s}) &= -\mathbf{n}(\mathbf{x_s}) \cdot \nabla\psi(\mathbf{x}_s) - (\mathbf{n}(\mathbf{x_s}) \times \mathbf{e}_y) \cdot \nabla A(\mathbf{x}_s) \\ &= -\frac{\partial\psi(\mathbf{x}_s)}{\partial n(\mathbf{x}_s)} - \frac{\partial A(\mathbf{x}_s)}{\partial t(\mathbf{x}_s)} = 0 \; , \end{aligned} \tag{4.3}$$

where $\partial/\partial n(\mathbf{x}_s)$ and $\partial/\partial t(\mathbf{x}_s)$ are the normal and tangential derivatives at $\mathbf{x}_s$. (The local tangent vector is $\mathbf{t} = \mathbf{n} \times \mathbf{e}_z$.) We construct the potentials ψ and A such that both terms $\partial\psi_s/\partial n$ and $\partial A_s/\partial t$ in Eq.(4.3) are zero. Note that $\partial A_s/\partial t = 0$ indicates that $A(\mathbf{x}_s)$ is a constant on the surface which we denote by A_0.

Considering that outside the wire, both divergence and curl of the magnetic field are zero, we get

$$\nabla^2\psi(\mathbf{r}) = 0 \qquad \nabla^2 A(\mathbf{r}) = 0 \tag{4.4}$$

where ∇^2 is the two-dimensional Laplace operator and $\mathbf{r}$ is the evaluation point. These Laplace equations can be solved with the help of the Green function

$$G(\mathbf{x}, \mathbf{r}) = -\frac{1}{2\pi} \log|\mathbf{x} - \mathbf{r}| \; , \tag{4.5}$$

where $\mathbf{r}$ is the evaluation point and $\mathbf{x}$ is the source point, given the values of the potentials and their derivatives on the wire surface, and an asymptotic condition at large distance. This Green function is the static analogue of the outgoing wave required by the Sommerfeld radiation condition.

The two potentials behave differently with respect to the current I transported by the superconductor. To see this, recall the Ampère-Maxwell law (in the static limit)

$$I = \int_F \mathrm{d}^2 f(\mathbf{x}) \nabla \times \mathbf{H}(\mathbf{x}) = \oint_S \mathbf{H}(\mathbf{x}) \cdot \mathrm{d}\mathbf{a}(\mathbf{x}) \; , \tag{4.6}$$

where F is an area including the cross-section of the superconducting wire (area element $\mathrm{d}^2 f(\mathbf{x})$), I the total current flowing through F, and S the closed curve bounding F (oriented line element $\mathrm{d}\mathbf{a}(\mathbf{x})$). Inserting Eq.(4.1) in the above equation, we see that

$$\oint_S \nabla\psi \cdot \mathrm{d}\mathbf{a} = 0 \tag{4.7}$$

and

$$I = \oint_S \nabla \times \mathbf{A} \cdot \mathrm{d}\mathbf{a} = -\oint_S \frac{\partial A}{\partial n} \mathrm{d}a \ . \tag{4.8}$$

where $\partial/\partial n$ is the derivative normal to the curve S and pointing 'outside'. Eqs.(4.7) and (4.8) indicate that the current only determines the vector potential $\mathbf{A}$, but does not provide any constraint for the scalar potential. We can thus split the problem in two parts. The scalar potential ψ asymptotically describes the external magnetic field (homogeneous bias $\mathbf{B}_b$). The vector potential is fixed by the imposed supercurrent and asymptotically, it increases at most like $\log|\mathbf{x}|$, providing a magnetic field proportional to $I/|\mathbf{x}|$. Since both potentials satisfy the boundary condition Eq.(4.3) on the wire surface, the full field is given by the sum Eq.(4.1).

In this chapter we only consider superconductors in the Meissner state with thickness much larger than penetration depth (eg. the niobium wire is $1\mu\mathrm{m}$ thick which is much larger than its penetration depth $40\mathrm{nm}$), then the currents are supposed to be only on the surface. The interior of the superconductor is screened from the field by the surface current; while the tangential magnetic field is nonzero at the outer surface of the superconductor. The surface current density is given by (Landau *et al.*, 1984)

$$\mathbf{g}(\mathbf{x_s}) = \frac{\mathbf{n}(\mathbf{x_s}) \times \mathbf{B}(\mathbf{x_s})}{\mu_0} \ , \tag{4.9}$$

where μ_0 is the permeability in the vacuum. In our case $\mathbf{n}$ and $\mathbf{B}$ are both in the xz plane, and the surface current $\mathbf{g}(\mathbf{x_s})$ is obviously along $\mathbf{e_y}$. Apply Eq.(4.1) in the above equation, we get

$$\begin{aligned} \mathbf{g}(\mathbf{x_s}) &= \frac{1}{\mu_0}\left(-\mathbf{n}(\mathbf{x_s}) \times \nabla\psi(\mathbf{x}_s) + \mathbf{n}(\mathbf{x_s}) \times \nabla \times \mathbf{e}_y A(\mathbf{x}_s)\right) \\ &= \frac{1}{\mu_0}\left(\frac{\partial\psi(\mathbf{x}_s)}{\partial t(\mathbf{x}_s)}\mathbf{e}_y - \frac{\partial A(\mathbf{x}_s)}{\partial \mathbf{n}(\mathbf{x_s})}\mathbf{e}_y\right) \ . \end{aligned} \tag{4.10}$$

To be sure that the superconductor is in the Meissner state, the surface current density g should remain below the critical sheet current density J_{c1}, for a type I superconductor, eg. Pb, this value is $4.4 \times 10^4 \mathrm{A/m}$, for a type II superconductor, eg. Nb, this value is $11.14 \times 10^4 \mathrm{A/m}$.

A superconducting wire with a transport current, placed in an external magnetic field is applied to provide a magnetic trap above the wire. Since the scalar and vector potentials (ψ, A) in Eq.(4.1) describe the field produced by the external field and transport current respectively, in the rest of this section we discuss the surface current density and magnetic field generated by the bias field and the transport current respectively first, and then combine them to make a magnetic trap.

4.3.1 Magnetic trap based on SC in the Meissner state

A magnetic trap can be formed by a superconducting wire in the Meissner state carrying a transport current and placed in a bias magnetic field. The trapping field and the current distribution can be computed as the superposition of a current-carrying wire in vacuum and a wire with zero transport current in a nonzero bias field.

4.3.2 Bias field

Let us consider a superconducting wire carrying zero transport current in a bias field $\mathbf{B}_b$. Because of the Meissner effect there will be currents within the London depth λ_L which screen the superconductor from the external field so that the magnetic field inside the superconductor below the London depth is zero. The outside magnetic field (the field created by the screen current and bias field) is described only by

$$\mathbf{B}(\mathbf{x}) = -\nabla\psi(\mathbf{x}) \ . \tag{4.11}$$

The induced surface current is determined by the tangential derivative of $\psi(\mathbf{x}_s)$, the first term in Eq.(4.10)

$$\mathbf{g}(\mathbf{x_s}) = \frac{-\mathbf{n}(\mathbf{x_s}) \times \nabla\psi(\mathbf{x}_s)}{\mu_0} = \frac{\mathbf{e}_y}{\mu_0}\frac{\partial\psi(\mathbf{x}_s)}{\partial t(\mathbf{x}_s)} \ . \tag{4.12}$$

The total current created by the external field can be obtained by integrating the current density on the whole surface

$$\oint \mathbf{e}_y \cdot \mathbf{g}(\mathbf{x_s}) \mathrm{d}a(\mathbf{x}_s) = \frac{1}{\mu_0}\oint_S \frac{\partial\psi(\mathbf{x}_s)}{\partial t(\mathbf{x}_s)} \mathrm{d}a(\mathbf{x}_s) \ , \tag{4.13}$$

where in two spactial dimensions S is the circumference of the wire, and $\mathrm{d}a(\mathbf{x})$ the scalar line element. As the integration of a gradient field over a closed curve is zero, the above integral vanishes. It again proves that the scalar potential ψ has no contribution to the total current.

The solution of Eq.(4.4) for the scalar potential ψ is given in terms of a surface integral equation

$$\begin{aligned} \psi(\mathbf{r}) &= \psi_b(\mathbf{r}) - \oint_S \mathrm{d}a(\mathbf{x}) \left(G(\mathbf{x},\mathbf{r}) \frac{\partial\psi(\mathbf{x})}{\partial n(\mathbf{x})} - \frac{\partial G(\mathbf{x},\mathbf{r})}{\partial n(\mathbf{x})}\psi(\mathbf{x}) \right) \\ &= \psi_b(\mathbf{r}) + \oint_S \mathrm{d}a(\mathbf{x}) \frac{\partial G(\mathbf{x},\mathbf{r})}{\partial n(\mathbf{x})}\psi(\mathbf{x}) \ , \end{aligned} \tag{4.14}$$

where $\mathbf{r}$ is the evaluation point outside the wire, $\partial/\partial n$ the normal derivative points outside the wire, ψ_b the external potential corresponding to the bias field $\psi_b(\mathbf{r}) = -\mathbf{B}_b \cdot \mathbf{r}$. We applied $\partial\psi(\mathbf{x}_s)/\partial n(\mathbf{x}_s) = 0$ (according to Eq.(4.3)) in the last term. Thus $\psi(\mathbf{x})$ on the surface is the only unknown in Eq.(4.14). It can be obtained by letting $\mathbf{r} \to \mathbf{x}_s$, then the singularitiy of the normal derivative of the Green function $\partial G(\mathbf{x},\mathbf{x}_s)/\partial n(\mathbf{x})$ under the integral has been touched. We extract the singularity as discussed in Sec.3.3.2 and get

$$\left(\frac{1}{2} - \frac{\phi(\mathbf{x}_s)}{4\pi}\right)\psi(\mathbf{x}_s) = \psi_b(\mathbf{x}_s) + \mathcal{P}\int_S \mathrm{d}a(\mathbf{x}) \frac{\partial G(\mathbf{x},\mathbf{x}_s)}{\partial n(\mathbf{x})}\psi(\mathbf{x}) \ , \tag{4.15}$$

where $\mathcal{P}\int$ denotes the principal integral and $\phi(\mathbf{x}_s)$ describes the angle subtended by the surface element centered at $\mathbf{x}_s$, it is zero for a flat surface element, but nonzero for a curved one. Eq.(4.15) is self-consistent and fixes $\psi(\mathbf{x}_s)$ and $\mathbf{g}(\mathbf{x}_s)$. $\psi(\mathbf{r})$ can be computed everywhere outside wire with Eq.(4.14), and the total magnetic field can be obtained by Eq.(4.11).

4.3.3 Transport current

Let us now consider a superconducting wire with a transport current I placed in vacuum. The magnetic field outside the wire is described completely by the vector potential $\mathbf{A}$ (the second term of Eq.(4.1))

$$\mathbf{B}(\mathbf{x}) = \nabla \times \mathbf{A}(\mathbf{x}) \ . \tag{4.16}$$

Again due to the Meissner effect the current flows only on the surface. The surface current density is given by the normal derivative of the vector potential on the surface (the second term of Eq.(4.10))

$$\mathbf{g}(\mathbf{x_s}) = -\frac{\mathbf{e}_y}{\mu_0}\frac{\partial A(\mathbf{x}_s)}{\partial n(\mathbf{x}_s)} \ . \tag{4.17}$$

The total current can be computed by integrating the surface current density over the whole surface

$$I\mathbf{e}_y = \frac{\mathbf{e}_y}{\mu_0}\oint\!\!\!\!\!\!\int_S \frac{\partial A(\mathbf{x})}{\partial n(\mathbf{x})}\mathrm{d}a(\mathbf{x}) \ . \tag{4.18}$$

We see again that the transport current I only contributes to the vector potential $\mathbf{A}$, but has no relevance to the scalar potential ψ. Similar to Eq.(4.14), the vector potential outside the wire can be computed with

$$\mathbf{A}(\mathbf{r}) = -\mathbf{e}_y \oint\!\!\!\!\!\!\int_S \mathrm{d}a(\mathbf{x}) \left(G(\mathbf{r},\mathbf{x})\frac{\partial A(\mathbf{x})}{\partial n} - \frac{\partial G(\mathbf{r},\mathbf{x})}{\partial n}A(\mathbf{x}) \right) \ , \tag{4.19}$$

where we can set under the integral $A(\mathbf{x}) = A_0$, constant on the surface according to Eq.(4.3). Other symbols are defined as in Eq.(4.14). Note that the integral of the second term in the bracket vanishes. Again we choose the evaluation point $\mathbf{r}$ to be on the surface and get a self-consistent equation

$$A_0 = -\oint\!\!\!\!\!\!\int_S \mathrm{d}a(\mathbf{x}) \left(G(\mathbf{x},\mathbf{x}_s)\frac{\partial A(\mathbf{x})}{\partial n(\mathbf{x})} \right) \ . \tag{4.20}$$

Note that the singularity of the Green function $G(\mathbf{x}_s,\mathbf{x})$ under the integral has to be taken into account here also. Integrating the Green function over a small surface element $c(\mathbf{x}_s)$ of length σ centered around $\mathbf{x}_s$, we get

$$\int_{c(\mathbf{x}_s)} -\frac{1}{2\pi}\log(|\mathbf{x}_s - \mathbf{x}|)\frac{\partial A}{\partial n}(\mathbf{x})\mathrm{d}a(\mathbf{x}) \approx \frac{\sigma}{2\pi}\frac{\partial A}{\partial n}(\mathbf{x}_s)\left(1 - \log\frac{\sigma}{2}\right) \ . \tag{4.21}$$

We always choose $A_0 = 1$ in Eq.(4.20) at the beginning of the numerical calculation. Eq.(4.20) then fixes $\partial A(\mathbf{x})/\partial n(\mathbf{x})$ and $\mathbf{g}(\mathbf{x}_s)$. We compute the total current by Eq.(4.18) and re-scale $A(\mathbf{x})$ and $\partial A(\mathbf{x})/\partial n(\mathbf{x})$ to get the desired current. Finally the surface current density $\mathbf{g}$, vector potential $\mathbf{A}$ and magnetic field $\mathbf{B}$ outside the wire can be obtained by Eqs.(4.17), (4.19) and (4.16) respectively.

4.4 Trap based on SC cylinder in the Meissner state

A cylindrical superconducting wire with a transport current I is placed in a homogeneous bias field $\mathbf{B}_b$ as shown in Fig. 4.1. The wire is infinite long along the y axis. R denotes the radius of the cylindrical wire, α the angle between the evaluation point $\mathbf{r}$ and the bias field $\mathbf{B}_b$ along the x direction. We calculate first the surface current density and then compute the magnetic field outside the wire by the Biot-Savart law. A quadruple trap can be obtained at $\alpha = \pi/2$ by choosing the bias field such that it cancels the magnetic field created by the transport current there.

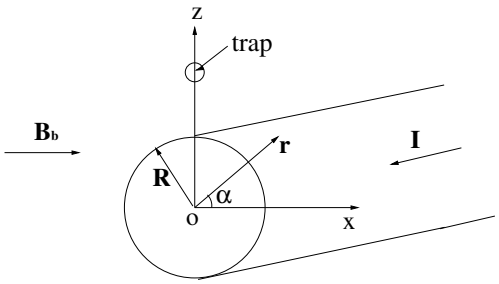

Figure 4.1: A cylindrical superconducting wire carrying a current I is placed in a homogeneous bias field $\mathbf{B}_b$ parallel to the x axis. o is the origin; R the radius of the wire; $\mathbf{r}$ the evaluation point; α the angle between $\mathbf{r}$ and $\mathbf{B}_b$. We consider the superconducting wire in the Meissner state here. A quadrupole magnetic trap can be formed by choosing the bias field such that it cancels the magnetic field created by the transport current above the center ($\alpha = \pi/2$).

4.4.1 Transport current

When there is a transport current I in the cylindrical superconducting wire (see Fig. 4.1), according to the discussion in Sec.4.3, the magnetic field outside the superconductor produced by this current can be described by the vector potential $\mathbf{A}$, which is given by Eq.(4.19). Due to the Meissner effect and the cylindrical symmetry, the surface current density is constant $I/2\pi R$, it should below the critical $J_{c1} = j_{c1}\lambda_L$: for example, a niobium cylinder with $R = 10\mu\mathrm{m}$ at $4.2\mathrm{K}$ in a zero magnetic field, the transport current should not exceed $I_{c1} = 2\pi R J_{c1} = 7.16\mathrm{A}$. While for a normal cylindrical wire with a transport current I, the current density is uniform in the whole volume. The magnetic field around the superconducting and the normal cylinder at the evaluation point $\mathbf{r}$ are both given by

$$\mathbf{B}(I, r) = \frac{\mu_0 I}{2\pi r}\mathbf{e}_\mathbf{r} \ . \tag{4.22}$$

But the magnetic fields outside of superconducting and normal wires with other identical shapes such as rectangle and strip are different. We will see below that the current density is uniform all over the volume in a normal rectangle and strip, but it concentrates at corners of

a superconducting rectangle or the edges of a superconducting strip, which results in different trapping fields at short distances from the superconductors.

We plot the magnetic field produced by the imposed current along the cylindrical superconducting wire in Fig. 4.2 to validate our numerics for a superconducting wire with a transport current.

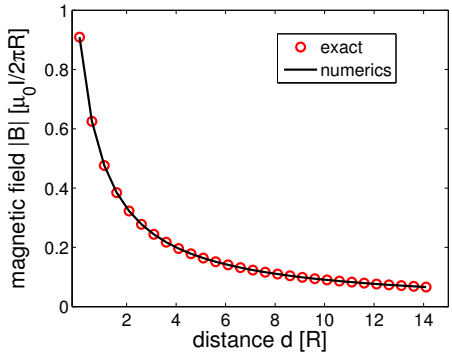

Figure 4.2: Magnetic field $|B|$ created by the transport current in the cylindrical superconducting wire vs distance from the surface. Circles: exact values computed by Eq.(4.22); Solid line: numerical results given by Eqs.(4.16) and (4.19). We normalize the distance by the radius R of the cylinder.

4.4.2 Bias field

Let us consider now the magnetic field and the surface current produced by the bias field $\mathbf{B}_b$. The magnetic field outside the superconductor (the bias field and field produced by the surface current) is described by the scalar potential ψ (see Eq.(4.11)) which satisfies the Laplace equation Eq.(4.4). The magnetic field coincides with the external one $\mathbf{B}_b$ at infinity and its normal component is zero at the boundary of the superconductor. The exact solution of Eq.(4.4) then can be written in polar coordinates

$$\psi(B_b, r, \alpha) = -B_b(r + \frac{R^2}{r}) \cos\alpha \ , \tag{4.23}$$

where $r = |\mathbf{r}| = R + d$, and d is the distance from the surface to the evalution point. The normal component of the magnetic field is

$$B_n(B_b, r, \alpha) = -\frac{\partial\psi}{\partial r} = B_b(1 - \frac{R^2}{r^2}) \cos\alpha \ , \tag{4.24}$$

and the tangential component of the magnetic field is

$$B_t(B_b, r, \alpha) = -\frac{1}{r}\frac{\partial\psi}{\partial\alpha} = B_b(1 + \frac{R^2}{r^2}) \sin\alpha \ . \tag{4.25}$$

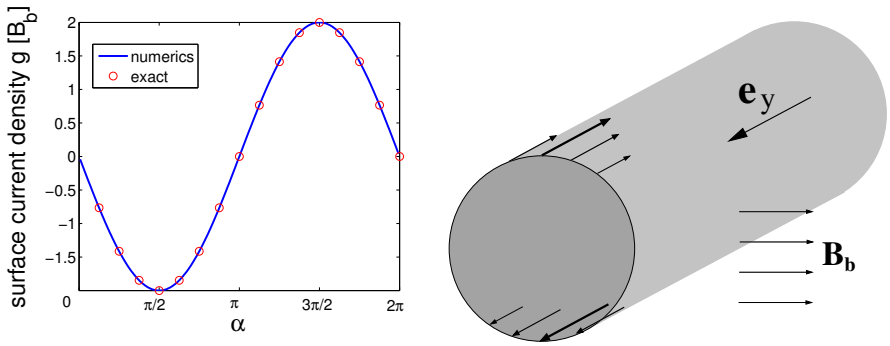

Figure 4.3: Left: current density on the surface of a superconducting cylinder placed in a bias field. Solid line: numerical results computed with Eq.(4.12). Circles: analytical results computed with Eq.(4.25). Right: sketch of the surface current density on the cylindrical wire. The currents are in the opposite directions on the upper half face and the lower half face. The total current is zero.

$g(R,\alpha) = -B_t(B_b, r = R, \alpha)/\mu_0$ is the surface current density caused by the bias field according to Eq.(4.12), which screens the superconductor from the external field. Because the superconductor is in the Meissner state, we require $|g(R)_{max}| = 2B_b/\mu_0 \leq J_{c1}$. For a niobium cylindrical wire at 4.2K, B_b should below $\mu_0 J_{c1}/2 \approx 0.069T$. The surface current density produced by the bias field is plotted in Fig. 4.3(left). It shows that the currents on the upper and lower semicircles are in the opposite directions so that the total current is zero as described by Eq.(4.13).

The magnetic field $|B|$ at $\alpha = \pi/2$ at different distances from the surface is plotted in Fig. 4.4. It can be seen that the magnetic field $|B|$ is significantly larger than the bias field $|B_b|$ at $\alpha = \pi/2$ in the region $d < 3R$, and it then goes to the bias field B_b with increasing d. This is due to the different current distribution compared to the normal cylinder. It is not easy to see the difference between the numerical results with curvature correction and without this correction in Fig. 4.4. In fact, the scale potential A is only proportional to the integral of $\partial G(\mathbf{x}, \mathbf{x}_s)/\partial n(\mathbf{x})$, so the curvature correction significantly improve the convergence of Eq.(4.20), as can be seen in Fig. 4.5.

4.4.3 Magnetic trap

Consider a 'side guide trap' formed by a superconducting cylinder carrying a transport current $I\mathbf{e}_y$ and placed in a bias field $B_b\mathbf{e}_x$. The magnetic field created by the transport current I has only nonzero x-component at $\alpha = pi/2$ (above the center of the wire). Choose the bias field B_b such that the magnetic field generated by it cancles the field at $\alpha = pi/2$ created by the transport current I. A quadruple magnetic trap is then obtained above the center of the cylinder. For example, we choose $B_b = 0.4\mu_0 I/2\pi R$ and plot the modulus of the total magnetic field above the wire in Fig. 4.6. A quadrupole magnetic field can be seen at $\alpha = \pi/2$ near the

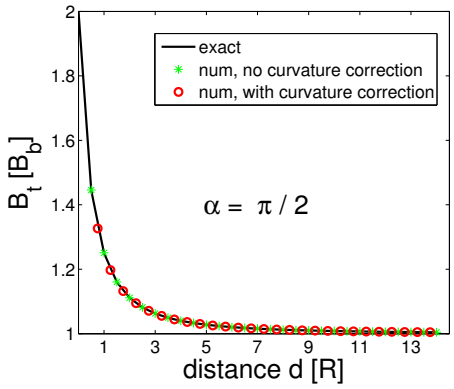

Figure 4.4: Magnetic field B_t normalized by B_b vs distance from the surface d at $\alpha = \pi/2$. Solid line is computed with the exact expression Eq.(4.25); circles are computed with the boundary integral equations with curvature correction Eqs.(4.15) and (4.20); Stars are computed with the boundary integral equations without curvature correction $\phi(\mathbf{x}_s) = 0$; . Our numerical results are in a good agreement with the exact one. The impact of curvature correction is not obvious in this figure, we show the details in Fig. 4.5.

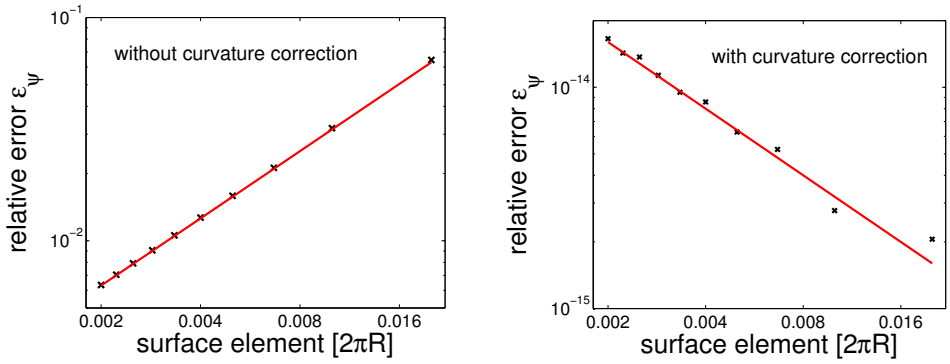

Figure 4.5: Relative error of the scalar potential ϵ_ψ vs the surface elements. ϵ_ψ is defined by replacing A_{num} and A_{ana} in Eq.(3.39) by ψ_{num} (Eq.(4.15) and ψ_{ana} (Eq.(4.23)). (left) ψ_{num} is computed with $\phi(\mathbf{x}_s) = 0$. The error has the magnitude around $\sim 10^{-1}$ and scales as σ (solid line). (right) ψ_{num} is computed by taking into account the nonzero $\phi(\mathbf{x}_s)$. The error is of a magnitude about $\sim 10^{-14}$. It scales also as σ (solid line). This small error is at the level of machine precision. In both figures we discretize the surface into uniform elements.

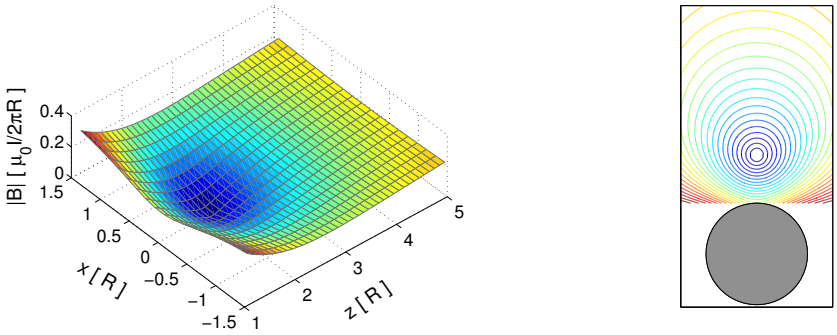

Figure 4.6: Magnetic trap created by a superconducting wire with a transport current I in a bias field $B_b = 0.4\mu_0 I/2\pi R$. We plot the total magnetic field $|B|$ around the superconductor. $|B|$ is computed with Eq.(4.1) and normalized to $\mu_0 I/2\pi R$. We discretize the wire boundary into 300 elements. Left: 3D plot of $|B|$. Right: equipotential lines.

trap height $d \sim R$. We should check that the total surface current density, the current produced by the bias field and the transport current, should remain below the critical values. If the cylinder in Fig. 4.6 is made of niobium and the operating temperature is $4.2\mathrm{K}$, the maximal surface current density caused by the bias field is $2 \times 0.4I/2\pi R$, the surface current density caused by the transport current is $I/2\pi R$. Therefore, the total current density $1.8 \times I/2\pi R$ should not exceed the critical sheet current density $J_{c1} = 11.14 \times 10^4 \mathrm{A/m}$. Then the transport current should not exceed $3.98\mathrm{A}$.

We know that the transport current I creates the same magnetic field outside of the superconducting and normal cylinder. The normal cylinder does not influence the bias field, whereas the superconducting one increases the external field in the region close to the superconductor (see Fig. 4.4). For a normal cylinder with transport current I, the required bias field at trap height d is

$$\text{normal}: \quad B_b(I,r) = \frac{\mu_0 I}{2\pi(d+R)} \,. \tag{4.26}$$

For a superconducting cylinder with transport current I, the required bias field at the trap height d is

$$\text{SC}: \quad B_b(I,r) = \frac{\mu_0 I(d+R)}{2\pi\left((d+R)^2+R^2\right)} \,. \tag{4.27}$$

We plot the required bias field at different trap heights above the superconducting and normal cylinders with identical geometry and transport curent in Fig. 4.7. In the region $d \leq 2.5R$, a superconducting wire needs a smaller bias field than a normal one. When the trap center approaches the surface of the cylinder, a superconducting wire only need one half of the bias field required by a normal one. On the other hand, applying the same bias field, the trap is closer to the superconducting one than the normal one. This is helpful for miniaturization and

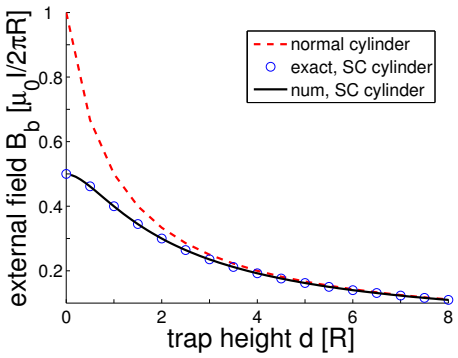

Figure 4.7: External field B_b vs the trap height above a cylindrical wire. Here B_b is normalized by $\mu_0 I/2\pi R$, the trap height d is normalized by the radius R. Dashed line: analytical results for the normal cylinder computed with Eq.(4.26). Circles: analytical results for the superconducting cylinder evaluated with Eq.(4.27). Solid line: numerical results for the superconducting cylinder evaluated with Eqs.(4.14) and (4.19). We apply 300 surface elements in the numerics.

integration with other devices as mentioned in chap.1. It is another advantage of superconducting atom chips compared to normal ones.

4.5 Trap based on SC rectangle and strip in the Meissner state

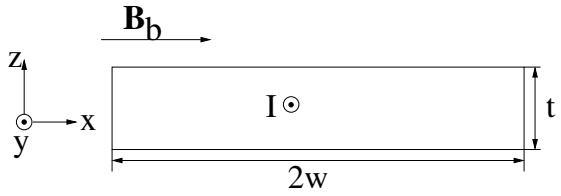

Figure 4.8: A superconducting rectangular wire is carrying a current I and placed in a bias magnetic field $\mathbf{B}_b$. The wire is infinitely long along the y axis, and has a width $2w$ along x and a thickness t along z. If t is much smaller than the width $2w$ and the distance between the trap center and the top surface of the wire denoted by d, we do not taken into account the finite thickness and the side faces, the rectangule transits into a strip (infinite thin rectangle). The current flows along the y axis, while the bias field $\mathbf{B}_b$ lies in the xz plane. A quadrupole trap can be created above the wire center by choosing the transport current and the bias field such that the fields generated by the transport current and the bias field cancel each other above the wire center.

In this section we focus on a 'side guide' trap realized by a superconducting rectangle or strip which are the usual shape for lithographically fabricated atom chips. Here, a strip

means an infinite thin rectangle ($t \ll 2w$) without side faces. The wire is carrying a current I and placed in a horizontal bias field $\mathbf{B}_b$ as shown in Fig. 4.8. We assume that the wire is in the Meissner state and its thickness t and width $2w$ are much larger than the London penetration depth λ_L. We will see that properties and parameters of the magnetic trap formed by a superconducting rectangular wire are different from those of the magnetic trap formed by a superconducting cylindrical wire or a normal conductor one due to the different surface current distributions.

4.5.1 Side guide trap

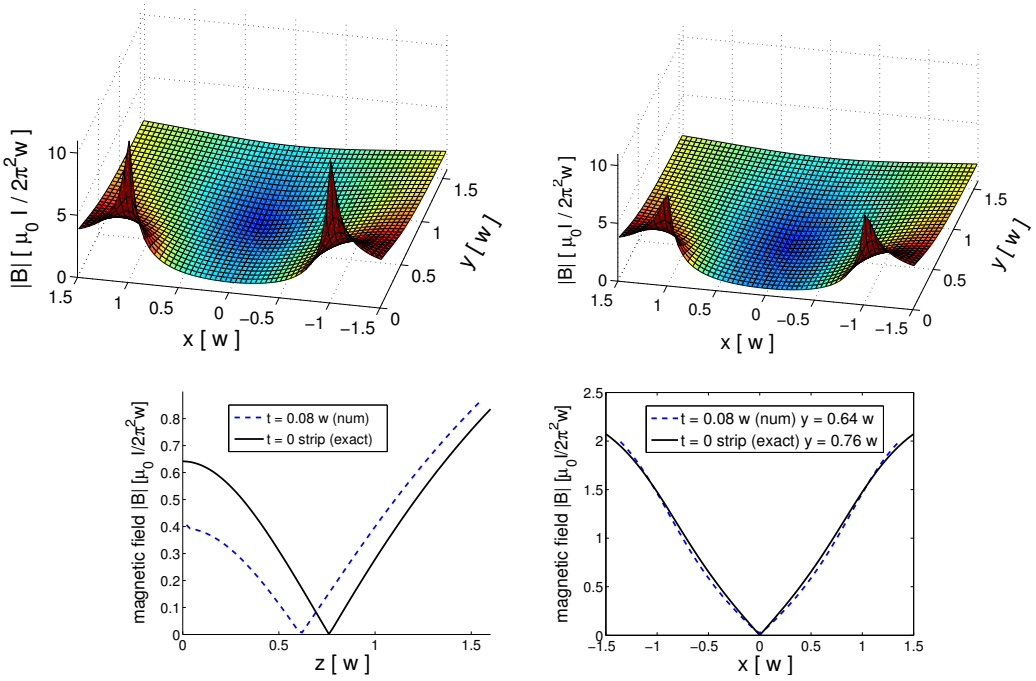

Figure 4.9: (top) Magnetic trap ("side guide") created by a superconducting rectangular wire with a transport current, placed in a bias field parallel to the wire surface. We plot the modulus of the magnetic field, normalized to $\mu_0 I/(2\pi^2 w)$. (left) infinite thin rectangular wire (strip, analytical calculation); (right) rectangular wire considering the finite thickness and side faces (numerical calculation). (bottom) cross-sections along the z axis and x axis through the trap centre. Solid lines: analytical result for a strip in the sheet current approximation; dotted lines: numerical calculation for a rectangle. Due to the finite thickness and the side faces, the trap is shifted closer to the wire (distance $0.76\,w \rightarrow 0.64\,w$).
The bias field is $B_b = -2.5\mu_0 I/(2\pi^2 w)$. The numerical calculations are for a thickness $t = 0.081\,w$, with screening currents flowing along all wire surfaces. The corners of the wire are rounded (radius $0.031\,w$). Only data points with distances larger than $0.031\,w$ are plotted in the top row.

A magnetic trap can be formed by a superconducting rectangular wire or a superconducting strip carrying a transport current I and placed in a bias field along the x axis as shown in Fig. 4.9, details of calculations for supercurrents and fields in superconducting wires are given in Sec.4.6. In the adiabatic approximation, a low-field-seeking atom is confined in the minimum of the modulus of the total field $|B|$, which we plot in Fig. 4.9. By symmetry, the minimum modulus of the total field lies above the center of the wire, where the parallel bias field is canceled by the field created by the transport current I. The field above a strip center generated by a transport current is parallel to the x axis and can be obtained by applying Bio-Savart law (Brandt & Indenbom, 1993)

$$\text{SC}: \quad B(I, x = 0, z) = \frac{\mu_0 I}{2\pi(w^2 + z^2)^{1/2}} \; . \tag{4.28}$$

In order to compare with the field above a normal strip, let us recall that the current distribution in a normal strip is uniform and the Biot-Savart law leads to (Reichel, 2002)

$$\text{normal}: \quad B(I, x = 0, z) = \frac{\mu_0 I}{2\pi w} \arctan \frac{w}{z} \; . \tag{4.29}$$

The magnetic fields created by the transport current above the center of a superconducting strip and a normal one as well as the fields above superconducting rectangular wires with two thickness/width ratios are shown in Fig. 4.10(left). Recall that the magnetic fields created by transport currents outside of a superconducting cylinder and a normal cylinder are exactly the same as shown in Fig. 4.2, although the current distribution is uniform in the whole volume inside the normal one wheares there is no current inside and the current is only uniform on the surface od the superconducting cylinder. But the magnetic field and current distribution generated by a transport current around a superconducting rectangular wire and a normal conducting rectangular wire are completely different. Fig. 4.10(left) shows that the field caused by a transport current above the superconducting strip is lower than that above a normal one at short height due to the different current distribution. The current diverges at the edges of the superconducting wires (see Sec.4.6). This is different from the cylindrical case. It also can be seen from Fig. 4.10(left) that at short height the infinite thickness and the side faces make the fields above a rectangle center a littel lower than that above a strip with the same width.

By adding a homogeneous bias field parallel to the x axis such that the external field (including the bias field and the field generated by the screening currents) $B(B_b, 0, d) = B(I, 0, d)$, then a quadrupole magnetic trap is formed above the center at distance d. The required bias fields at different d are shown in Fig. 4.10(right). We see that the required bias field for a superconducting strip is smaller than for a normal one by a factor $2/\pi$ at low trap height $d \leq 2.5w$. Or we can say that the superconducting strip traps the atoms closer to the surface than a normal strip in the same bias field. This results from the different current distrobution. Due to the finite thickness and the side faces, the required bias field above a superconducting rectangle is even smaller than above a superconducting strip. At larger trap height, all wires behave practically the same.

Figs. 4.9 and 4.10 together illustrate the impact of the finite thickness and the side faces of the superconducting wire. The horizontal bias field also induces screening currents on the side

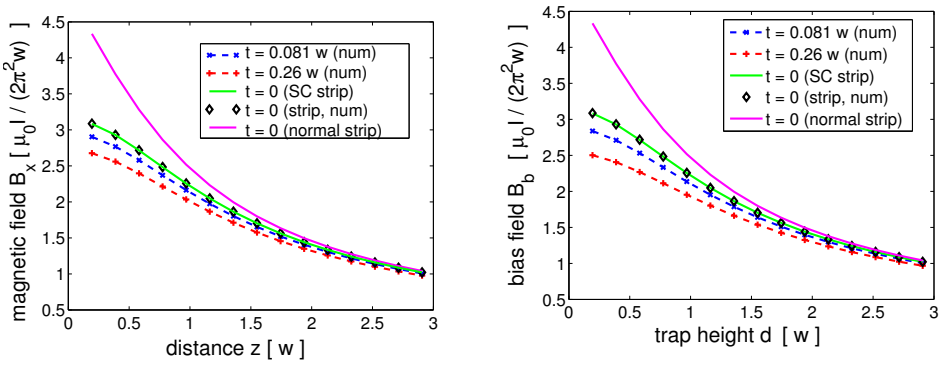

Figure 4.10: (left) Magnetic field created by a current-carrying wire as a function of the normalized obsrevation distance z/w. Solid line: superconducting strip; dashed line: normal metal strip; symbols: superconducting rectangular wires with different thickness. The magnetic field is normalized to $\mu_0 I/(2\pi^2 w)$. (right) Bias field required to form a trap at height d above the wire. This plot differs from the left one only for rectangular wires where screening currents appear on all surface. The trap height is slightly reduced. Field and distances are normalized as in (left).

faces of the wire which makes the currents on the top and bottom faces in different directions (see Sec.4.6 below). The effect is so small that the field gradient along the x axis at the trap center is almost unchanged (see Fig. 4.9 bottom right). The main impact of superconductor is to make the trap-surface distance shorter at fixed bias field, see Fig. 4.9. Conversely, superconducting wires lower the bias field required to create a trap at small height as shown in Fig. 4.10(right).

geometry	$I_{c1}(J_{c1} \times \mu\mathrm{m})$ for $B_b = 0$	$B'_{c1}(B_{c1})$ for $I = 0$
cylindrical wire	64.27	0.49
rectangular wire	10.81	$0.44/0.07(\mathrm{horizontal/vertical})$
strip	5.39	large (horizontal) < 0.07 (vertical)

Table 4.2: Critical values for niobium wires. The critical sheet current density is $J_{c1} = 11.14 \times 10^4 \mathrm{A/m}$, the critical field is $B_{c1} = 1400\mathrm{G}$ and the penetration depth is $\lambda_L = 39\mathrm{nm}$ for niobium. The critical transport current is given in units of $J_{c1} \cdot \mu\mathrm{m}$ and the critical field in units of B_{c1}. The results are evaluated for a cylindrical wire with radius $10\mu\mathrm{m}$, a rectangular wire $20\mu\mathrm{m} \times 2\mu\mathrm{m}$ and a strip with width $20\mu\mathrm{m}$ and thickness $t > 2\lambda_L$. For the cylindrical wire, we give the critical magnetic field in arbitrary direction; for the rectangle, the critical values for a horizontal and vertical bias field are given respectively. A strip has no effect on a horizontal bias field. Details about the computations of critical values are given in Sec.4.7.

One should be careful that in order to keep the superconducting wire in the Meissner state,

the total magnetic field including the bias field, the field created by the transport current and the field created by the induced screening currents should remain below the first critical magnetic field B_{c1} in any point of the wire. Otherwise, the superconductor may transit into the normal state (type I superconductors eg. Pb) or the mixed state (type II supercondcutors eg. Nb). We list some typically critical values for Nb wires in Table 4.2, details are given in Sec.4.7.

4.5.2 Transport of atoms

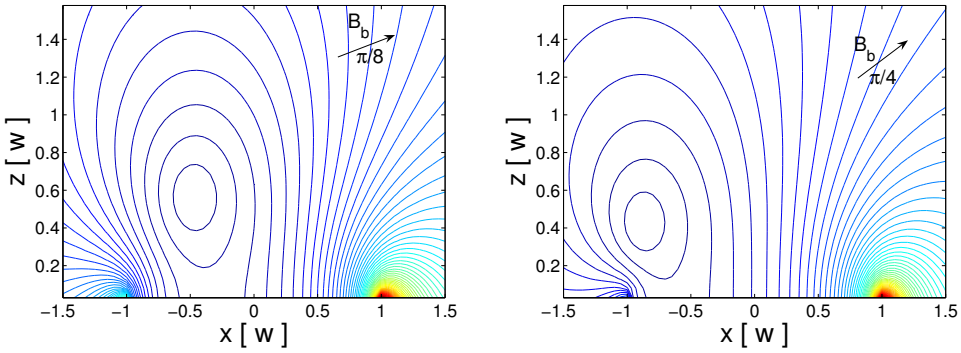

Figure 4.11: Magnetic trap shifted to the edge of the rectangular wire by turning the bias field in Fig. 4.9 in the xz-plane. The wire is carrying a current I. The bias field is $B_b = -2.5\mu_0 I/(2\pi^2 w)$. The wire is $t = 0.08\,w$ thick. The corners of the wire are rounded (radius $0.031\,w$). Only data points with distances larger than $0.031\,w$ are plotted in left. We discretize the surface into 424 elements in the numerical calculation. Left: $22.5°$ angle between the bias field and the x axis. Right: $45°$ angle between the bias field and the x axis.

A simple transport procedure of an atom cloud above a superconducting chip is shown in Fig. 4.11. A superconducting rectangular wire is carrying a transport current I. Applying a bias field with the amplitude $B_b = -2.5\mu_0 I/(2\pi^2 w)$ and changing the angle between the bias field and the x axis (as well as turning the bias field in Fig. 4.9), the minimum of the total field is shifted, hence the atoms are moved along a curve path. Fig. 4.11 shows the field profiles at two different angles of the bias field. When the angle between the bias field and the x axis changes from zero to $45°$, the trap center is moved curvely from the center close to the edge of the wire. One should be careful that the screening currents induced by the external field produce potential barriers near the edges of the wire which should be taken into account for the loading and controlling of the atoms. For this reason, the loading procedure for a superconducting atom chip is quite different compared to a normal one. In the experiments the loading procedure of atom chips transports an atom cloud along the x axis by adjusting the bias field and the transport current. A varying vertical bias field B_y is often used to load atoms on a normal atom chip. However, the impact of the field on the screening current distribution is strongest when the external field is perpendicular to the superconducting wire. The induced screening currents shield the interior of the superconductor from the external vertical field and

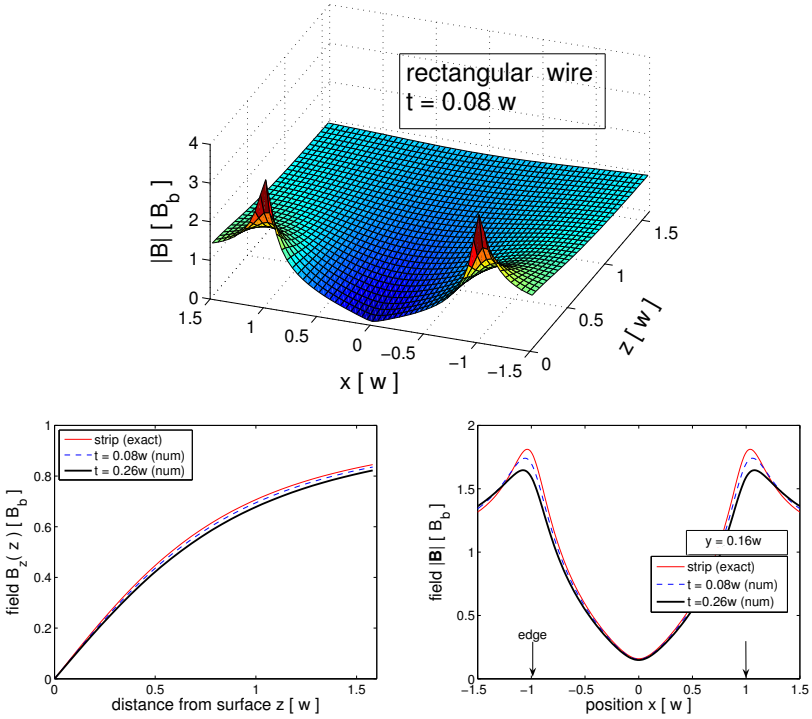

Figure 4.12: Magnetic potential above superconducting wires placed in a vertical bias field. We plot the modulus $|\mathbf{B}(x,z)|$ normalized to the bias field B_b.
(top) Field distribution above a rectangular wire, numerical calculation. A strip wire (infinitely thin rectangle) gives slightly sharper peaks at the wire edges $x = \pm w$.
(bottom left) Field above the wire centre, as a function of distance from the top surface. The difference between an strip (infinitely thin) and wires (finite thickness) is minor. Sheet currents that flow on the wire surfaces (preferentially near the edges) screen the bias field so that the field normal to the wire goes to zero at the surface.
(bottom right) Field at fixed distance $z = 0.16\,w$ from the wire top surface, as a function of lateral position. The peaks are broadened for a rectangular wire.
Analytical results: infinitely thin strip in the sheet current approximation (see Brandt & Indenbom (1993) for details). Numerical calculations: rectangular wire with rounded corners (radius of curvature $0.031\,w$). Only data points with distances larger than $0.031\,w$ from the top surface are included in the top plot.

make the external field significantly non-uniform. This effect get maximal for supercondcutors in the Meissner state. Consequently, different loading procedure is required to be designed for a superconducting atom chip. For example, if the transport current and the horizontal bias field are fixed, we need carefully vary the vertical field nonlinearly so that the atom cloud can be loaded along the x axis.

To show the influence of the screening currents on the external field, we plot the magnetic field distribution above a superconducting rectangle placed in a vertical bias field in Fig. 4.12. There are two maxima around the edges and one minimum above the center on the surface, since the screening currents preferentially flow along the edges. Around the top corners the fields close to the surface are much larger than the applied bias field (see Fig. 4.12 bottom right), at the center the field goes to zero on the surface (see Fig. 4.12 bottom left). It can also be seen that increasing the thickness of the wire broadens the two peaks around the edges (see Fig. 4.12 bottom right), but has less impact on the field above the wire center (see Fig. 4.12 bottom left). The effect of the screening currents decreases as the distance from the surface increasing. As can be seen in Fig. 4.12 (bottom left), the effect of the screening currents is only 15% of the applied bias field at the height $d = 1.5w$. In general, an atom cloud is formed and loaded into a magnetic trap at the height of $300 \sim 500\mu\mathrm{m}$ (Fortágh *et al.*, 2002). This height is about $1.5w$ of usual design wires with width less than $200\mu\mathrm{m}$. Therefore the screening currents influence the loading procedure slightly.

4.5.3 Trap parameters

As shown in the above that a side guide trap can be realized by an atom chips based on superconductors. The non-uniform current distribution and the nonzero screening currents induced by the bias field make the trapping field near a superconducting chip much different from that near a normal one. The transport current concentrates at the edges of the wire (we will show it in the next sections), which makes the current density in the central part of a superconductiong wire smaller and the magnetic field near the wire center weaker than that near a normal one at the same total current. Recall that a superconducting strip has no effect on a parallel bias field, a side guide trap is closer to the surface of a superconducting strip than to the surface of a normal one (at fixed horizontal field). The finite thickness and the side faces of the superconducting wire slightly decrease the bias field above the wire center and bring the trap even closer to the top surface of a superconducting rectangular wire (Fig. 4.10).

Before we consider trap parameters of the side guide traps created by a superconducting wire, we point out that we do not take into account here the bending of the wires such as 'U' and 'Z' traps and only conside a side guide trap generated by a current-carrying superconducting wire in an external bias field. Calculation of the current density distributionthe in a bent superconducting wire is complicated, it requires to solve the integral equations in Sec.4.3 in three spatial dimensions and take care of the concentration of currents at each sharp corner. However, our results can be applied at the central part of the guiding wire, where is sufficiently far away from the bends.

The confinement of atoms in a magnetic trap is described by the two parameters: the magnetic field gradient at the trap center and the depth of the trapping potential. The trap depth is determined by the smaller one of the two potential barriers: one is from the trap center to the

surface and the other is from the trap cenetr to far away. The gravitational potential is taken into account for the trap depth. For a fair comparison, the superconducting and normal strips have the identical geometry; the superconducting rectangle has the same width $10\mu\mathrm{m}$ as the strips; the superconducting strip and rectangle are both made of niobium and applied at $4.2\mu\mathrm{K}$; three wires carry the same transport current $20\mathrm{mA}$.

The field gradients and the trap depthes at different distances are presented in Fig. 4.13. At larger trap height ($d > 2w = 10\mu\mathrm{m}$), the field gradient and the trap depth for the three geometries are essentially the same. At small trap height, the superconducting traps have obviously smaller field gradient and trap depth than the normal one. The parameters of the trap formed by the superconductng rectangle are slightly smaller than the superconducting strip due to the impact of the finite thickness and side faces. A reliable trapping of the atoms having temperature of $1\mu\mathrm{K}$ can be obtained when the trap depth is larger than $10\mu\mathrm{K}$ (the dashed line in Fig. 4.13right) and the gradient is high enough to avoid the atoms loss by the gravitational effect, for example $15.3G/\mathrm{cm}$ (the dashed line in Fig. 4.13left) for ^{87}Rb atoms in the $|F = 2, m_f = 2\rangle$ state (F is the total spin and m_F magnetic moment). This reliable trapping range of the traps formed by niobium superconducting wires can be roughly estimated from Fig. 4.13 $1 \sim 100\mu\mathrm{m}$. It is obviously samller than the trapping range of a normal trap. Although compared to a normal chip trap, a superconducting one has a smaller trapping range and worse trap parameters at low height $d < 6\mu\mathrm{m}$, it is still attractive due to the significant reduction of the magnetic noise, which prolong the trap lifetime and coherence.

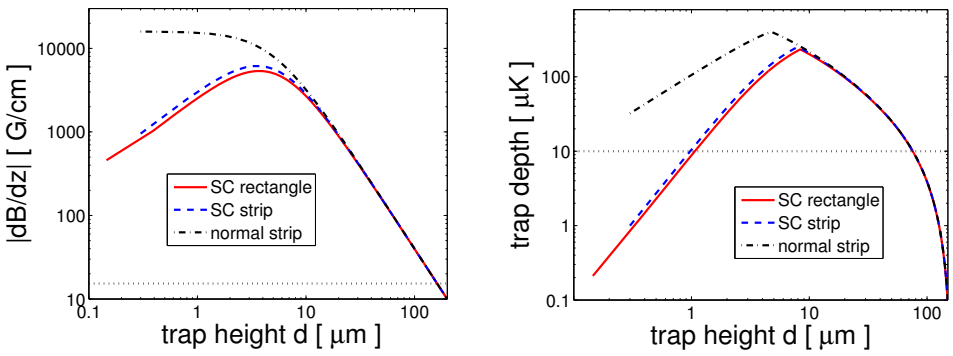

Figure 4.13: Magnetic field gradient (left) and trap depth (right). Black dash-dot lines: normal strip. Blue dahsed lines: superconducting strip. Red solid lines: superconducting rectangle. Dot lines: typical criteria for reliable trapping, $15.3G/\mathrm{cm}$ for the magnetic field gradient in the left and $10\mu\mathrm{K}$ for the trap depth in the right. The three wires are all $10\mu\mathrm{m}$ wide and carrying $20\mathrm{mA}$ transport current. The rectangular wire is $0.86\mu\mathrm{m}$ thick. The superconducting wires are made of niobium and applied at $4.2\mu\mathrm{K}$. The trap depth is corrected by taking into account the gravitational effect.

4.5.4 Noise

The motion of the electrons that are not in the superconducting state and participate in thermally induced current fluctuations is the main source of the magnetic noise. Recently, the magnetic noise has been investigated by means of two-fluid model, Bardeen-Cooper-Schrieffer (BCS) theory and Eliashberg theory. Compared to normal metallic chips, the magnetic noise is significantly reduced by several orders of magnitude around a superconducting chip in the Meissner state. This is benift from the opening of the superconducting gap and the resulting inability to deposit energy into the superconductor, the highly efficient screening properties and the small active volume within which current fluctuations can contribute to the noise (Scheel *et al.*, 2005; Skagerstam *et al.*, 2006; Hohenester *et al.*, 2007; Rekdal & Skagerstam, 2007; Skagerstam & Rekdal, 2007). However, the magnetic noise can not yet be detected by any superconducting quantum interference devices (SQUID) or other measurement devices.

4.6 Field and current distribution in the Meissner state

It is well known that in a normal conductor the current density is homogeneous in the whole volume. However, this is quite different in a superconducting wire due to the Meissner effect. In the following, we discuss the current density distribution in a superconducting wire by means of the surface integral equations and conformal mapping respectively. Once the current density distribution is determined, the megnetic field near the superconducting wire can be obtained by applying the Biot-Savart law.

4.6.1 Numerical calculation

Let us first consider the magnetic field and screening currents created by a transport current I. For a superconducting rectangle they are still described by Eq.(4.17[1] and 4.19) and shown in Fig. 4.14. The current distributions are the same on the upper and lower surface by symmetry and concentrate in the four corners with the same direction and amplitude (see Fig. 4.14 left). In Fig. 4.14(right), the magnetic field above the wire shows two maxima around the corners and a 2D minimum in the middle at short distance ($z \leq w$); in the far field the magnetic field becomes 'azimuthal' with respect to the rectangle, and the superconducting wire behaves as a normal metallic one.

For a strip (see Fig. 4.15) the integral equations can be simplified and the current density can be replaced by a sheet current density. Recall the second term in Eq.(4.19), it can be written as

$$\frac{\partial G(\mathbf{r},\mathbf{x})}{\partial n(\mathbf{x})} = \mathbf{n}(\mathbf{x}) \cdot \mathbf{s} \frac{\mathrm{d}G(s)}{\mathrm{d}s} \frac{1}{s} \,, \tag{4.30}$$

where $\mathbf{s} = \mathbf{r} - \mathbf{x}$ and $s = |\mathbf{s}|$ which is the distance beween the evaluation point $\mathbf{r}$ and source point $\mathbf{x}$ as shown in Fig. 4.15. Because the strip is infinite thin, the source points $\mathbf{x}$ and $\mathbf{x}'$ on the top and bottom surfaces have the same coordinates and the same distances from the evaluation point, but the normal vectors at $\mathbf{x}$ and $\mathbf{x}'$ have opposite signs. The integrals of Eq.(4.30) on the

[1] We round the edges of the wire with a radius of curvature $r \approx w/32$, for the sake of faster convergence.

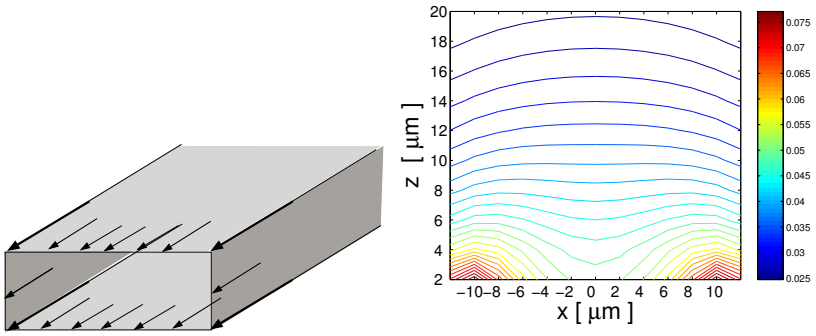

Figure 4.14: Superconducting rectangularwire with a transport current. Left: illustration of the surface current distribution. The supercurrent flows preferentially along the wire corners. Right: equipotential lines of the magnetic field $|\mathbf{B}|$ above the wire, which is $2w = 20.64\mu\mathrm{m}$ wide and $t = 1.64\mu\mathrm{m}$ thick. We take the transport current $I = 1\mathrm{A}$ and $|B|$ is in unit of T. The corners are smoothed with a radius of curvature $r = 0.32\mu\mathrm{m}$. We discretize the boundary into 424 elements.

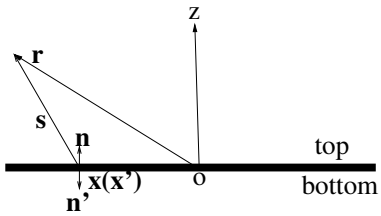

Figure 4.15: Sketch of a superconductor strip. The top and bottom surfaces coincide each other. $\mathbf{x}(\mathbf{x}')$ is the source point on the top(bottom) surface. $\mathbf{n}(\mathbf{n}')$ is the unit normal vector at $\mathbf{x}(\mathbf{x}')$. o is the origin.

top and bottom surfaces have opposite sign and cancel each other in Eq.(4.19). We have used here that, similar to a superconducting rectangular wire with a transport current, the surface current density distributions on the top and bottom surfaces are exactly the same by symmetry. We write $g'(\mathbf{x}) = \partial A'_s(\mathbf{x})/\partial n$ to denote the sum of current densities on the top and bottom at point $\mathbf{x}$, and get from Eq.(4.19) the integral equation of Bancroft (1996)

$$A_0 = -\int_{-w}^{w} \mathrm{d}a(\mathbf{x}) \left(G(\mathbf{r}, \mathbf{x}) g'(\mathbf{x}) \right) \ , \tag{4.31}$$

where A_0 is the constant value of the vector potential on the strip surface.

We plot the sheet current density $g'(\mathbf{x})$ in Fig. 4.16. The current, as well as the current in the superconducting rectangle, diverges at the edges of the strip. For comparison, we include the analytic results (circles computed by Brandt's model which is discussed in the following section) in Fig. 4.16 also. Good agreement between the numerics and the analytics effectively

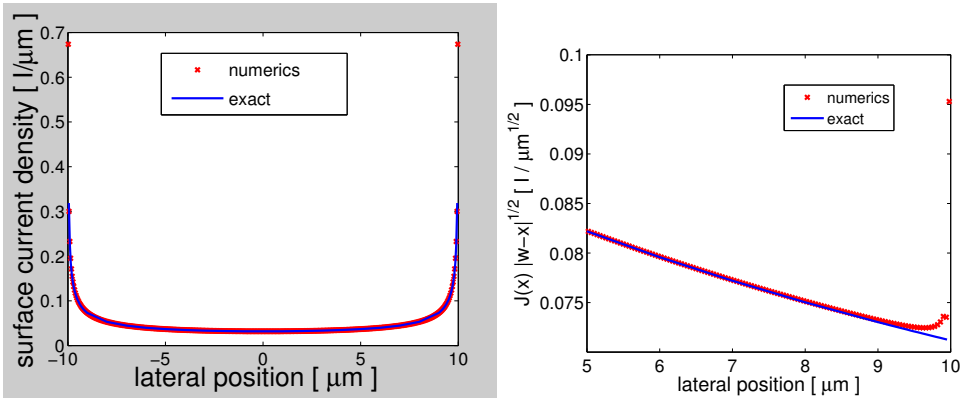

Figure 4.16: Left: current density distribution on a superconducting strip with a transport current. The strip is 20μm wide. Solid line: computed numerically with Eq.(4.31); Circles: computed with Eq.(4.38). We discretize the strip surface into 200 surface elements. Both numerical and analytical results show the divergence of the current at the edges. Right: sheet current density diverges near the edge as $\sqrt{|w-x|}$.

.

validates our numerical approach. Once we know the sheet current density $g'(\mathbf{x})$ on the strip, the magnetic field can be evaluated everywhere by Eq.(4.16).

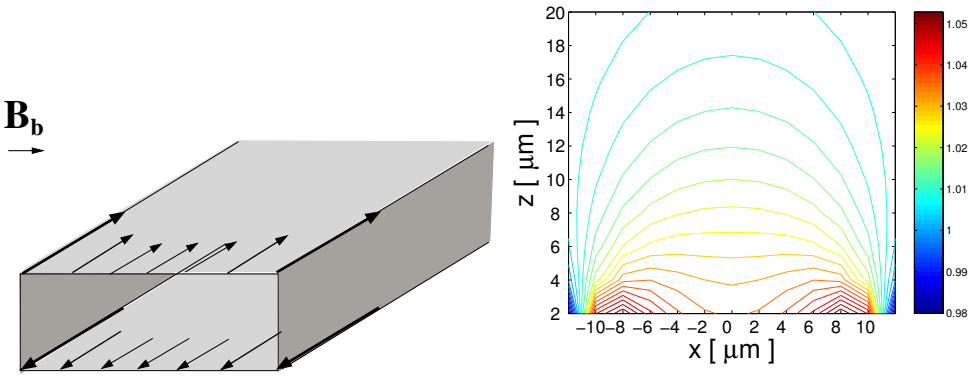

Figure 4.17: Superconducting rectangular wire placed in a horizontal bias field $\mathbf{B}_b$. Left: illustration of the surface current distribution. The bias field induces screening currents on the side faces of the rectangle and makes the currents on the top and bottom sides differ. Right: equipotential lines of the magnetic field $|\mathbf{B}|$ (bias field plus field produced by the screening current) above the wire. $|\mathbf{B}|$ is normalized to b_b. The rectangular wire is $2w = 20.64\mu$m wide and $t = 1.64\mu$m thick. The corners are smoothed with a radius of curvature $r = 0.32\mu$m. We discretize the boundary into 424 elements.

Let us now consider screening currents induced by a horizontal bias field and how they react on the external field. The density distribution of the induced screening current is described by Eq.(4.12) and shown in Fig. 4.17 (left). The currents concentrate on the four corners: the currents on the two upper corners flow in the positive direction of the y axis while the currents on the two lower corners flow in the opposite direction. It is the induced screening currents on the side faces of the rectangle that make the currents on the top and bottom sides differ. The magnetic field above the superconducting wire (ie. bias field plus field generated by the screening current) is described by Eq.(4.14) and presented in Fig. 4.17 (right). At short distances ($z \leq w$), there are two maxima at the two upper corners. In the far field, the magnetic field coincides with the bias field, and the impact of the screening current rapidly becomes negligible because the total screening current is zero.

For a superconducting strip in a horizontal bias field, the thickness is so small that there is no induced screening current inside the strip and the strip does not change the bias field.

4.6.2 Conformal mapping

Brandt's model

Brandt & Mikitik (2000a) investigate the surface current distribution in a superconducting rectangle in the Meissner state by means of a conformal mapping of the rectangle onto a half plane. A superconducting wire carrying a current I and placed in a bias field B_b can be computed as a linear superimposition of the two cases (as mentioned before): a wire with a nonzero current in a zero bias field ($I \neq 0,\ B_b = 0$) and a wire with zero current in a nonzero bias field ($I = 0,\ B_b \neq 0$). Generally, if the bias field B_b forms an angle with the top surface of the wire, we decompose it into two components parallel and perpendicular to the top surface and estimate the current density and fields induced by these two components seperately. We recall some basic formulas here.

In Brandt's model, a universal mapping function is defined as

$$f(s,m) = ms \int_0^1 \frac{\sqrt{1-s^2\zeta^2}}{\sqrt{1-ms^2\zeta^2}} \mathrm{d}\zeta \ , \tag{4.32}$$

that can be evaluated as a sum of two incomplete elliptic integrals $f(s,m) = E(s,m) - (1-m)F(s,m)$, with $0 \leq |s|, m \leq 1$:

$$F(s,m) = \int_0^s \frac{1-\zeta^2}{\sqrt{1-m\zeta^2}} \mathrm{d}\zeta \tag{4.33}$$

is the incomplete elliptic integral of the first kind, and

$$E(s,m) = \int_0^s \sqrt{\frac{1-m\zeta^2}{1-\zeta^2}} \mathrm{d}\zeta \tag{4.34}$$

is the incomplete elliptic integral of the second kind, see Abramowitz & Stegun (1972). m is determined by the ratio of the thickness to the width of the rectangle

$$\frac{t}{2w} = \frac{f(1,m)}{f(1,1-m)} \ . \tag{4.35}$$

For the rectangle with fixed ratio $2w/t$ (then m is fixed) carrying a current I and placed in a zero bias field, the surface current $J(x,z)$ has the parametric form

$$J(x,t/2) = \frac{I}{2\pi w}\frac{f(1,1-m)}{\sqrt{(1-m)(1-s^2)}}\,, \quad \frac{x(s)}{w} = \frac{f(s,1-m)}{f(1,1-m)} \quad 0<|s|<1\,, \tag{4.36}$$

$$J(w,z) = \frac{I}{\pi t}\frac{f(1,m)}{\sqrt{m(1-s^2)}}\,, \quad \frac{2z(s)}{t} = \frac{f(s,m)}{f(1,m)} \quad 0<|s|<1\,. \tag{4.37}$$

We plot the surface current density induced by the transport current and described by the above two equations in Fig. 4.18(left), The current density diverges at the corners, but this singularity is integrable.

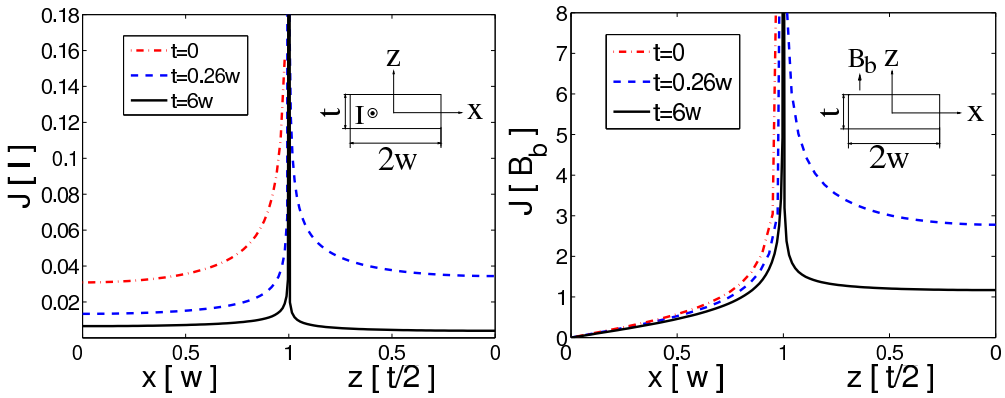

Figure 4.18: Surface Current density distribution induced by a transport current (left) and a bias field (right) on a strip and rectangles with different aspect ratios. Left half: top surface $x=0...w,\ z=t/2$; right half: side aurface $z=t/2...0,\ x=w$, see insert. Red (dot-dashed) line: strip. Blue (dashed) line: a rectangle with thickness $t=0.26w$. Black (solid) line: a rectangle with thickness $t=6w$.

In the limit $t \ll 2w$, m tends to zero and as shown by Brandt & Mikitik (2000a), Eq.(4.36) yields

$$J(x,0) = \frac{I}{2\pi(w^2-x^2)^{1/2}}\,. \tag{4.38}$$

Taking into account both the top and bottom surfaces of the wire, $2J(x,0)$ gives back the exact sheet current density for a strip given in Brandt & Indenbom (1993); Zeldov *et al.* (1994). We plot Eq.(4.38) in Fig. 4.16 and Fig. 4.18(left). The current distribution on a wire can be described by the sheet current density as long as the thickness is much smaller than the width, see Fig. 4.18(left).

Similarly, for a rectangle with fixed ratio $t/2w$ carrying a zero current and placed in a

vertical field B_b, the surface current $J(x,z)$ is

$$J(x,t/2) = \frac{B_b}{\mu_0}\frac{s}{\sqrt{1-s^2}}\,, \quad \frac{x(s)}{w} = \frac{f(s,1-m)}{f(1,1-m)}\,,\ 0<|s|<1\,, \tag{4.39}$$

$$J(w,z) = \frac{B_b}{\mu_0}\frac{\sqrt{1-ms^2}}{\sqrt{m(1-s^2)}}\,, \quad \frac{2z(s)}{t} = \frac{f(s,m)}{f(1,m)}\,,\ 0<|s|<1\,. \tag{4.40}$$

The current distribution in a strip which is placed in a vertical field can be obtained by taking the limit $t \ll 2w$ in Eq.(4.39), see (Brandt & Mikitik, 2000a):

$$J(x,0) = \frac{xB_b}{\mu_0\sqrt{w^2-x^2}} \tag{4.41}$$

Again considering both the top and bottom surfaces, we can use $2J(x,0)$ as sheet current density for a strip. From the above equation, one finds that the currents in the left and right halves of the top surface are in opposite directions. We plot the current density distribution on rectangles with different thickness/width ratios and a strip which are placed in a bias field perpendicular to their top surfaces in Fig. 4.18(right). It can be seen again that the current diverges at the corner, but this singularity is integrable. For example, integrating the current density Eq.(4.41) over the half width of a strip, one gets a current $I_{half} = 2wB_b/\mu_0$.

Zhilichev's model

In order to avoid the divergence of the fields at the corners, Zhilichev (2003) rounded the sharp corners by arcs. This approach will be used in Sec.4.7 to estimate critical currents and fields. Let us first consider a semi-infinite superconducting film with rounded corners and placed in a horizontal bias field, as shown in Fig. 4.19(left). The film is infinite along the y axis and the positive x axis and it has thickness t along the z axis. The bias field B_b is parallel to the x axis. We round the corners with a curvature of ρ, which is normalized by $t/2$. By symmetry, we only compute the upper half part of the film by conformally mapping it onto the upper half-plane (Zhilichev, 2003), as shown in Fig. 4.19(right).

The mapping function between the p and w planes (map $w \to p$) is (Zhilichev, 2003)

$$\begin{aligned} p &= C\int \frac{\sqrt{w}+\gamma\sqrt{w+\beta}}{\sqrt{w+1}}\mathrm{d}w \\ &= C\Big\{\gamma\left[\sqrt{(w+1)(w+\beta)} - (1-\beta)\ln\left(\sqrt{w+1}+\sqrt{w+\beta}\right)\right] \\ &\quad -\gamma\left[\sqrt{\beta} - (1-\beta)\ln\left(1+\sqrt{\beta}\right)\right] + \sqrt{w(w+1)} - \ln\left(\sqrt{w+1}+\sqrt{w}\right)\Big\}\,. \end{aligned} \tag{4.42}$$

The points $a_2(w=-1)$, $a_1(w=-\beta)$ and 0 on the w-plane are mapped to the points $A_2(p=-\rho-i)$, $A_1(p=-\rho-i\rho)$ and 0 on the p-plane, respectively. $w=u, u\geq -1$ corresponds to the surface of the upper half of the film, from A_2 to the rounded corner, and then to the flat

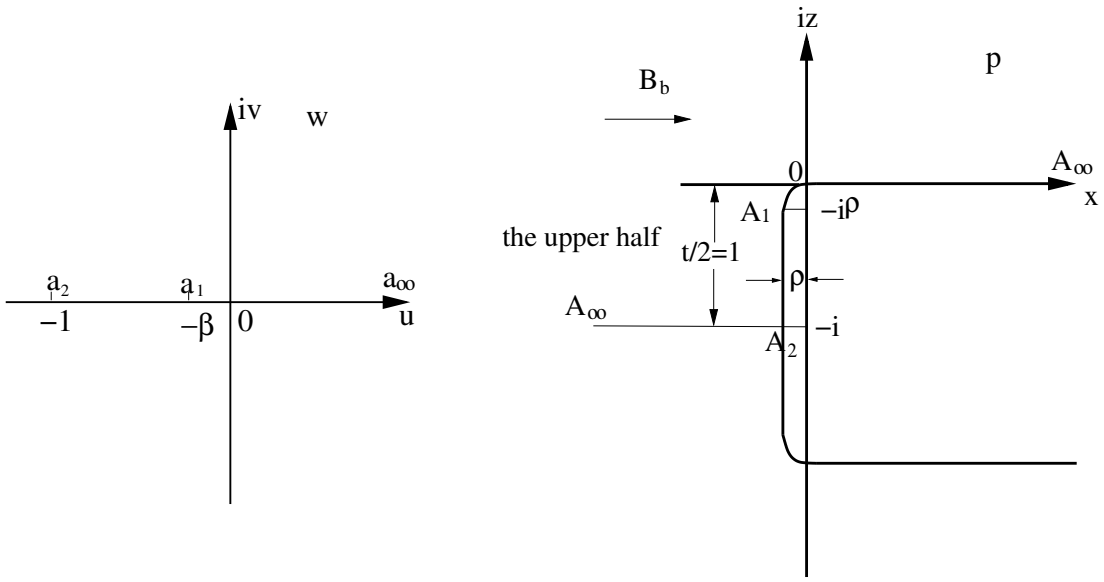

Figure 4.19: Conformal mapping between the upper half-plane ($w = u + \mathrm{i}v$) and the upper half of a semi-infinite film with rounded corners ($p = x + \mathrm{i}z$).

surface, see Fig. 4.19. When β is sufficient small, the following approximations can be used (Zhilichev, 2003)

$$\gamma \approx 1 + \frac{1}{10}\left(\frac{3\pi\rho}{2}\right)^{2/3}, \quad C \approx \frac{2}{\pi\left(2 - 0.9(1.5\pi\rho)^{2/3}\right)}, \quad \beta \approx \left(\frac{3\pi\rho}{2}\right)^{2/3}. \tag{4.43}$$

The field on the surface of the upper half of the superconducting film in the p-plane is given by

$$B = (1+\gamma)B_b\left|\frac{\sqrt{1+u}}{\sqrt{u}+\gamma\sqrt{u+\beta}}\right|, \qquad u \geq -1\,. \tag{4.44}$$

The field B_ρ on the rounded corner ($-\beta \leq u \leq 0$) can be obtained from the above equation

$$B_\rho \approx B_b\left(\frac{16}{3\pi\rho}\right)^{1/3}, \quad \beta \ll 1\,, \tag{4.45}$$

B_ρ is approximately constant and remains finite, unless $\rho \to 0$ (sharp corner). Note that the rounded corner is not exactly one quarter of a circle, its shape is described by Eq.(4.42) with $-\beta \leq u \leq 0$. For example, taking $B_b = 0.181[B_{c1}]$ and $\rho = 0.01$, we plot the exact shape of the rounded corner defined by Eq.(4.42) in Fig. 4.20(left). It shows that the corner is sandwiched between arcs of radius 0.01 and 0.011. The field on the surface of the upper half film is plotted in Fig. 4.20(right). The field behaves similarily to the surface current in Fig. 4.18 described by the Brandt's model, but here the field does not diverge near the corner, see the insert of Fig. 4.20. The maximal field on the corner is finite and can be even lowered by increasing ρ.

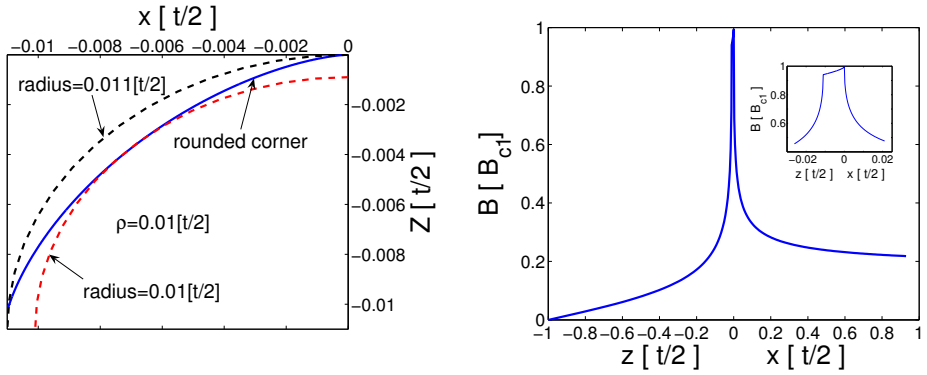

Figure 4.20: Left: the corner shape for rounding parameter $\rho = 0.01[t/2]$. Blue solid line: exact shape of the rounded corner defined by Eq.(4.42) with $\beta \approx 0.13$ (Eq.(4.43)). It is sandwiched by two quarter circles of radius 0.01 and 0.011 (dashed lines). Right: field on the surface of the upper half film. Insert: field around the corner. As can be seen, the magnetic field gets the maximal value ($B = B_{c1}$) at ($x = 0, z = 0$). x and z are all given in units of $t/2$, and the horizontal bias field $B_b = 0.181$ and the field B on the surface are both given in units of B_{c1}.

For a superconducting rectangle, the width along the x axis is finite and denoted again by $2w$. Compared to the semi-infinite film above, the field on the rounded corner of the rectangle B_ρ^{rect} is given by multiplying Eq.(4.45) with a correction factor (Zhilichev, 2001)

$$B_\rho^{rect} = B_b \left(\frac{16}{3\pi\rho_{rect}}\right)^{1/3} \sqrt{\frac{E(1,m') - F(1,m')}{E(1,m') - mF(1,m')}} \,. \tag{4.46}$$

where $E(1,m')$ and $F(1,m')$ are complete elliptic integrals of the first and second kind and defined by Eqs.(4.33) and (4.34), corresponding to the complementary parameter $m' = 1 - m$, where m is fixed by the aspect ratio of the superconducting rectangle, see Eq.(4.35). Here ρ_{rect} is also normalized by $t/2$. Returning ρ_{rect} into Eq.(4.42), the exact shape of the rounded corners can be obtained.

4.7 Critical values

We have already listed some typical critical values for superconductors with planar boundaries, such as bulk or film, in Table 4.1, and approximate critical values for finite size wires in Table 4.2. The critical values of a superconducting cylinder have been discussed in Sec.4.4. On superconducting atom chips, superconducting wires always have the form of rectangle. Transitions from the Meissner state into normal or the mixed state in a superconducting rectangular

wire become more involved and are much different from transitions in a superconducting cylinder or bulk due to the diverging current near sharp corners. Transitions in a superconducting rectangle happen in several steps dependent on geometry, transport current and bias field. The estimation of critical currents and bias fields is challenging for superconducting rectangular wires and we discuss approximate treatments here.

In Sec.4.6, we have investigated the field and the current density distribution around superconducting rectangles under the assumption that the thickness is much larger than the penetration depth and that there are only currents on the surface of the wires (sheet current approximation). Near sharp corners the sheet currents show strong divergence, but in actual experiments the currents, even near sharp corners, should be finite. This can be obtained in two ways: on the one hand, Zhilichev (2003) regularized the current density near a sharp corner by rounding the corner with arcs, see Fig. 4.20. On the other hand, one can use the full London theory that takes into account the finite penetration depth below the surface and gives a finite current density at sharp corners (Brandt & Mikitik, 2000a). In the following, we roughly estimate the first critical bias field B'_{c1} and transport current I'_{c1} for superconducting rectangles in the Meissner state in the framework of Brandt's model and Zhilichev's model.

4.7.1 Brandt's model

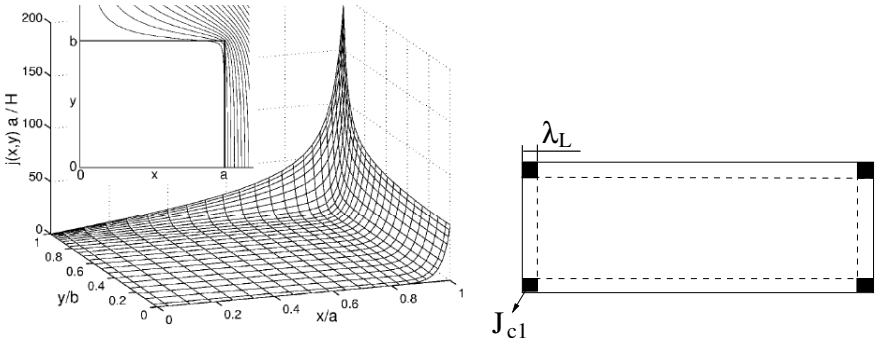

Figure 4.21: Left: The current density induced by a bias field in a superconducting square ($a = b$). $\lambda_L = 0.025a$, $2a$ is the width and $2b$ is the thickness. The bias field $B_b = \mu_0 H$ is vertical to the face along the x axis. The current density $j(x, y)$ is in unit of H/a. Only a quarter of the cross section is shown, by symmetry. The current density shows a sharp, but finite peak in the corner. Insert: magnetic field lines. From Brandt & Mikitik (2000a). Right: qualitative picture: the sheet current density takes its critical value over a region of size λ_L near the sharp corner.

Taking into account the finite penetration depth λ_L, the London equation is used to describe the exactly current and field distribution around a superconductor of arbitrary cross section (London & London, 1935),

$$\lambda_L^2 \nabla^2 \mathbf{B}(\mathbf{x}) = \mathbf{B}(\mathbf{x}) \ , \tag{4.47}$$

where $\mathbf{B}$ is the total magnetic field, $\mathbf{x}$ is the evaluation point. Brandt & Mikitik (2000a) investigated superconducting rectangles in the Meissner state by solving the full London equation, Eq.(4.47), numerically. They found a finite current density at the sharp corners of rectangles, as shown in Fig. 4.21(left). However, no analytical formulas can be obtained directly from the London equation (Eq.(4.47)) for rectangular superconductors. We therefore estimate the critical values for a superconducting rectangle still under the sheet current density approximation, but taking into account the finite value at the sharp corner. The sheet current density diverges as $l^{-1/3}$ at the corners of a rectangle symmetrically, where l is the distance from the corner. As we know that the field and current penetrate into the superconductors in the Meissner state on a scale λ_L, we construct a critical situation by smoothing the current density near the sharp corners on a scale λ_L and setting the maximum current density to the first critical value $J_{c1} = \lambda_L j_{c1}$ of the superconducting material (Fig. 4.21, right).

Nonzero transport current and zero external field

Let us consider a superconducting rectangle carrying a transport current. In this section, we always consider that the thickness t and width $2w$ are larger than $2\lambda_L$. Using conformal mapping techniques, it has been shown that the current density near the sharp corner diverges approximately as $l^{-1/3}$ (Brandt & Mikitik, 2000a)

$$J_{corner}(w, l, I) = \frac{I}{2\pi w}\left(\frac{f(1,m)^2}{3\sqrt{m(1-m)}}\frac{w}{l}\right)^{1/3}, \tag{4.48}$$

where I is the transport current, $f(1,m)$ is defined by Eq.(4.32) and m is fixed by the aspect ratio of the rectangle, Eq.(4.35). We smooth the current density on a scale λ_L and in order to keep the rectangle in the Meissner state we assume $J_{corner}(w, \lambda_L, I'_{c1}) = J_{c1}$ (see Fig. 4.21, right), This gives as approximate critical current for the wire:

$$I'_{c1}(w, \lambda_L, J_{c1}) \approx 2\pi w J_{c1}\left(\frac{f(1,m)^2}{3\sqrt{m(1-m)}}\frac{w}{\lambda_L}\right)^{-1/3}. \tag{4.49}$$

We plot the first critical current I'_{c1} as a function of the width in Fig. 4.22(left), where m is changing with $2w/t$. I'_{c1} increases as the width of the rectangle at fixed λ_L, since the rectangle can carry larger transport currents.

If we ignore the effect of the side faces and consider a width much larger than the thickness, the rectangle can be treated as a strip. But here we should take into account the finite thickness of the strip for the critical current and field. Then the current density induced by the transport current is defined by Eq.(4.38) and diverges at the edges. We smooth the current density near the edges on the scale λ_L, as we did for the current density near sharp corners of a rectangle. Therefore, the currents in the regions of scale λ_L near the two edges are $4\lambda_L J_{c1}$, considering both the top and bottom surfaces. We assume when the transport current increases to the critical value I'_{c1}, the sheet current density at $x = \pm(w - \lambda_L)$ takes its critical value J_{c1}. We then find out the sheet current density distribution between $x = -(w - \lambda_L)$ and $x = (w - \lambda_L)$, it is

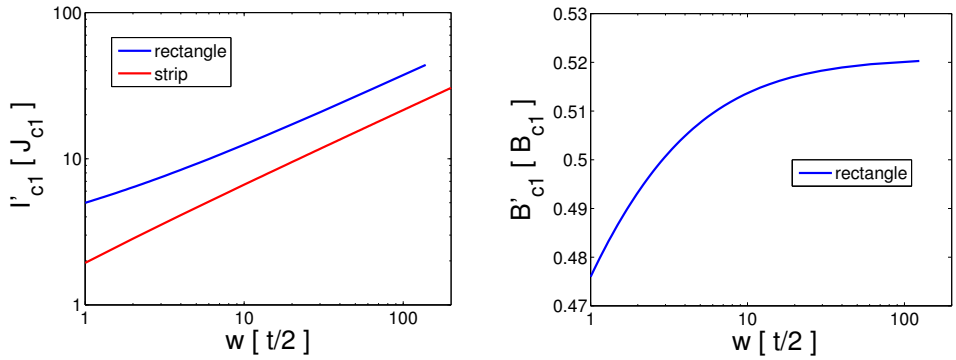

Figure 4.22: Left: the first critical current I'_{c1} vs. the width w of a rectangle and a strip. I'_{c1} are computed by Eq.(4.49) for a rectangle and by Eq.(4.51) for a strip, and given in units of $J_{c1}t/2$. Right: the first critical bias field B'_{c1} (parallel to the surface with the width of $2w$) vs. the width w. B'_{c1} are computed by Eq.(4.53) (rectangle) and given in units of B_{c1} (critical value of the material). In both figures, $\lambda_L = 0.06[t/2]$. Blue lines: rectangle, red line: strip. Because a horizontal bias field has no effect on a strip, we only plot the critical transport current for a strip in the left. For the rectangle, both I'_{c1} and B'_{c1} depend on the aspect ratio and the penetration depth λ_L. While for a strip, they depend on the width and the penetration depth.

integrable:

$$J(x) = \frac{J_{c1}\sqrt{2w\lambda_L}}{\sqrt{w^2 - x^2}} , \quad |x| \leq w - \lambda_L . \tag{4.50}$$

The first critical current for a strip can be approximated by taking the sum of the currents near the edges and the current in the central part from $x = -(w - \lambda_L)$ to $x = (w - \lambda_L)$. Taking into account both the top and bottom surfaces, one has

$$\begin{aligned} I'_{c1} &= 4\lambda_L J_{c1} + 4\int_0^{w-\lambda_L} \frac{J_{c1}\sqrt{2w\lambda_L}}{\sqrt{w^2 - x^2}} \mathrm{d}x \\ &= 2J_{c1}(\pi\sqrt{2w\lambda_L} - 2\lambda_L) . \end{aligned} \tag{4.51}$$

The integral in the above equation is larger than the first term $4\lambda_L J_{c1}$. This means that although the current density takes its maximum near the sharp corners, the main contribution to the total current is from the central part of the surfaces. Eq.(4.51) shows that the first critical current I'_{c1} of a strip increases as its width w at fixed penetration depth λ_L, this also can be seen in Fig. 4.22(left). Note that Eq.(4.38) and (4.51) are only correct when the width is much larger than the thickness ($w \gg t \gg 2\lambda_L$).

For example, consider a superconducting rectangle made of niobium and applied at $4.2\mathrm{K}$ in a zero bias field. The penetration depth of niobium is $\lambda = 39\mathrm{nm}$ and the critical sheet current density is $J_{c1} = 11.14 \times 10^4 \mathrm{A/m}$. If $t = 2\mu\mathrm{m}$ and $w = 10\mu\mathrm{m}$, the transport current I should be less than $I'_{c1} = 1.2\mathrm{A}$ to keep it in the Meissner state (from Eq.(4.49)). For a niobium strip (no side face effects) with the same width, this critical value is $I'_{c1} = 0.636\mathrm{A}$ (from Eq.(4.51)).

Nonzero bias field and zero transport current

Similarly to a superconducting rectangle carrying currents in vacuum, the screening currents induced by a bias field parallel to the width $2w$ of a superconducting rectangle also diverge at the corners as $l^{-1/3}$ (Brandt & Mikitik, 2000a)

$$J_{corner}(w,l,B_b) = \frac{B_b}{\mu_0}\left(\frac{1-m}{3\sqrt{m}f(1,m)}\frac{w}{l}\right)^{1/3}, \tag{4.52}$$

where B_b is the parallel bias field. Again, we smooth the current density on a scale λ_L and in order to keep the rectangle in the Meissner state, we assume $J_{corner}(w,\lambda_L,B'_{c1}) = J_{c1}$. This gives the first critical bias field

$$B'_{c1}(w,\lambda_L,J_{c1}) \approx B_{c1}\left(\frac{1-m}{3\sqrt{m}f(1,m)}\frac{w}{\lambda_L}\right)^{-1/3}. \tag{4.53}$$

We plot the first critical field B'_{c1} in Fig. 4.22(right). B'_{c1} increases with the aspect ratio $2w/t$ of the rectangle at a fixed ratio λ_L/w, while it also increasees as λ_L/w at fixed aspect ratio $2w/t$. In the region where the aspect ratio is much larger than 1, B'_{c1} is the critical value for the bias field parallel to the wider surface of the rectangle (a flat rectangle in parallel field); in the opposite region, B'_{c1} is the critical value for the bias field vertical to the wider surface (a flat rectangle in vertical field).

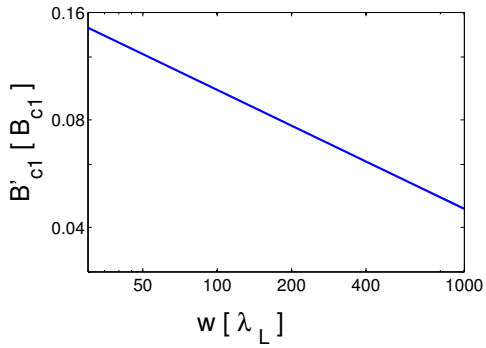

Figure 4.23: The first critical vertical bias field B'_{c1} vs. the ratio w/λ_L for a rectangle. B'_{c1} is computed with Eq.(4.53) and given in units of B_{c1} (critical value of the material). It depends on the ratio w/λ_L at fixed $2w/t$. Here we take a fixed aspect ratio $2w/t = 10$.

4.7.2 Zhilichev's model

Within the frame of Zhilichev's model, the sharp corner is rounded by parameter ρ and defined by Eq.(4.42). The magnetic field takes its maximum at the rounded corner (Fig. 4.20, right) and scales as $(1/\rho)^{1/3}$, see Eq.(4.46). In order to keep the rectangle in the Meissner state, this

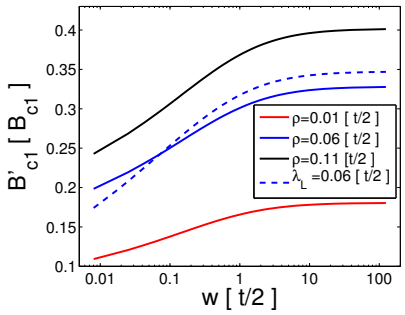

Figure 4.24: The first critical parallel field B'_{c1} for a superconducting rectangle. Red line: the rounding parameter is $\rho = 0.01$; Blue line: $\rho = 0.06$; Black line: $\rho = 0.11$. Blue dashed line: computed by Brandt's model, Eq.(4.53) and taking $\lambda_L = 0.06$. At fixed ρ, B'_{c1} increases as the aspect ratio $2w/t$ and saturates when $2w/t \geq 10$; at fixed aspect ratio, B'_{c1} increases as the rounding parameter ρ. B'_{c1} is in units of B_{c1}, ρ, λ_L and w are all in units of $t/2$.

maximum should be below the first critical value B_{c1} for superconducting bulk or film listed in Table 4.1. The bias field which induces a field on the rounded corner equal to B_{c1}, as the first critical field for the superconducting rectangle, and denote it by B'_{c1}. According to Eq.(3.40),

$$B'_{c1} = B_{c1}\frac{16}{3\pi\rho}^{1/3}\sqrt{\frac{E(1,m')-F(1,m')}{E(1,m')-mF(1,m')}}\,. \tag{4.54}$$

The first critical field B'_{c1} at different rounding parameters ρ are plotted in Fig. 4.24 as a function of aspect ratio $2w/t$ (or $w[t/2]$). At fixed ρ, B'_{c1} increases as the aspect ratio is inreasing and tends to a constant when $2w/t \geq 10$. While at fixed aspect ratio, the larger the rounding parameter ρ is, the higher the critical B'_{c1} is. For comparison, we include the critical values computed by Brandt's model, Eq.(4.53) in Fig. 4.24 (blue dashed line), and modify the data by a prefactor $2/3$ because Brandt's model slightly overestimates the current density near the sharp corners. To make a fair comparison, we take a penetration depth $\lambda_L = 0.06t/2$ in Eq.(4.53), identical to the rounding parameter $\rho = 0.06t/2$ in Zhilichev's model Eq.(4.46) (blue solid line in Fig. 4.24). The blue dashed line computed by Brandt's model and the blue solid line computed by Zhilichev's model in Fig. 4.24 are very close. This suggest that when we use Zhilichev's model to regularize the current density at a sharp corner, we may choose the rounding parameter $\rho \approx \lambda_L$. And this also implies that the magnetic field and the current may penetrate into a superconductor in the Meissner state in a shell of depth λ_L near a sharp corner. Both Brandt's and Zhilichev's models predict that the current density near a sharp corner diverges as $l^{-1/3}$, where l is the distance from the corner.

4.7.3 Bean's model

Fig. 4.25 illustrates how the magnetic field penetrates into a superconducting rectangle elliptically based in Bean's model (Bean, 1962; Norris, 1970; Brandt & Mikitik, 2000). When

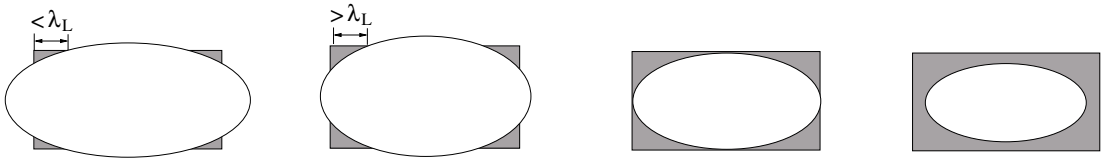

(a) Meissner state (b) intermediate state (c) critical state (d) mixed state

Figure 4.25: Magnetic field penetrates into a superconducting rectangle elliptcally—-Bean's model. The white spaces are field free region; the shades are filed with currents and fields. (a) the Meissner state. The currents distribute within the scale λ_L^2. (b) an intermedia state. As the transport current increases, the current density at corner exceeds its critical value. The magnetic flux penetrates into the rectangle at the corner. The rectanlge partially transits into a mixed state near the corner. (c) a critical state. The ellipse touches the rectangle, the spaces between the ellipse and the rectangle are full filed with the magnetic flux. (d) the pure mixed state.

the current and the bias field are both below the first critical values, the ellipse in which the magnetic field is completely expelled is larger than the rectangle and the currents mainly concentrate in the four corners on a scale smaller than λ_L, see Fig. 4.25(a). If the current or the magnetic field exceeds the first critical value in a type II superconductor, the magnetic flux would penetrate into the superconductor, especially at the corners first, in the form of vortices and the superconductor partially transits into the mixed state. The current at the corner then extends over a scale larger than λ_L, as shown in Fig. 4.25(b). It is an intermediate state where some parts of the superconductor display the properties of the mixed state while some parts of the superconductor are still kept in the Meissner state. Bean (1962) assume that the mixed parts carry a spatially constant current density j_{c2} (niobium, $5^{10}\mathrm{A}/\mathrm{m}^2$). If the current or the bias field continues increasing, more and more magnetic flux penetrates into the rectangle and the ellipse keeps decreasing. When the ellipse touches the boundary of the rectangle as shown in Fig. 4.25(c), the shaded part is entirely filled with the current density j_{c2}, the total current is denoted by $I_c' = 2j_{c2}wt(1-\pi/4)$. For a niobium rectangle with a width of $w = 10\mu\mathrm{m}$ and a thickness of $t = 2\mu\mathrm{m}$, this distinguish current is $I_c' = 0.43\mathrm{A}$. When the current is larger than I_c', the ellipse is smaller than the rectangle (see Fig. 4.25(d)) and the superconductor is in the mixed state. This state can be described by the Bean-Brandt model that we discuss in the following section.

4.8 Trap based on SC strip in the mixed state

In the mixed (or Shubnikov) state, the supercurrent distribution differs from the Meissner state because magnetic flux partically enters into the wire. Qualitatively, a behavior intermediate between a SC in the meissner state and a normal conductor is found, as is discussed in Sec.4.8.2. We start with a brief comparison of the side guide trap.

4.8.1 Side guide trap

A side guide trap can be formed by a strip in the mixed state carrying a transport current I and placed in a bias field B_b. If the bias field is parallel to the wide surface of the strip (along the x axis), the trap is above the strip center by symmetry. We plot the trapping potentials above three strips in Fig. 4.26(right), one is a normal strip (red solid line), one strip is in the mixed state (black dashed line) and the other one is in the Meissner state with current $I = 0.5I_{c2}$ (green dot-dash line). The magnitude of the horizontal bias field is taken as $2.5\mu_0 I/2\pi^2 w$. The trap formed by a strip in the mixed state is between the traps formed by a normal strip and by a strip in the Meissner state. Inceasing the current I, the parameters of a trap formed by a strip in the mixed state are coming closer to those of a trap made by a normal one, whereas decreasing the current makes the parameters come closer to those of a trap made by a strip in the Meissner state.

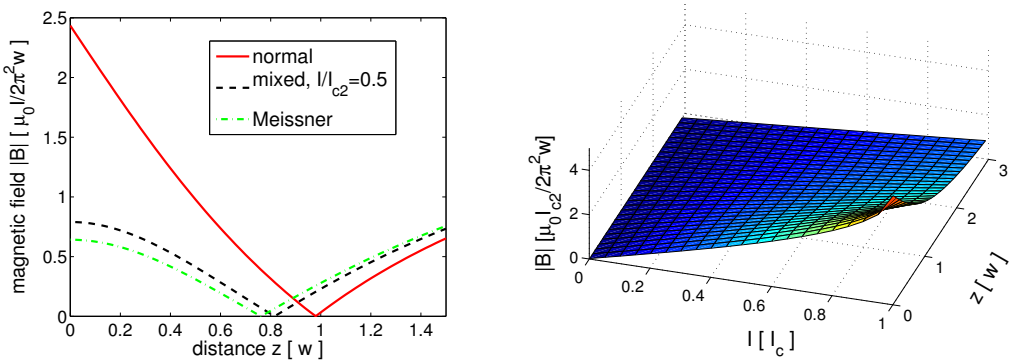

Figure 4.26: Left: magnetic field above the strip center at different current ratio I/I_{c2}. There is no bias field. The field get the maximum value $\mu_0 I/2\pi^2 w$ at the surface when $I = I_{c2}$. At fixed distance z, the magnetic field increases nonlinearly as the current ratio. Right: magnetic potential vs distance z above the strip center. The horizontal bias field is $-2.5\mu_0 I/2\pi^2 w$. Red solid line: potential above a normal strip, computed with Eq.(4.29). Black dashed line: potential above a strip in the mixed state carrying current $I = 0.5I_{c2}$, computed based on the sheet current distribution defined by Eq.(4.55). Green dot-dashed line: potential above a strip in the Meissner state, computed with Eq.(4.28). The minima of the three curves denote the trap positions. The trap above the strip in the Meissner state is closest to the surface, while the trap above a normal strip is furthest away.

We plot the magnetic field above the strip center which is created by the transport current at different ratios I/I_{c2} in Fig. 4.26(left). As can be seen, the magnetic field increases nonlinearly with the current. This is different from both a normal strip and a strip in the Meissner state. The nonlinearity is result from the fact that the shape of the current distribution depends on the ratio I/I_{c2}, see Fig. 4.27 (computed by Eq.(4.55) below). When $I < 0.2I_{c2}$, the nonlinearity is negligible and the currents are mainly flowing near the edges, as for in a strip in the Meissner state. In this case, the magnetic field around the strip can be computed in the same way as for

a strip in the Meissner state. In the opposite case ($I \sim I_{c2}$), the current density all over the strip equals the second critical value j_{c2} which makes the strip behave as a normal one with a spatially uniform current density. Hence the magnetic field around the strip can be computed as for a normal strip wire.

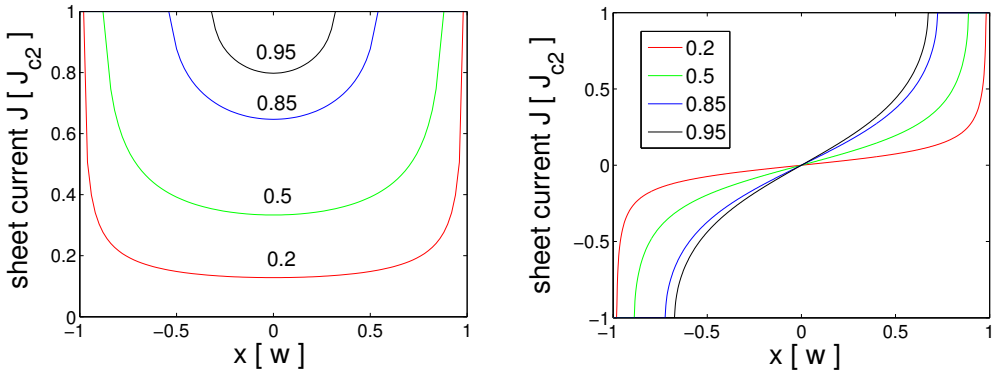

Figure 4.27: Sheet current density distribution in a strip in the mixed state vs ratio I/I_{c2} (left) and ratio B_b/B_{c2} (right). The current has been increased from zero (vergin state). The four curves correspond to the ratio I/I_{c2}, $B_b/B_{c2} = 0.2, 0.5, 0.85, 0.95$ respectively.

4.8.2 Current distribution

Let us first consider a superconducting strip carrying a transport current I in a zero external field. The Bean critical state model (Bean, 1962) is applied here: the current density (in units of $\mathrm{A/m^2}$) takes the critical values $\pm j_{c2}$ in the region where the magnetic flux penetrates and is zero in the free-field region. Brandt & Indenbom (1993); Zeldov *et al.* (1994); Brandt (1996) define the sheet current density (in units of A/m) by integrating j_{c2} over the thickness of the strip, $J(x) = (t_+ + t_-)j_{c2}$, where t_+ and t_- are the thicknesses of the regions carrying $+j_{c2}$ or $-j_{c2}$ respectively. Note that $t_\pm$ also depend on the history of ramping the supercurrent up and down. Since $t_+ + t_- \le t$, the sheet current should be less than its critical value $J_{c2} = tj_{c2}$, which is approached near the strip edges. The current in the central part of the strip is much smaller because the current-carrying domain shields it from the external field, similarly to the Meissner state. The sheet current distribution in a strip in the mixed state is given by (Brandt & Indenbom, 1993) (see Fig. 4.27left)

$$J(x,I) = \begin{cases} \frac{2J_{c2}}{\pi} \arctan \sqrt{\frac{w^2-b^2}{b^2-x^2}}\ , & |x| \le b \\ J_{c2}\ , & b \le |x| \le w \end{cases} \tag{4.55}$$

where $b = w\sqrt{1 - I^2/I_{c2}^2}$, I is the transport current and $I_{c2} = 2wJ_{c2}$ the maximal transport current. It is achieved when the magnetic field fully penetrates the strip, in that case $b = 0$ and the current density everywhere in the strip is J_{c2}. If the transport current exceeds I_{c2}, then the

superconducting strip transits into a normal one. For a niobium strip with a width $2w = 20\mu\mathrm{m}$ and a thickness $t = 60\mathrm{nm}$, placed in a zero external field, the transport current should be smaller than $2wJ_{c2} = 6.19 \times 10^{-2}\mathrm{A}$ to keep it in the mixed state.

Let us now consider the case of an external magnetic field, with the transport current being zero. If the field is parallel to the top surface of the strip, it has no impact on the strip, as long as the strip is infinitely thin. If the field is perpendicular to the top surface of the strip, the distribution of the induced sheet current density is given by (Brandt & Indenbom, 1993; Zeldov *et al.*, 1994)

$$J(x, B_b) = \begin{cases} \frac{2J_{c2}}{\pi} \arctan \frac{x}{w} \sqrt{\frac{w^2-b^2}{b^2-x^2}} \ , & |x| \le b \\ J_{c2} \frac{x}{|x|} \ , & b \le |x| \le w \end{cases} \tag{4.56}$$

where $b = w/\cosh(B_b/B_{c2})$, $B_{c2} = \mu_0 J_{c2}/\pi$ is a characteristic field value. te. If the external field B_b significantly exceeds B_{c2}, b decreases to 0, and the current density takes a step-like profile (see Fig. 4.27, right). Taking the same parameters as above (Niobium strip, width $2w = 20\mu\mathrm{m}$, thickness $t = 60\mathrm{nm}$) we find a characteristic field $B_{c2} = 12\,\mathrm{G}$.

We recall that our Eqs.(4.55, 4.56) can be applied only when the transport current I and the external field B_b have been increased from zero for the first time. The effect of reversing the current or the bias field, resulting in more complex current distributions that are 'frozon' in the wire, is discussed in detail by Brandt & Indenbom (1993).

4.8.3 Discussion

Compared to a superconducting strip in the Meissner state, a mixed state strip has some advantages and disadvantages. A superconducting strip in the mixed state can carry a higher transport current due to the higher critical sheet current density J_{c2} and consequently provide a tighter trapping confinement. On the other hand, the mixed state superconductor traps magnetic flux which may result in higher magnetic noise and corrugation of the trapping potential at low height. This is due to the motion of trapped votices that produce larger magnetic noise than the thermal motion of residual normally conducting electrons in the Meissner state (Scheel *et al.*, 2007). In addition, if the transport current or the external field is increased from zero to a certain value and then decreased to zero again, there is still some magnetic fields kept inside the mixed state superconductor. This should be taken into account for loading and controlling of the atoms as well as the magnetic noise. The magnetic 'pre-history' is also relevant, as vortices may be trapped when the superconductor is cooled through the transition temperature in an external field. Still, we have good reasons to believe that cold atoms can be maintained long enough and close enough to a mixed state atom chip so that they can be applied as a sensitive new probe for the mixed state superconductor. The magnetic noise from the vortex motion in the mixed state could be detected by the spin dephasing rate of trapped atoms (Scheel *et al.*, 2007). The high sensitivity of cold atoms to the magnetic trapping field (Wildermuth *et al.*, 2005; Vengalattore *et al.*, 2007) can be used to image the static disorder produced by frozen vortices (Scheel *et al.*, 2007). Atom clouds have a highe spatial resolution ($3\mu\mathrm{m}$), better than conventional SQUIDs, and their high sensitivity provides a promising alternative to traditional methods based on the noise of the transport current (Scola *et al.*, 2006).

4.9 Conclusion

A magnetic trap can be formed above a superconducting wire carrying a current and placed in a bias field. Compared to a normal metallic chip, a superconducting one significantly reduces the magnetic noise, especially when it is in the Meissner state. The magnetic noise is less by 6 orders than that around a normal one (Skagerstam *et al.*, 2006). Technical noises can be removed by using persistent currents. Besides, a superconducting wire can transport high currents without the Joule heating. And there is zero voltage drop across a superconducting wire. For a normal chip, the Joule heating and the high electric field across the wires lead to deformation and shift of the atom trap and increases the magnetic noise. For a normal conductor with a cross-section of a size of $\mu\mathrm{m}^2$ and a resistivity of the order of $\mu\Omega\,\mathrm{cm}$, the electric field across the wire has a magnitude of $10^4\mathrm{V/m}$, where a Rb atom may experience an attractive potential of an order of $10^2\mathrm{Hz}$ ($u = -1/2\alpha E^2$). The superconducting chip also has some disadvantagdes. Its trap confinement is not as good as a normal one's, but it still might improve the lifetime of trapped atoms due to the significant reduction of magnetic noise.

The magnetic field and supercurrents around a superconducting wire in the Meissner state have been computed both numerically in a self-consistent way and analytically by conformal mapping. Bean-Brandt model has been used for the superconducting wires in the mixed state. The supercurrents become large at sharp corners and near edges. With identical dimensions, transport currents and bias fields, at low trap height $d \leq 2.5w$ (reactangle and strip) or $d \leq 2.5R$ (cylinder), the superconducting wire brings the trap center closer to the top surface than a normal conducting one, especially when it is in the Meissner state. This result is in qualitative agreement with the recent publication by Cano *et al.* (2008). It is the supercurrents that make the trap-surface distance shorter. The finite thickness of a superconducting rectangle makes the trap even closer to the surface, because of the screening currents on the side faces of the wire, which are not taken into account for a superconducting strip. The magnetic trap above a superconducting rectangle or strip in this region has some similarity with the double-wire trap. The two maxima of the current distribution at the edges play a role of co-propagating currents in the double-wire trap. On the other hand, in the opposite region the effect of the screening currents is negligible. The trap based on a superconducting wire is like a 'side guide' trap based on a normal metallic wire. The supercurrents strongly shield the superconductor from the exteranl magnetic field perpendicular to its surface. This effect has to be taken into account for the loading and controlling cold atoms. The superconducting chip in the mixed state produces higher magnetic noise than the one in the Meissner state, due to the motion of votices. But it is still attractive for some advantages. The superconducting wire in the mixed state can transport higher current due to the high critical values, hance it can provide tighter confinment. Cold atoms trapped above the superconducting chip in the mixed state can be applied as a new probe for the study of vortex dynamics. The critical current and external field strongly depend on geometry and material.

We have studied the magnetic traps produced by superconductors with assumption that the screening currents only flow on the surface (sheet current approximation). The surface currents screen the superconductor from the external field. There is no field inside the supconductor. If we take into account the finite penetration depth, the field and current will be on a scale λ_L

below the surface (Brandt & Mikitik, 2000a). The London equations are required inside the superconductor for more accurate descriptions. This is one of our next work.

We have studied the magnetic trap formed by a superconducting strip in the mixed state without considering the effect of the side faces. However, the side faces do has impact on the magnetic field and supercurrent distribution (Brandt, 1996). In addition, for a superconducting wire with arbitrary cross-sections in the mixed state, Ginzburg-Landau equations may be required Brandt & Indenbom (1993); Zharkov *et al.* (2000). This could be our future work.

The superconducting wires we studied in this chapter are all of infinite length. In a real atom chip design, 'U' or 'Z' form guiding wires are widely used. In that case, the trapping field should be studied in three-dimensional setting. Our results can be applied on the central part of 'U' or 'Z' wires, as long as it is sufficiently far away from the ends. The effect of the ends will be investigated in the future.

Multiple current-carrying wires have been miniturized and integrated on atom chips to provide atom traps, guides and so on. Our next work might also focus on how a current imposed in one superconducting wire creates currents in the neighboring ones, which might change the features of the magnetic trap (Cano *et al.*, 2008).

Conclusion

In this thesis, we have studied magnetic microtraps above complex microchip structures, as well as the thermal magnetic noise surrounding these metallic component. Magnetic traps formed by superconducting wires have been investigated in the last part, since they can significantly reduce thermal noise and technical noise.

The lifetime of atoms above a layered chip has been investigated semi-analytically. Numerical calculations have been performed for the loss rate due to spin flips induced by thermal noise by means of multi-layer reflection coefficients. The magnetic noise depends essentially on the thickness of the topmost metallic layer, as long as the the layers below have a much smaller conductivity. The same magnetic noise could be obtained with a metallic membrane suspended in vacuum. Based on this result, scaling laws for loss rate above a thin metallic layer have been developed. The skin depth δ is highlighted as a characteristic length scale. At distances smaller than δ, the thermal magnetic noise power roughly scales with the volume of the metallic material, hence the thickness of the metallic layer. A thin layer helps to increase the trap lifetime if its thickness is substantially thinner than the skin depth at the Larmor frequency, inversely it even gives a shorter lifetime than a bulk metal when its thickness is comparable to the skin depth. Lifetimes evaluated without adjustable parameters are in a good agreement with the experiment at a distance of a few microns. At shorter distances, atom-surface potentials of the van der Waals-Casimir-Polder type might lower the trap barrier and open additional loss channels. This could be our next work for a more precise description of trapping lifetime.

The impact of finite lateral size (width) of conducting wires on magnetic noise has been considered in two-dimensional setting. The thermal magnetic noise around a metallic wire of arbitrary cross-section has been computed with the help of boundary integral equations. At distances smaller than the skin depth δ, the main property of the infinitely wide wire applies still for a wire of finite width: the spectral noise power roughly scales with the volume of metallic material, in consistency with the 'incoferent summation approximation'. As the wire width increases, the magnetic noise saturates. The main difference beween an infinitely wide wire and a finitely wide wire is that the magnetic noise components $\mathcal{B}_{xx}$ and $\mathcal{B}_{yy}$ (parallel and perpendicular to the wire surface, respectively) are identical above the infinitely wide wire, whereas the magnetic noise around the finitely wide wire is strongly dependent on the polarization. Strategies to minimize loss or decoherence due to thermal magnetic fields is suitably choosing the direction of the static trapping fields. Inceasing the width of the wire, the magnetic noise component $\mathcal{B}_{xx}$ levels off faster than $\mathcal{B}_{yy}$. $\mathcal{B}_{yy}$ gets maximum when the trap height is comparable to the wire width. The incoherent summation approximation systematically over-

estimates the noise power in one of the two field polarizations, but otherwise reproduces the main features as long as the skin depth is the largest scale. The noise power can be significantly non-additive when dealing with multiple objects. Our method is restricted to 2D and does not permit quantitative predictions of trap lifetimes. Expanding our method into three dimensions and calculating trap lifetime above wires with finite size may be our next work.

A magnetic trap generated by a superconducting wire has been investigated. The trapping field and supercurrents around a superconducting wire in the Meissner state and the mixed state with arbitrary cross sections have been computed both analytically by means of a conformal mapping and numerically in a self-consistent way. At low trap height, compared to a normal chip, a superconducting wire with identical dimensions brings the trap center closer to the chip surface. This results from the distribution of the supercurrent that shield the interior of the superconductor from the magnetic field. Taking into account the supercurrents on the side faces, the finite thickness of a superconducting rectangular wire makes the trap even closer to the surface than a superconducting infinitely thin wire (strip). The magnetic trap above a superconducting rectangle or strip has some similarity with a double-wire trap: the two maxima of the current distribution at the edges work like co-propagating currents and produce potential barriers near the corners. This makes the loading and controlling atoms above a superconducting chip different from those of a normal one. The confinement potential provided by a superconducting chip is not as strong as a normal one, but they are still enough for trapping atoms. However, superconducting chips improve the lifetime of trapped atoms due to the significant reduction of thermal magnetic noise, especially when they are in the Meissner state. In addition, technical noise can be completely removed by using persistent currents. Superconducting chips in the mixed (Shubnikov) state are likely to produce higher magnetic noise than those in the Meissner state, due to the motion of vortices. Tighter confinements can be obtained in superconducting chips in the mixed state due to the higher critical current. Cold atoms trapped above superconducting chips in the mixed state can also be applied as a new probe for the study of vortex dynamics. Critical currents and external fields for a superconducting rectangle and strip are much smaller than the values for a flat bulk and a cylinder. One should be careful not to exceed the critical values, especially because the supercurrent becomes large near a sharp corner.

Our numerical and analytical calculations are both made under the sheet current approximation where the penetration depth λ_L is much smaller than the thickness and width of the wire and the screening currents only flow on the surface. A more accurate description needs to take into account the finite penetration depth λ_L using the London equations, for example. This is one of our future works. In the future, we will also investigate magnetic traps produced by superconducting wires in the mixed state with arbitrary cross-section.

In a real atom chip design, ‘U’ or ‘Z’ form guiding wires are widely used. In that case, the trapping field should be computed in three dimensions. Our results can be applied on the central part of ‘U’ or ‘Z’ wires, as long as it is sufficiently far away from the ends. The effects of the ends could be our next work.

Bibliography

Abramowitz, M., & Stegun, I. A. (eds). 1972. *Handbook of Mathematical Functions*. 9nd edn. New York: Dover Publications, Inc.

Agarwal, G. S. 1975. Quantum electrodynamics in the presence of dielectrics and conductors. I. Electromagnetic-field response functions and black-body fluctuations in finite geometries. *Phys. Rev. A*, **11**, 230.

Andersson, E., Calarco, T., Folman, R., Andersson, M, Hessmo, B., & Schmiedmayer, J. 2002. Multimode interferometer for guided matter waves. *Phys. Rev. Lett.*, **88**, 100401.

Bancroft, Randy. 1996. *Understanding electromagnetic scattering using the moment method: a practical approach*. Norwood, MA: Artech House.

Barrett, M. D., Sauer, J. A., & Chapman, M. S. 2001. All-optical formation of an atomic Bose-Einstein condensate. *Phys. Rev. Lett.*, **87**, 010404.

Bauer, Siegfried. 1992. Optical properties of a metal film and its application as an infrared absorber and as a beam splitter. *Am. J. Phys.*, **60**, 257.

Bean, C. P. 1962. Magnetization of hard superconductors. *Phys. Rev. Lett.*, **8**, 250.

Biehs, S.-A., Reddig, D., & Holthaus, M. 2007. Thermal radiation and near-field energy density of thin metallic films. *Eur. Phys. J. B*, **55**, 237.

Blatter, G., Feigel'man, M. V., Geshkenbein, V. B., Larkin, A. I., & Vinokur, V. M. 1994. Vortices in high-temperature superconductors. *Rev. Mod. Phys.*, **66**, 1125.

Brandt, E. H. 1996. Superconductors of finite thickness in a perpendicular magnetic field: strips and slabs. *Phys. Rev. B*, **54**, 4246.

Brandt, E. H., & Indenbom, M. 1993. Type-II-superconductor strip with current in a perpendicular magnetic field. *Phys. Rev. B*, **48**, 12893.

Brandt, E. H., & Mikitik, G. P. 2000. Critical state in superconductor thin plates with elliptic shape. *Physica. B*, **284**, 745.

Brandt, E. H., & Mikitik, G. P. 2000a. Meissner-London currents in superconductors with rectangular cross section. *Phys. Rev. Lett.*, **85**, 4164.

Cano, D., Kasch, B., Hattermann, H., Koelle, D., Kleiner, R., Zimmermann, C., & Fortagh, J. 2008. Impact of the Meissner effect on magnetic microtraps for neutral atoms near superconducting thin films. *Phys. Rev. A*, **77**, 063408.

Cassettari, D., Hessmo, B., Folman, R., Maier, T., & Schmiedmayer, J. 2000a. Beam splitter for guided atoms. *Phys. Rev. Lett.*, **85**, 5483.

Cassettari, D., Chenet, A., Folman, R., Haase, A., Hessmo, B., Krüger, P., Maier, T., Schneider, S., Calarco, T., & Schmiedmayer, J. 2000b. Micromanipulation of neutral atoms with nanofabricated structures. *Appl. Phys. B*, **70**, 721.

Cornell, E. A., & Wieman, C. E. 2002. Nobel Lecture: Bose-Einstein condensation in a dilute gas, the first 70 years and some recent experiments. *Rev. Mod. Phys.*, **74**, 875.

Dekker, N. H., Lee, C. S., Lorent, V., Thywissen, J. H., Smith, S. P., Drndić, M., Westervelt, R. M., & Prentiss, M. 2000. Guiding neutral atoms on a chip. *Phys. Rev. Lett.*, **84**, 1124.

Denschlag, J., Cassettari, D., & Schmiedmayer, J. 1999. Guiding Neutral Atoms with a Wire. *Phys. Rev. Lett*, **82**, 2014.

Dikovsky, V., Japha, Y., Henkel, C., & Folman, R. 2005. Reduction of magnetic noise in atom chips by material optimization. *Eur. Phys. J. D*, **35**, 87.

Dikovsky, V., Sokolovsky, V., Zhang, B., Henkel, C., & Folman, R. 2008. Superconducting atom chips: advantages and challenges. *submitted to Eur. Phys. J. D*.

Finnemore, D. K., Stromberg, T. F., & Swenson, C. A. 1966. Superconducting properties of high-purity niobium. *Phys. Rev.*, **149**, 231.

Folman, R., Krüger, P., Cassettari, D., Hessmo, B., Maier, T., & Schmiedmayer, J. 2000. Controlling Cold Atoms using Nanofabricated Surfaces: Atom Chips. *Phys. Rev. Lett*, **84**, 4749.

Folman, R., Krüger, P., Schmiedmayer, J., Denschlag, J., & Henkel, C. 2002. Microscopic atom optics: from wires to an atom chip. *Adv. At. Mol. Opt. Phys.*, **48**, 263.

Fortágh, J., & Zimmermann, C. 2007. Magnetic microtraps for ultracold atoms. *Rev. Mod. Phys.*, **79**, 235.

Fortágh, J., Ott, H., Kraft, S., Günther, A., & Zimmermann, C. 2002. Surface effects in magnetic microtraps. *Phys. Rev. A*, **66**, 041604.

Frisch, R., & Segrè, E. 1933. Über die Einstellung der Richtungsquantelung. II. *Z. Phys.*, **80**, 610.

Gehm, M. E., O'Hara, K. M., Savard, T. A., & Thomas, J. E. 1998. Dynamics of noise-induced heating in atom traps. *Phys. Rev. A*, **58**, 3914.

Grimm, R. Weidemuller, M., & Ovchinnikov, Y. 2000. Optical dipole traps for neutral atoms. *Adv. At. Mol. Opt. Phys*, **42**, 95.

Groth, S., Krüger, P., Wildermuth, S., Folman, R., Fernholz, T., Schmiedmayer, J., Mahalu, D., & Bar-Joseph, I. 2004. Atom chips: Fabrication and thermal properties. *Appl. Phys. Lett.*, **85**, 2980.

Haase, A., Cassettari, D., Hessmo, B., & Schmiedmayer, J. 2001. Trapping neutral atoms with a wire. *Phys. Rev. A*, **64**, 043405.

Hänsel, W., Hommelhoff, P., Hänsch, T. W., & Reichel, J. 2001. Bose-Einstein condensation on a microelectronic chip. *Nature*, **413**, 498.

Hänsel, W., Reichel, J., Hommelhoff, P., & Hänsch, T. W. 2001. Magnetic conveyor belt for transporting and merging trapped atom clouds. *Phys. Rev. Lett.*, **86**, 608.

Hänsel, W., Reichel, J., Hommelhoff, P., & Hänsch, T. W. 2001c. Trapped-atom interferometer in a magnetic microtrap. *Phys. Rev. A*, **64**, 063607.

Harber, D. M., McGuirk, J. M., Obrecht, J. M., & Cornell, E. A. 2003. Thermally induced losses in ultra-cold atoms magnetically trapped near room-temperature surfaces. *J. Low Temp. Phys.*, **133**, 229.

Harber, D. M., Obrecht, J. M., McGuirk, J. M., & Cornell, E. A. 2005. Measurement of the Casimir-Polder force through center-of-mass oscillations of a Bose-Einstein condensate. *Phys. Rev. A*, **72**, 033610.

Harrington, R. F. 1993. *Field computation by moment methods*. 1st edn. Piscataway: Wiley-IEEE Press.

Henkel, C. 2005. Magnetostatic field noise near metallic surfaces. *Eur. Phys. J. D*, **35**, 59.

Henkel, C., & Pötting, S. 2001. Coherent transport of matter waves. *Appl. Phys. B*, **72**, 73.

Henkel, C., Pötting, S., & Wilkens, M. 1999. Loss and heating of particles in small and noisy traps. *Appl. Phys. B*, **69**, 379.

Henkel, C., Krüger, P., Folman, R., & Schmiedmayer, J. 2003. Fundamental limits for coherent manipulation on atom chips. *Appl. Phys. B*, **76**, 173.

Henkel, C., Power, B., & Sols, F. 2005. New light on cavity QED with ultracold atoms. *Page 34 of:* Weiner, J., Feenstra, L, & Schmiedmayer, J (eds), *Proceedings of the Conference on Atoms and Molecules near Surfaces (CAMS)*. Heidelberg: J. Phys.: Conf. Series.

Hess, H. F., Kochanski, G. P., Doyle, J. M., Masuhara, N., Kleppner, D., & Greytak, T. J. 1987. Magnetic trapping of spin-polarized atomic hydrogen. *Phys. Rev. Lett.*, **59**, 672.

Hinds, E. A., & Hughes, I. G. 1999. Review Article: Magnetic atom optics: mirrors, guides, traps, and chips for atoms. *J. Phys. D*, **32**, 119.

Hinds, E. A., Vale, C. J., & Boshier, M. G. 2001. Two-wire waveguide and interferometer for cold atoms. *Phys. Rev. Lett.*, **86**, 1462.

Hohenester, U., Eiguren, A., Scheel, S., & Hinds, E. A. 2007. Spin-flip lifetimes in superconducting atom chips: Bardeen-Cooper-Schrieffer versus Eliashberg theory. *Phys. Rev. A*, **76**, 033618.

Jackson, J. D. 1975. *Classical Electrodynamics*. 2nd ed. edn. New York: Wiley & Sons.

Jones, M. P. A., Vale, C. J., Sahagun, D., Hall, B. V., & Hinds, E. A. 2003. Spin coupling between cold atoms and the thermal fluctuations of a metal surface. *Phys. Rev. Lett.*, **91**, 080401.

Ketterle, W. 2002. Nobel Lecture: When atoms behave as waves: Bose-Einstein condensation and the atom laser. *Rev. Mod. Phys.*, **74**, 1131.

Krüger, P. 2004. *Coherent matter waves near surfaces*. Ph.D. thesis, Universität Heidelberg.

Krugler, K. J., Paul, W., & Trinks, U. 1978. A magnetic storage ring for neutrons. *Phys. Lett. B*, **72**, 422.

Landau, L. D., Lifshitz, E. M., & Pitaevskii, L. P. 1984. *Electrodynamics of continuous media*. 2nd edn. Oxford: Pergamon.

Larbalestier, D., Gurevich, A., Feldmann, D. M., & Polyanskii, A. 2001. High-T_c superconducting materials for electric power applications. *Nature*, **414**, 368.

Leanhardt, A. E., Shin, Y., Chikkatur, A. P., Kielpinski, D., Ketterle, W., & Pritchard, D. E. 2003. Bose-Einstein condensates near a microfabricated surface. *Phys. Rev. Lett.*, **90**, 100404.

Lin, Y., Teper, I., Chin, C., & Vuletic, V. 2004. Impact of the Casimir-Polder potential and Johnson noise on Bose-Einstein condensate stability near surfaces. *Phys. Rev. Lett.*, **92**, 050404.

London, F., & London, H. 1935. The electromagnetic equations for the supraconductor. *Proc. Roy. Soc.*

Migdall, A. L., Prodan, J. V., Phillips, W. D., Bergeman, T. H., & Metcalf, H. J. 1985. First observation of magnetically trapped neutral atoms. *Phys. Rev. Lett.*, **54**, 2596.

Mukai, T., Hufnagel, C., Kasper, A., Meno, T., Tsukada, A., Semba, K., & Shimizu, F. 2007. Persistent Supercurrent Atom Chip. *Phys. Rev. Lett.*, **98**, 260407.

Müller, D., Anderson, D. Z., Grow, R. J., Schwindt, P. D. D., & Cornell, E. A. 1999. Guiding neutral atoms around curves with lithographically patterned current-carrying wires. *Phys. Rev. Lett.*, **83**, 5194.

Müller, D., Cornell, E. A., Prevedelli, M., Schwindt, P. D. D., Zozulya, A., & Anderson, D. Z. 2000. Waveguide atom beam splitter for laser-cooled neutral atoms. *Opt. Lett.*, **25**, 1382.

Negretti, A. 2005 (Dec). *Quantum engineering with ultracold neutral atoms*. Ph.D. thesis, University of Potsdam and University of Trento.

Nenonen, J., Montonen, J., & Katila, T. 1996. Thermal noise in biomagnetic measurements. *Rev. Sci. Instr.*, **67**, 2397.

Nieto-Vesperinas, M. 1991. *Scattering and Diffraction in Physical Optics*. New York: Wiley & Sons.

Nirrengarten, T., Qarry, A., Roux, C., Emmert, A., Nogues, G., Brune, M., Raimond, J.-M., & Haroche, S. 2006. Realization of a superconducting atom chip. *Phys. Rev. Lett.*, **97**, 200405.

Norris, W. T. 1970. Calculation of hysteresis losses in hard superconductors carrying ac: isolated conductors and edges of thin sheets. *J. Phys. D*, **3**, 489.

Paul, W. 1990. Electromagnetic traps for charged and neutral particles. *Rev. Mod. Phys.*, **62**, 531.

Pritchard, D. E. 1983. Cooling neutral atoms in a magnetic trap for precision spectroscopy. *Phys. Rev. Lett.*, **51**, 1336.

Purcell, E. M., Torrey, H. C., & Pound, R. V. 1946. Resonance absorption by nuclear magnetic moments in a solid. *Phys. Rev.*, **69**, 37.

Reichel, J. 2002. Microchip traps and Bose-Einstein condensation. *Appl. Phys. B*, **75**, 469.

Reichel, J., Hänsel, W., & Hänsch, T. W. 1999. Atomic micromanipulation with magnetic surface traps. *Phys. Rev. Lett.*, **83**, 3398.

Rekdal, P. K., & Skagerstam, B. K. 2007. Decay processes in the presence of thin superconducting films. *Phys. Rev. A*, **75**, 022904.

Rekdal, P. K., Scheel, S., Knight, P. L., & Hinds, E. A. 2004. Thermal spin flips in atom chips. *Phys. Rev. A*, **70**, 013811.

Rockstuhl, C., Salt, M. G., & Herzig, H. P. 2003. Application of the boundary-element method to the interaction of light with single and coupled metallic nanoparticles. *J. Opt. Soc. Am. A*, **20**, 1969.

Rogobete, L., & Henkel, C. 2004. Spontaneous emission in a subwavelength environment characterized by boundary integral equations. *Phys. Rev. A*, **70**, 063815.

Roux, C., Emmert, A., Lupascu, A., Nirrengarten, T., Nogues, G., Brune, M., Raimond, J.-M., & Haroche, S. 2008. Bose-Einstein condensation on a superconducting atom chip. *Europhys. Lett.*, **81**, 56004.

Sakurai, J. J. 1994. *Modern Quantum mechnics*. revised edn. Addison-Wesley.

Scheel, S., Rekdal, P. K., Knight, P. L., & Hinds, E. A. 2005. Atomic spin decoherence near conducting and superconducting films. *Phys. Rev. A*, **72**, 042901.

Scheel, S., Fermani, R., & Hinds, E. A. 2007. Feasibility of studying vortex noise in two-dimensional superconductors with cold atoms. *Phys. Rev. A*, **75**, 064901.

Schmiedmayer, J. 1992. IQEC 92:XVIIIth International conference on Quantum Electronics. *In:* Magerl, G. (ed), *Technical Digest*.

Schmiedmayer, J. 1995. Guiding and trapping a neutral atom on a wire. *Phys. Rev. A*, **52**, R13.

Schmiedmayer, J., Folman, R., & Calarco, T. 2002. Quantum information processing with neutral atoms on an atom chip. *J. Mod. Opt*, **49**, 1375.

Scola, J., Pautrat, A., Goupil, C., & Simon, Ch. 2006. Experimental study of the correlation length of critical-current fluctuations in the presence of surface disorder: Probing vortex long-range interactions. *Phys. Rev. B*, **73**, 024508.

Shin, Y., Sanner, C., Jo, G.-B., Pasquini, T. A., Saba, M., Ketterle, W., Pritchard, D. E., Vengalattore, M., & Prentiss, M. 2005. Interference of Bose-Einstein condensates split with an atom chip. *Phys. Rev. A*, **72**, 021604.

Sidles, J. A., Garbini, J. L. Dougherty, W. M., & Chao, S. H. 2003. The classical and quantum theory of thermal magnetic noise, with applications in spintronics and quantum microscopy. *PROCEEDINGS OF THE IEEE*, **91**, 799.

Skagerstam, B. K., & Rekdal, P. K. 2007. Photon emission near superconducting bodies. *Phys. Rev. A*, **76**, 052901.

Skagerstam, B. K., Hohenester, U., Eiguren, A., & Rekdal, P. K. 2006. Spin decoherence in superconducting atom chips. *Phys. Rev. Lett.*, **97**, 070401.

Sukumar, C. V., & Brink, D. M. 1997. Spin-flip transitions in a magnetic trap. *Phys. Rev. A*, **56**, 2451.

Thywissen, J. H., Olshanii, M., Zabow, G., Drndić, M., Johnson, K. S., Westervelt, R. M., & Prentiss, M. 1999. Microfabricated magnetic waveguides for neutral atoms. *Eur. Phys. J. D*, **7**, 361.

Treutlein, P., Hommelhoff, P., Steinmetz, T., Hänsch, T. W., & Reichel, J. 2004. Coherence in Microchip Traps. *Phys. Rev. Lett.*, **92**, 203005.

Tuncer, E., & Neikirk, D. P. 1993. Efficient calculation of surface impedance for rectangular conductors. *Elec. Lett.*, **29**, 2127.

Turchette, Q. A., Myatt, C. J., King, B. E., Sackett, C. A., Kielpinski, D., Itano, W. M., Monroe, C., & Wineland, D. J. 2000. Decoherence and decay of motional quantum states of a trapped atom coupled to engineered reservoirs. *Phys. Rev. A*, **62**, 053807.

Varpula, T., & Poutanen, T. 1984. Magnetic field fluctuations arising from thermal motion of electric charge in conductors. *J. Appl. Phys.*, **55**, 4015.

Vengalattore, M., Higbie, J., Leslie, S., Guzman, J., Sadler, L., & Stamper-Kurn, D. 2007. High-resolution magnetometry with a spinor Bose-Einstein condensate. *Phys. Rev. Lett.*, **98**, 200801.

Vladimirskii, V. V. 1961. Magnetic mirrors, channels and bottles for cold neutrons. *Soviet Phys. JETP-USSR*, **12**, 740.

Wildermuth, S., Krüger, P., Becker, C., Brajdic, M., Haupt, S., Kasper, A., Folman, R., & Schmiedmayer, J. 2004. Optimized magneto-optical trap for experiments with ultracold atoms near surfaces. *Phys. Rev. A*, **69**, 030901.

Wildermuth, S., Hofferberth, S., Lesanovsky, I., Haller, E., Andersson, L., Bar-Joseph, S. G., Krüger, P., & Schmiedmayer, J. 2005. Bose-Einstein condensates Microscopic magnetic-field imaging. *Nature*, **435**, 440.

Yeh, P. 1988. *Optical Waves in layered Media*. 1st edn. New York: Wiley & Sons.

Zeldov, E., Clem, John R., McElfresh, M., & Darwin, M. 1994. Magnetization and transport currents in thin superconducting films. *Phys. Rev. B*, **49**, 9802.

Zhang, B., & Henkel, C. 2007. Magnetic noise around metallic microstructures. *J. Appl. Phys.*, **102**, 084907.

Zhang, B., Henkel, C., Haller, E., Wildermuth, S., Hofferberth, S., Krüger, P., & Schmiedmayer, J. 2005. Relevance of sub-surface chip layers for the lifetime of magnetically trapped atoms. *Eur. Phys. J. D*, **35**, 97.

Zharkov, G. F., Zharkov, V., & A. Zvetkov, . 2000. Ginzburg-Landau calculations for a superconducting cylinder in a magnetic field. *Phys. Rev. B*, **61**, 12293.

Zhilichev, Y. N. 2001. Superconducting cylinder of finite length in transverse magnetic field. *Lat.J.Phys.Tech*, **5**, 14.

Zhilichev, Y. N. 2003. Magnetic field penetration into superconductors with sharp edges. *Physica. C*, **384**, 32.